

May 2023

# The Response of Atomic-to-Molecular Hydrogen Transition Points in Photodissociation Regions Due to a Hard X-Ray Spectrum

Gregory Joseph Colarch

Follow this and additional works at: <https://digitalscholarship.unlv.edu/thesesdissertations>



Part of the [Astrophysics and Astronomy Commons](#)

---

## Repository Citation

Colarch, Gregory Joseph, "The Response of Atomic-to-Molecular Hydrogen Transition Points in Photodissociation Regions Due to a Hard X-Ray Spectrum" (2023). *UNLV Theses, Dissertations, Professional Papers, and Capstones*. 4660.

<http://dx.doi.org/10.34917/36114685>

This Dissertation is protected by copyright and/or related rights. It has been brought to you by Digital Scholarship@UNLV with permission from the rights-holder(s). You are free to use this Dissertation in any way that is permitted by the copyright and related rights legislation that applies to your use. For other uses you need to obtain permission from the rights-holder(s) directly, unless additional rights are indicated by a Creative Commons license in the record and/or on the work itself.

This Dissertation has been accepted for inclusion in UNLV Theses, Dissertations, Professional Papers, and Capstones by an authorized administrator of Digital Scholarship@UNLV. For more information, please contact [digitalscholarship@unlv.edu](mailto:digitalscholarship@unlv.edu).

THE RESPONSE OF ATOMIC-TO-MOLECULAR HYDROGEN TRANSITION POINTS IN  
PHOTODISSOCIATION REGIONS DUE TO A HARD X-RAY SPECTRUM

By

Gregory Joseph Colarch

Bachelor of Science – Astrophysics  
University of Calgary  
2009

Master of Science – Physics  
University of Nevada, Las Vegas  
2012

Master of Science – Health Physics  
University of Nevada, Las Vegas  
2015

A dissertation submitted in partial fulfillment  
of the requirements for the

Doctor of Philosophy – Physics

Department of Physics and Astronomy  
College of Sciences  
The Graduate College

University of Nevada, Las Vegas  
May 2023



## **Dissertation Approval**

The Graduate College  
The University of Nevada, Las Vegas

April 5, 2023

This dissertation prepared by

Gregory Joseph Colarch

entitled

The Response of Atomic-to-Molecular Hydrogen Transition Points in Photodissociation  
Regions Due to a Hard X-Ray Spectrum

is approved in partial fulfillment of the requirements for the degree of

Doctor of Philosophy – Physics  
Department of Physics and Astronomy

Stephen Lepp, Ph.D.  
*Examination Committee Chair*

Tao Pang, Ph.D.  
*Examination Committee Member*

Bernard Zygelman, Ph.D.  
*Examination Committee Member*

Steen Madsen, Ph.D.  
*Graduate College Faculty Representative*

Alyssa Crittenden, Ph.D.  
*Vice Provost for Graduate Education &  
Dean of the Graduate College*

# Abstract

This dissertation develops a model for the response of the transition points in the density profiles from atomic ( $H^0$ ) to molecular ( $H_2$ ) hydrogen in a photodissociation region (PDR) due to a hard X-ray flux (HXR). A model for a steady-state PDR due to the photodissociation of  $H_2$  by the far-ultraviolet (FUV) Lyman-Werner radiation band is presented both analytically and computationally. A steady state X-ray dissociation region (XDR) from an HXR in the 1 - 100 keV energy range is also developed both analytically and computationally. An analytic model is then developed by combining these two different steady state models. The inclusion of the hard X-rays gives rise to additional ionization in the PDR from secondary electrons which also leads to the generation of an internal FUV radiation field. Computational results for the density profiles and the response of the transition point of the PDR due to the HXR flux are given. A simple analytic formula based upon the separate PDR and XDR is then given which can provide an approximation to the transition point due to their combination.

# Acknowledgements

I would like to thank my advisor Dr. Stephen Lepp for agreeing to take me on as a graduate student as well as for his insight and expertise throughout this degree. I would also like to thank the members of my advisory committee for providing me with helpful comments and suggestions: Dr. Bernard Zygelman, Dr. Tao Pang, and Dr. Steen Madsen. I respectfully acknowledge the financial support given for my graduate studies from the State of Nevada.

Finally I would like to thank my fiancée Kasia Staszkiwicz who earned her own PhD in Patience along the way.

# Dedication

To my mother Vivian and my father Joseph.

# Table of Contents

<b>Abstract</b>	<b>iii</b>
<b>Acknowledgements</b>	<b>iv</b>
<b>Dedication</b>	<b>v</b>
<b>List of Tables</b>	<b>ix</b>
<b>List of Figures</b>	<b>xii</b>
<b>1 Introduction</b>	<b>1</b>
<b>2 PDR - Model</b>	<b>5</b>
2.1 Physical Processes . . . . .	5
2.1.1 Ultraviolet Radiation Field . . . . .	6
2.1.2 Molecular Hydrogen Destruction . . . . .	9
2.1.2.1 Solomon Process . . . . .	12
2.1.3 Attenuation of Ultraviolet Radiation . . . . .	15
2.1.3.1 Extinction due to Interstellar Dust . . . . .	16
2.1.3.2 Line Profiles . . . . .	21
2.1.3.3 Self-Shielding of Molecular Hydrogen . . . . .	27
2.1.4 Molecular Hydrogen Formation . . . . .	29
2.1.4.1 Formation in the Gas Phase . . . . .	29
2.1.4.2 Formation on Dust Grains . . . . .	30
2.2 Steady State FUV Field Creation - Destruction of Molecular Hydrogen . . . . .	34

<b>3</b>	<b>XDR - Model</b>	<b>38</b>
3.1	Physical Processes . . . . .	38
3.1.1	Hard X-Ray Radiation Field . . . . .	39
3.1.2	Molecular Hydrogen Destruction . . . . .	44
3.2	Steady State HXR Field Creation - Destruction of Molecular Hydrogen . . . . .	46
3.2.1	Internally Generated UV Field due to Secondary Electrons . . . . .	49
3.3	Steady State XUV Field Creation - Destruction of Molecular Hydrogen . . . . .	52
3.4	Steady State HXR Field Creation - Destruction of Molecular Hydrogen including an XUV Field . . . . .	58
<b>4</b>	<b>Density Profiles and Transition Points</b>	<b>62</b>
4.1	PDR Analytical Model . . . . .	62
4.2	PDR Computational Results . . . . .	63
4.2.1	PDR density profiles and transition points for Bialy & Sternberg 2016 . . . . .	64
4.2.2	PDR density profiles and transition points from computational model . . . . .	65
4.3	Analytic response of the PDR transition points to HXR field . . . . .	69
4.4	Computational response of the PDR transition points to HXR field . . . . .	70
4.4.1	$H_X \propto S(\tau_X)\tau_X^{-\phi-1}$ . . . . .	70
4.4.2	$H_X \propto \tau_X^{-\phi-1}$ . . . . .	73
4.5	Analytic Fit for $H_X \propto \tau_X^{-\phi-1}$ . . . . .	77
<b>5</b>	<b>Conclusions</b>	<b>80</b>
<b>Appendix A Far-Ultraviolet Spectral Distributions</b>		<b>83</b>
A.1	The Habing SED . . . . .	84
A.2	The Draine SED . . . . .	86
A.3	The Draine and Bertoldi SED . . . . .	88
A.4	The Draine - Sternberg SED . . . . .	90
<b>Appendix B Hard X-ray Attenuation and Energy Deposition</b>		<b>94</b>
<b>Appendix C Analytic Best Fit Curves</b>		<b>101</b>

References	117
Curriculum Vitae	123

# List of Tables

4.1	FUV transition points based on the five step analytical procedure for generating depth-dependent atomic and molecular densities (see Bialy & Sternberg 2016) . . . .	65
4.2	FUV transition points . . . . .	67
4.3	Comparison of H <sup>0</sup> and H <sub>2</sub> transition points for FUV irradiated PDR with analytic vs. computational models . . . . .	69
4.4	HXR energy flux $F_X/n_H$ [erg cm s <sup>-1</sup> ] at the H <sup>0</sup> -to-H <sub>2</sub> combined FUV-HXR transition points at one order of magnitude increase in $N_H$ column density for $S(\tau_X)\tau^{-\phi-1}$ attenuation. . . . .	72
4.5	HXR energy flux $F_X/n_H$ [erg cm s <sup>-1</sup> ] at the H <sup>0</sup> -to-H <sub>2</sub> combined FUV-HXR transition points at one order of magnitude increase in $N_H$ column density for $\tau^{-\phi-1}$ attenuation. 73	
4.6	Ratio of the HXR energy flux $F_X/n_H$ [erg cm s <sup>-1</sup> ] at one order of magnitude increase in $N_H$ column density for $\tau^{-\phi-1}$ vs. $S(\tau_X)\tau^{-\phi-1}$ . . . . .	77
A.1	Habing SED . . . . .	86
A.2	Draine SED . . . . .	88
A.3	Draine & Bertoldi SED . . . . .	90
A.4	Draine - Sternberg SED . . . . .	92

# List of Figures

2.1	Self-shielding function . . . . .	28
4.1	H <sup>0</sup> and H <sub>2</sub> density profiles for FUV irradiated PDR based on the five step analytical procedure for generating depth-dependent atomic and molecular densities (see Bialy & Sternberg 2016) . . . . .	64
4.2	H <sup>0</sup> and H <sub>2</sub> density profiles for FUV irradiated PDR . . . . .	66
4.3	Comparison of H <sup>0</sup> and H <sub>2</sub> density profiles for FUV irradiated PDR by analytic vs. computational models . . . . .	68
4.4	The transition point curve where $x_{\text{H}^0} = 2x_{\text{H}_2}$ for the response of a PDR to an HXR field with $S(\tau_X)\tau^{-\phi-1}$ attenuation. The vertical portion of the curve represents the FUV only transition point. The contribution of $\beta B$ as a percentage of $\delta$ to the column density of the transition point is shown at 10% (orange dot), 50% (green dot), and 90% (red dot). . . . .	71
4.5	The H <sup>0</sup> and H <sub>2</sub> density profiles and transition points for $x_{\text{H}^0}$ and $2x_{\text{H}_2}$ of an FUV only flux superimposed with an HXR flux $S(\tau_X)\tau^{-\phi-1}$ attenuation that causes a response in the PDR transition point by one order of magnitude. . . . .	72
4.6	The transition point curve where $x_{\text{H}^0} = 2x_{\text{H}_2}$ for the response of a PDR to an HXR field with $\tau^{-\phi-1}$ attenuation. The vertical portion of the curve represents the FUV only transition point. The contribution of $\beta B$ as a percentage of $\delta$ to the column density of the transition point is shown at 10% (orange dot), 50% (green dot), and 90% (red dot). . . . .	74

4.7	The $H^0$ and $H_2$ density profiles and transition points for $x_{H^0}$ and $2x_{H_2}$ of an FUV only flux superimposed with an HXR flux $\tau^{-\phi-1}$ attenuation that causes a response in the PDR transition point by one order of magnitude. . . . .	75
4.8	Comparison of the response for the attenuation functions $S(\tau_X)\tau^{-\phi-1}$ and $\tau^{-\phi-1}$ . . .	76
4.9	The transition point curves for the response of a PDR to an HXR field with $\tau^{-\phi-1}$ (solid blue line) superimposed with the analytic model (orange dashed line). A variation of $\pm 0.2$ dex is shown around the analytic fit line (light grey strip). . . . .	78
A.1	FUV SED between 6 - 13.6 eV . . . . .	92
A.2	LW SED between 11.2 - 13.6 eV . . . . .	93
B.1	Attenuation term $N_H^{-\phi-1}$ . . . . .	95
B.2	$S(\tau_X)$ using <code>scipy.special</code> . . . . .	96
B.3	$S(\tau_X)$ using <code>mpmath</code> . . . . .	97
B.4	$B \equiv \frac{S(\tau_X)}{\tau_X^{\phi+1}}$ . . . . .	98
B.5	Comparison of the analytic and numerical form of $S(\tau_X)N_H^{-\phi-1}$ . . . . .	99
B.6	Attenuation region of analytic and numerical form of $S(\tau_X)N_H^{-\phi-1}$ . . . . .	100
C.1	Analytic fit to the HXR perturbation curve for $\tilde{\sigma}_d = 0.01$ and $\alpha G = 0.01$ . . . . .	101
C.2	Analytic fit to the HXR perturbation curve for $\tilde{\sigma}_d = 0.1$ and $\alpha G = 0.01$ . . . . .	102
C.3	Analytic fit to the HXR perturbation curve for $\tilde{\sigma}_d = 1$ and $\alpha G = 0.01$ . . . . .	103
C.4	Analytic fit to the HXR perturbation curve for $\tilde{\sigma}_d = 10$ and $\alpha G = 0.01$ . . . . .	104
C.5	Analytic fit to the HXR perturbation curve for $\tilde{\sigma}_d = 0.01$ and $\alpha G = 0.1$ . . . . .	105
C.6	Analytic fit to the HXR perturbation curve for $\tilde{\sigma}_d = 0.1$ and $\alpha G = 0.1$ . . . . .	106
C.7	Analytic fit to the HXR perturbation curve for $\tilde{\sigma}_d = 1$ and $\alpha G = 0.1$ . . . . .	107
C.8	Analytic fit to the HXR perturbation curve for $\tilde{\sigma}_d = 10$ and $\alpha G = 0.1$ . . . . .	108
C.9	Analytic fit to the HXR perturbation curve for $\tilde{\sigma}_d = 0.01$ and $\alpha G = 1$ . . . . .	109
C.10	Analytic fit to the HXR perturbation curve for $\tilde{\sigma}_d = 0.1$ and $\alpha G = 1$ . . . . .	110
C.11	Analytic fit to the HXR perturbation curve for $\tilde{\sigma}_d = 1$ and $\alpha G = 1$ . . . . .	111
C.12	Analytic fit to the HXR perturbation curve for $\tilde{\sigma}_d = 10$ and $\alpha G = 1$ . . . . .	112
C.13	Analytic fit to the HXR perturbation curve for $\tilde{\sigma}_d = 0.01$ and $\alpha G = 10$ . . . . .	113

C.14 Analytic fit to the HXR perturbation curve for  $\tilde{\sigma}_d = 0.1$  and  $\alpha G = 10$  . . . . . 114  
C.15 Analytic fit to the HXR perturbation curve for  $\tilde{\sigma}_d = 1$  and  $\alpha G = 10$  . . . . . 115  
C.16 Analytic fit to the HXR perturbation curve for  $\tilde{\sigma}_d = 10$  and  $\alpha G = 10$  . . . . . 116

# Chapter 1

## Introduction

Interstellar gas clouds are regions that are dominated by the existence of molecular hydrogen ( $\text{H}_2$ ) as well as dust grains which are intermixed with the hydrogen. These gas clouds can be exposed to sources of radiation ranging from the optical, ultraviolet, and through to the X-ray regime. There are two significant processes that can occur in these clouds that lead to regions where atomic hydrogen ( $\text{H}^0$ ) is dominant over molecular hydrogen and it is these processes that will be the focus of this dissertation. The aforementioned regions of atomic hydrogen are primarily caused by the dissociation of molecular hydrogen due to fluxes of far-ultraviolet radiation (FUV) and/or hard X-ray radiation (HXR). As the radiation fields are attenuated through the cloud, the amount of molecular hydrogen increases and these regions that are shielded from radiation can undergo star formation. The transition point where the gas goes from being predominantly atomic hydrogen to that of molecular hydrogen is of interest here.

The galactic sources of these radiation fields can include bright O and B stars which produce significant amounts of FUV radiation. As these star-forming regions can contain O stars with short lifetimes ( $\sim$  a few million years) it is possible that there may exist an accretion disk around a compact object. This would emit a radiation field in the HXR spectrum that would shift the transition point compared to it not being there. For example an object with a luminosity of  $L_X \sim 10^{40} \text{ erg s}^{-1}$  at a distance of  $r \sim 30 \text{ ly}$  would have an energy flux of  $F_X \sim 1 \text{ erg cm}^{-2} \text{ s}^{-1}$  at the cloud face. It is this response to the transition point due to the HXR radiation field that will be modeled in this dissertation.

Photodissociation regions (PDRs), also known as photon dominated regions, are those char-

acterized by exposure to far-ultraviolet radiation fields in the 6 - 13.6 eV range. The interaction of the FUV radiation field that is in the 11.2 - 13.6 eV range with molecular hydrogen proceeds by absorption into excited electronic states which can then undergo radiative decay into atomic hydrogen or else into excited rovibrational levels of the ground electronic state.

The attenuation of the radiation by absorption as well as dust opacity leads to a reduction in the FUV radiation field. From this then, as well as the the formation of  $\text{H}_2$  from atomic hydrogen in dust grain catalyzed reactions, there exist atomic-to-molecular hydrogen transition points, namely where  $n_{\text{H}^0} = 2n_{\text{H}_2}$ .

X-ray dissociation regions (XDRs), also known as X-ray dominated regions, are regions where the interaction of high energy photons ( $E \gtrsim 1 \text{ keV}$ ) with molecular hydrogen is due to direct photoionization along with subsequent ionization from secondary electrons. These secondary electrons can also excite  $\text{H}_2$  leading to the production of LW-band photons capable of further dissociating molecular hydrogen. Due to the small cross-section for ionization the hard X-ray field (1-100 keV) has  $\text{H}^0$ -to- $\text{H}_2$  transition points that occur at greater column densities than in PDRs.

The difference in nomenclature between photodissociation region and photon dominated region is due the different modeling of the internal chemistry. The naming of photon dominated regions was first given by models that include cosmic-ray ionizations [1], whereas photodissociation regions assume that the dissociation of molecular hydrogen is mainly due to LW-band photons. As the model of the PDR in this dissertation is based on the latter [2], the term photodissociation region is used throughout both. A similar rationale for naming conventions is given in the case of X-ray dissociation regions and X-ray dominated regions. The model used in this dissertation for the XDR is based on an HXR radiation field [3], so the term X-ray dissociation region is used here as it is in the original paper. This varies from the more modern term X-ray dominated region [4].

The photodissociation of molecular hydrogen due to a FUV radiation field mostly occurs due to the absorption of LW-band photons into bound excited states which then subsequently decay. One of these decay pathways leads to the direct dissociation of  $\text{H}_2$  into its constituent hydrogen atoms in an interaction known as the Solomon process [5].

In the case of an HXR radiation field, direct photoionization of molecular hydrogen leads to a cascade of additional ionizations due the primary photoelectron. These ions react chemically with the gas causing further  $\text{H}_2$  dissociations. The interaction of the secondary electrons with molecular

hydrogen causes excitation into bound excited states which produce an internal FUV radiation field. This internal field can then cause further dissociation due to the Solomon process.

The literature in the study of PDRs and XDRs is extensive and only a partial list of such research will be given here. This includes the modeling of the interstellar radiation field [6, 7, 8], the effects of molecular hydrogen self-shielding [9, 8, 10, 11, 12, 2], the interaction of FUV radiation with dust grains [13], the formation of hydrogen on dust grains [14, 15], the modeling of steady state PDRs [8, 12, 2, 16] and the sources, interactions and modeling of X-ray fields [17, 18, 3, 19]. Review articles discussing PDRs, XDRs and their combinations include [20, 21, 22, 23, 24, 25].

Of interest in this dissertation is the identification of the total integrated energy flux at the transition point in the HXR range that would lead to a response in the transition points of an FUV only PDR model. This model is based on the combination of two existing models for PDRs and XDRs. The flux of hard X-rays is increased until a shift in the transition point of the FUV only model is shifted to greater column densities. This is done with an HXR attenuation model that doesn't have significant attenuation until a total hydrogen column density of  $N_{\text{H}} \gtrsim 10^{21} \text{ cm}^{-2}$  is reached, as well as a simplified HXR attenuation model that is being continuously attenuated across all column densities. An analytic fit is given for the response of the simplified attenuation function.

This dissertation starts off in Chapter 2 with the theory leading to the steady-state creation-destruction model of a photodissociation region (PDR). The first steps are discussing details of the FUV radiation field and its ability to dissociate molecular hydrogen in §§ 2.1.1 - 2.1.2.1. This includes details on the Draine spectral energy distribution (SED) [7] that is commonly used in PDR modeling as well as how the Solomon process leads to an efficient dissociation mechanism for  $\text{H}_2$  [5]. Appendix A describes methods to convert between various forms of FUV SEDs that are commonly encountered in the literature. The attenuation of the FUV radiation field due to extinction from dust grains and the reduction of the field from the effect of self-shielding is given in §§ 2.1.3 - 2.1.3.3. The formation routes of molecular hydrogen is in §§ 2.1.4 - 2.1.4.2 with emphasis given to the formation mechanisms via dust grains as that is what this model is based upon.

There are many models of PDR regions that have been developed as well as advanced codes used for their computation [26]. The steady-state model used for the creation-destruction of molecular hydrogen in this dissertation is based on those of Sternberg, Bialy, et al.[2, 16] in § 2.2.

Chapter 3 details the model that was used for the X-ray dissociation (XDR) region due to a hard X-ray spectrum (HXR). The basis for this model is that developed by Maloney, Hollenbach, and Tielens [3]. In §§ 3.1.1 - 3.1.2 the details involving the SED for a HXR field are given. This includes the energy deposition due to the X-rays and the secondary non-thermal electrons that are produced by the primary photoelectron. Appendix B gives further details on the energy deposition due to hard X-rays. The interaction of the non-thermal electrons with  $\text{H}_2$  causes rovibrational excitation and transitions to LW-band energy levels which can then produce an internal FUV radiation field is described in § 3.2.1 [27, 28, 29].

The steady-models used in §§ 3.2, 3.4 and, 3.4 all have the same general form as that given in § 2.2.

The analytic modeling and the computational results of the response of the PDR transition points to an HXR field is contained in Chapter 4. In § 4.1 the equations for the determination of the density profiles for the PDR model used are given. As a test for the code, the analytic model for the density profiles from [16] is used where their attenuation function  $G$  was replaced by the total hydrogen column density dependent function  $A$ . The results of these transition points and their comparison are discussed in §§ 4.1 - 4.2.2.

The model for the response of the PDR to an HXR radiation field is in § 4.3. This creation-equation combines the transition point of the FUV only PDR with a linear response due to HXR radiation field with its associated internally generated FUV radiation. The computational results of the response using the the exact analytic model for the energy deposition rate  $H_X$  are given in § 4.4.1. Given are transition point response curve and an example of density profiles for an increase in the transition point by one order of magnitude. The computational results of approximation to the energy deposition is given in § 4.4.2 with the same plots described above. In § 4.5 a simple analytic model is given that gives the transition point response curve as a function of the transition point due to a independent PDR model and an HXR model.

The conclusions of this dissertation and possible future work is given in § 5.

# Chapter 2

## PDR - Model

### 2.1 Physical Processes

The basic equation for the creation-destruction of  $\text{H}_2$  in steady state, isothermal, non-turbulent conditions with a low ionization fraction ( $x_e \lesssim 10^{-3}$ ) for a beamed far-ultraviolet (FUV) radiation field into an optically thick plane parallel slab is given by

$$R_d n(\text{H}^0) n(\text{H}) = \frac{1}{2} D_U f_{\text{att},U} n(\text{H}_2) \quad [\text{cm}^{-3} \text{s}^{-1}]. \quad (2.1)$$

The left side of Eq. (2.1) represents the formation rate per unit volume of molecular hydrogen,  $\text{H}_2 \text{ cm}^{-3} \text{s}^{-1}$ , and conversely, the right hand side is the destruction rate per unit volume of  $\text{H}_2$  with the same units. The volumetric formation rate of  $\text{H}_2$  is dependent upon the formation rate coefficient  $R_d \text{ cm}^3 \text{s}^{-1}$ , the atomic hydrogen number density  $n(\text{H}^0) \text{ cm}^{-3}$ , and the total hydrogen nuclei number density  $n(\text{H}) \text{ cm}^{-3}$ . The factor of  $1/2$  comes from the reduction in the surface flux density of a total free-space radiation field when an optically thick semi-infinite slab is inserted and the impinging field is considered to be beamed. The volumetric destruction rate of  $\text{H}_2$  due to an FUV radiation field depends on the free space photodissociation rate  $D_U \text{ s}^{-1}$ , the dimensionless effective depth dependent attenuation of the radiation field  $f_{\text{att},U}$ , and the molecular hydrogen number density  $n(\text{H}_2)$ . The volumetric number densities shall be denoted as  $n(\text{H}^0)$ ,  $n(\text{H}_2)$ , and  $n(\text{H})$  by  $n_{\text{H}^0}$ ,  $n_{\text{H}_2}$ , and  $n_{\text{H}}$  respectively. The total hydrogen nuclei number density, (i.e. proton

number density), is conserved so that

$$n_{\text{H}} \equiv n_{\text{H}^0} + 2n_{\text{H}_2}. \quad (2.2)$$

The terms in equation (2.1) will be described in greater detail in §§ (2.1.1) - (2.2) below. A similar equation will also be given for an X-ray dissociation region in § (3.1) which examines the atomic-to-molecular ( $\text{H}^0$ -to- $\text{H}_2$ ) transition region due to a hard X-ray spectrum. § (3.1.2) will also discuss how an increasing ionization fraction affects the molecular hydrogen destruction rate.

### 2.1.1 Ultraviolet Radiation Field

The interstellar ultraviolet (UV) radiation field is particularly important in the destruction of molecular hydrogen. The broad UV field is considered to have a wavelength of between 100 Å and 4000 Å; however, the FUV region of this spectrum has wavelengths,  $\lambda$  that are in the range of  $912 \text{ Å} < \lambda < 3000 \text{ Å}$  [30]. This region is of interest since photons with wavelengths less than 3000 Å have enough energy to cause ionization [6]. The extreme ultraviolet field (EUV) is in the  $100 \text{ Å} < \lambda < 912 \text{ Å}$  range [30]. These fields exist primarily due to hot O and B stars.

The specific intensity distribution function,  $I_\nu$  is defined mathematically as

$$I_\nu = \frac{dE_\nu}{d\sigma dt d\nu d\omega} \quad [\text{erg cm}^{-2} \text{ s}^{-1} \text{ Hz}^{-1} \text{ sr}^{-1}], \quad (2.3)$$

where  $I_\nu$  is the frequency dependent specific intensity,  $\theta$  and  $\phi$  are the polar and azimuthal angle respectively that are made with respect to the source of the radiation and the observer,  $dE_\nu$  is the amount of energy per unit frequency crossing the detector,  $d\sigma$  is the unit area at the detector, and  $d\omega$  is the solid angle subtended by the detector. The specific intensity can also be given in terms of other quantities such as wavelength or photon number. For example, a frequency dependent specific intensity can be related to a wavelength dependent one through the differential relation  $I_\nu d\nu = I_\lambda d\lambda$ .

Assuming that there is no time dependence of the intensity, the specific intensity can be given in terms of the energy density of the radiation field by defining a characteristic length  $s = ct$ , so

that  $1/dt = c/ds$  and then equation (2.3) becomes

$$I_\nu = \frac{c dE_\nu}{dV d\nu d\omega} \quad [\text{erg cm}^{-2} \text{s}^{-1} \text{Hz}^{-1} \text{sr}^{-1}], \quad (2.4)$$

where  $dV \equiv d\sigma ds$ , and  $c = 2.998 \times 10^{10} \text{ cm s}^{-1}$  is the speed of light.

The interstellar energy density at the wavelengths of 1000 Å, 1400 Å, and 2400 Å was calculated by Habing with a frequency specific energy density of  $\nu u_\nu = 4 \times 10^{-14} \text{ erg cm}^{-3}$  at 1000 Å [6]. There have been numerous updates and modifications to these values, a representative table of some of which can be found in [12]. One such fit for Habing's values is given by [12]

$$\lambda u_{\lambda, \text{Habing}} = \left( -\frac{25}{6} \lambda_3^3 + \frac{25}{2} \lambda_3^2 - \frac{13}{3} \lambda_3 \right) \times 10^{-14} \quad [\text{erg cm}^{-3}], \quad (2.5)$$

where  $\lambda_3 \equiv \lambda/10^3 \text{ Å}$ . The integrated (full  $4\pi$ ) energy density of this UV SED is found by

$$u_{\lambda, \text{Habing}} = \int_{\lambda_1}^{\lambda_2} (-4.167 \times 10^{-23} \lambda^2 + 12.5 \times 10^{-20} \lambda - 4.333 \times 10^{-17}) d\lambda \quad [\text{erg cm}^{-3}], \quad (2.6)$$

where  $\lambda_1$  is generally taken to be the ionization wavelength of atomic hydrogen (912 Å). With this the energy and photon flux are given respectively by

$$F_{\lambda_E, \text{Habing}} = c \int_{\lambda_1}^{\lambda_2} u_{\lambda, \text{Habing}} d\lambda \quad [\text{erg cm}^{-2} \text{s}^{-1}], \quad (2.7a)$$

$$F_{\lambda_\gamma, \text{Habing}} = \frac{1}{h} \int_{\lambda_1}^{\lambda_2} \lambda u_{\lambda, \text{Habing}} d\lambda_3 \quad [\text{photon cm}^{-2} \text{s}^{-1}], \quad (2.7b)$$

and where  $c = 2.998 \times 10^{10} \text{ cm s}^{-1}$ ,  $h = 6.626 \times 10^{-27} \text{ g cm}^2 \text{s}^{-1}$ , and  $d\lambda_3$  has dimensions of  $10^{-8} \text{ cm}$  for equation (2.7b) to be dimensionally correct since. Habing considers the radiation energy density between 912 and 2400 Å (or equivalently between 13.598 and 5.166 eV respectively). Within these ranges and using equations (2.5) - (2.7b), the spectrum has a (full  $4\pi$ ) integrated energy density of  $6.21 \times 10^{-14} \text{ erg cm}^{-3}$ , an integrated energy flux of  $1.86 \times 10^{-3} \text{ erg cm}^{-2} \text{s}^{-1}$ , and an integrated photon flux of  $1.50 \times 10^8 \text{ photon cm}^{-2} \text{s}^{-1}$ . This radiation field is often denoted as  $G_0$  in the literature [8].

A radiation field in the far-ultraviolet regime that is commonly used in the study of photodissociation regions is the Draine standard ultraviolet radiation field [7]. This radiation field is an

analytic fit based on previous theoretical and observational work [6, 15, 31, 32, 33, 34, 35]. It describes a free-space isotropic far-ultraviolet radiation field between 5 and 13.598 eV (or equivalently between 2480 and 912 Å respectively).

This can be written in terms of a specific photon intensity distribution as a function of photon energy by [7]

$$F_{E,\text{Draine}} = (1.658 \times 10^6 (E_e) - 2.152 \times 10^5 (E_e)^2 + 6.919 \times 10^3 (E_e)^3) \quad [\text{photon cm}^{-2} \text{s}^{-1} \text{sr}^{-1} \text{eV}^{-1}], \quad (2.8)$$

where  $E_e \equiv (E/1\text{eV})$ . The integrated photon and energy flux of this energy distribution over the relevant energy ranges are given respectively by

$$F_{E_\gamma,\text{Draine}} = \int_{E_{e1}}^{E_{e2}} \int_{\Omega} (1.658 \times 10^6 (E_e) - 2.152 \times 10^5 (E_e)^2 + 6.919 \times 10^3 (E_e)^3) d\Omega dE_e \quad [\text{photon cm}^{-2} \text{s}^{-1}], \quad (2.9a)$$

$$F_{E_E,\text{Draine}} = \int_{E_{e1}}^{E_{e2}} \int_{\Omega} (1.658 \times 10^6 (E_e)^2 - 2.152 \times 10^5 (E_e)^3 + 6.919 \times 10^3 (E_e)^4) d\Omega dE_e \quad [\text{eV cm}^{-2} \text{s}^{-1}], \quad (2.9b)$$

and where

$$\int_{\Omega} d\Omega = \int_0^{2\pi} \int_0^\pi \sin \theta d\theta d\phi. \quad (2.10)$$

The evaluation of this integral gives  $\int_{\Omega} d\Omega = 4\pi$ . Conversion of equation (2.9b) into dimensional units of  $\text{erg cm}^{-2} \text{s}^{-1}$  is given with  $1 \text{ eV} = 1.602 \times 10^{-12} \text{ erg}$ . With this then equation (2.9b) becomes

$$F_{E_{\text{erg}},\text{Draine}} = 1.602 \times 10^{-12} F_{E_E,\text{Draine}} \quad [\text{erg cm}^{-2} \text{s}^{-1}]. \quad (2.11)$$

The energy density of the Draine UV spectrum can then be found from equation (2.9b) as

$$u_{E,\text{Draine}} = \frac{1}{c} F_{E_{\text{erg}},\text{Draine}} \quad [\text{erg cm}^{-3}]. \quad (2.12)$$

This field has an integrated photon flux of  $2.42 \times 10^8 \text{ photons cm}^{-2} \text{s}^{-1}$  over the 5 - 13.6 eV range. The integrated energy flux of equation (2.8) is  $1.932 \times 10^9 \text{ eV cm}^{-2} \text{s}^{-1}$  or equivalently

$3.11 \times 10^{-3} \text{ erg cm}^{-2} \text{ s}^{-1}$  over the same energy range. The energy density of this field is  $1.04 \times 10^{-13} \text{ erg cm}^{-3}$  in this same range. There are various forms of equation (2.8) in the literature [12, 2, 36, 37, 38].

Since equations (2.8) - (2.12) represent the full free-space Draine FUV radiation field, i.e.,  $F(0) = 4\pi F_0$ , where  $F_0$  is any particular specific flux intensity distribution that has been already been integrated over its relevant functional dependency, a semi-infinite slab inserted into the field will cause a decrease in the surface flux density across the cloud. For a beamed field the angular integration modifies the angular portion of the free space field to  $\int_0^{2\pi} \int_0^{\pi/2} \sin \theta d\theta d\phi = 2\pi$ . The surface flux density of the beamed field is then one half of the free-space field and

$$F_{\text{Bea}}(0) = \frac{1}{2} F_0 \quad [\text{erg cm}^{-2} \text{ s}^{-1}]. \quad (2.13)$$

For a semi-infinite slab inserted into an isotropic Draine FUV radiation field, the angular portion of the surface flux density is reduced to  $\int_0^{2\pi} \int_0^{\pi/2} \sin \theta \cos \theta d\theta d\phi = \pi$ . The surface flux density of the isotropic field is then one quarter of the free-space field and

$$F_{\text{Iso}}(0) = \frac{1}{4} F_0 \quad [\text{erg cm}^{-2} \text{ s}^{-1}]. \quad (2.14)$$

These relations also hold for the surface flux densities of the Habing FUV field, equation (2.7a). Further details on these FUV spectral distributions as well as the distribution given in [2] are found in Appendix A.

### 2.1.2 Molecular Hydrogen Destruction

The bond energy of molecular hydrogen,  $\text{H}_2$ , is 4.476 eV, or a wavelength equivalent of 2770 Å. Dissociation, however, does not occur directly at this energy via photon absorption through the photodissociation reaction



This radiative dissociation reaction has an extremely small rate coefficient ( $\lesssim 10^{-23} \text{ cm}^3 \text{ s}^{-1}$ ) due to the forbidden transition by the  $\Delta S = 0$  selection rule [14, 39]. This is because the hydrogen molecule is a homonuclear diatom and thus has no dipole moment since the net dipole coordinate

coincides with the geometrical center of mass of the molecule. Due to this, there are no pure vibrational electric dipole-allowed transitions which would excite the molecule to the vibrational dissociation continuum limit ( $\nu \geq 14$ ). Since this is a forbidden transition there needs to be other mechanisms which will allow the separation of molecular hydrogen into its constituent atoms.

Moving to the higher end of the UV energy spectrum required for  $\text{H}_2$  destruction, photons with an energy of greater than 15.426 eV, or equivalently, wavelengths shortward of 804 Å are capable of photoionizing the  $\text{H}_2$  molecule.  $\text{H}_2$  is photoionized in the reaction



The dissociation energy of the hydrogen molecular ion,  $\text{H}_2^+$ , is 2.8 eV, however like the hydrogen molecule, a greater energy than the binding energy is required for destruction. A minimum energy of 12.5 eV, or an equivalent wavelength of less than 992 Å from the ground state of  $\text{H}_2^+$  leads to the photodissociation reaction [40, 41]



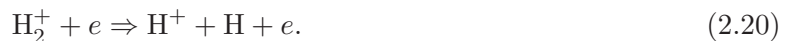
with the  $\text{H}^0$  atom being left in the ground state. If the energy for excitation to higher discrete electronic states of  $\text{H}_2^+$  is between 19 and 30 eV, or a wavelength equivalent of 413 to 653 Å the photodissociation reaction



can occur leading to a hydrogen atom in an excited state which can then decay or be ionized. For photon energies greater than 30 eV, or equivalently wavelengths less than 413 Å excitation into the continuum state can occur giving the dissociative ionization reaction



The destruction of  $\text{H}_2^+$  also occurs through a gas-phase chemistry dissociative recombination reaction



Direct photodissociation of  $\text{H}_2$  at energies greater than the Lyman (photoionization) limit occurs at an energy of 14.671 eV through the absorption of a  $\lambda < 850 \text{ \AA}$  photon leading to [5]



with the excited  $\text{H}^0$  atom being in the 2s or 2p state.

The destruction of  $\text{H}_2$  due to photons at these energies or greater leads to a layer of atomic hydrogen that has built up in front of the molecular hydrogen layer. This layer of atomic hydrogen is further stratified into a front of ionized hydrogen that is facing the radiation field and a thin boundary layer of  $\text{H}^+$  and  $\text{H}^0$  where the transition from mostly ionized hydrogen to atomic hydrogen occurs. Beyond this transition point the photodissociation region proper is entered. The hydrogen in this region is neutral and consists of a layer of atomic hydrogen with a transition region where the destruction of molecular hydrogen diminishes and the gas becomes predominantly molecular.

With the ionization energy of  $\text{H}^0$  being 13.598 eV, then photons with wavelengths shortward of 912  $\text{\AA}$  are attenuated in the process of ionizing  $\text{H}^0$  [42, 43]. Thus, due to destruction of  $\text{H}_2$  with photons shortward of 912  $\text{\AA}$  and the ionization of  $\text{H}^0$  in the reaction



the photodissociation region contains photons with wavelengths longward of 912  $\text{\AA}$ . Since photons with  $\lambda < 850 \text{ \AA}$  are absorbed in the ionization of atomic hydrogen, the pathway to direct photodissociation as in equation (2.21) is absent.

If photons have energies greater than the  $\text{H}_2$  bond dissociation energy of 4.476 eV, there is a pathway to direct photodissociation; however the reaction leading to  $X^1\Sigma_g^+ \rightarrow b^3\Sigma_u^+$  is a singlet-triplet transition which changes the spin multiplicity and is a forbidden transition [5]. There are also forbidden transitions to the triplet states  $a^3\Sigma_g^+$  and  $c^3\Pi_u$  from the  $X^1\Sigma_g^+$  state as well as allowed transitions from the repulsive  $b^3\Sigma_u^+$  to the  $a^3\Sigma_g^+$  and  $c^3\Pi_u$  states. The former state has allowed transitions to the repulsive  $b^3\Sigma_u^+$  state leading to dissociation, while the latter has allowed transitions to the  $b^3\Sigma_u^+$  via the  $a^3\Sigma_g^+$  state for vibrational levels  $\nu \geq 1$ . The  $c^3\Pi_u$  ( $\nu = 0$ ) state is metastable and can decay to the repulsive  $b^3\Sigma_u^+$  via a magnetic dipole transition [5, 44]. However,

due to the multipole nature of these transitions, these reactions do not play a significant role in the dissociation of  $\text{H}_2$ .

The convention for the prefix of the molecular state of hydrogen is that the ground singlet is state is denoted by  $X$ . Excited electronic states of the same multiplicity as the ground electronic state have prefixes of  $A, B, C$ , etc. in terms of increasing energy. For states with multiplicity that is different from the ground electronic state, the prefixes used in terms of increasing energy are  $a, b, c$ , etc.

### 2.1.2.1 Solomon Process

The favored reactions for the dissociation of  $\text{H}_2$  at energies less than the Lyman (photoionization) limit of  $\text{H}^0$  occur through what is called the Solomon process (P.M. Solomon, private communication, 1965, in [5] pg.226). There are allowed electric dipole transitions from the ground state of  $\text{H}_2$  to two excited states at minimum energies of 11.2 and 12.3 eV. These excited states are the  $B^1\Sigma_u^+$  and  $C^1\Pi_u$  respectively as there is no bound  $A^1\Sigma$  state. The former is known as the Lyman band transition and the latter as the Werner band transition after whom had first observed their respective band systems [45, 46, 47].

In cold molecular clouds,  $T \sim 100$  K, essentially all of the hydrogen molecules are in the ground vibrational state. Rotational levels within the ground vibrational level are typically in the first or second rotational energy level. The photon energy spectrum related to these transitions are infrared for vibrational transitions and microwave for rotational transitions.

The electric dipole transition rules for transitions between the ground and excited electronic states include the change in projection of the total angular momentum along the internuclear axis,  $\Lambda = 0, \pm 1$ . This leads to the  $\Lambda = 0, \Sigma$  state; and the  $\Lambda = 1, \Pi$  state. These rules allow for  $\Sigma \rightarrow \Sigma$  and  $\Sigma \rightarrow \Pi$  transitions. There is also the change in spin multiplicity of  $\Delta S = 0$ . This rule leads to the excited states having singlet spin multiplicity since the ground state has this spin multiplicity, i.e.  $^1\Sigma \rightarrow ^1\Sigma$  and  $^1\Sigma \rightarrow ^1\Pi$  transitions. There are also symmetry rules for dipole transitions. One is for the parity of the molecular wavefunction upon reflection of the electronic coordinates about an internuclear plane containing the nuclei. For  $\Sigma$  states, there is no net orbital angular momentum and so also a lack of degeneracy of the wavefunction upon reflection. Thus the molecule is either in the parity unchanged  $\Sigma^+$ , or parity changed  $\Sigma^-$  state and the dipole selection

rules due to non-degeneracy lead to  $\Sigma^+ \rightarrow \Sigma^+$  and  $\Sigma^- \rightarrow \Sigma^-$ . For states with  $\Lambda \geq 1$ , there is a net angular momentum projection onto the internuclear axis and so there exists a degeneracy of states upon reflection of the electronic coordinates. This is annotated by  $\Pi^\pm$  as an example for the  $\Lambda = 1$  state. The dipole transition rules for the reflection operator are then given by  $\Sigma^+ \rightarrow \Pi^\pm$  and  $\Sigma^- \rightarrow \Pi^\pm$ . Since the ground state of  $\text{H}_2$  is  $\Sigma^+$  the former rule applies. Since all states with  $\Lambda \geq 1$  have this degeneracy, the convention is to suppress the  $\pm$  notation so that, e.g.  $\Pi^\pm \rightarrow \Pi$ . As  $\text{H}_2$  is homonuclear, there also is a symmetry regarding an inversion of electronic coordinates,  $(x, y, z) \rightarrow (-x, -y, -z)$ , through the geometric center of the molecule. This operation on the electronic wavefunction either changes the parity (*ungerade*,  $u$ ) or leaves it unchanged (*gerade*,  $g$ ). This operator is often denoted by  $\hat{P}$ . The dipole selection rule for this operation is  $g \rightarrow u$  or  $u \rightarrow g$ . As the ground state of  $\text{H}_2$  is  $\Sigma_u$  the latter rule applies.

The electric dipole selection rules for rotational transitions determine the rotational state of the molecule upon absorption of a Lyman-Werner band photon. The particular selection rules for a given molecule depend on the type of “coupling scheme” that is used. In the case of  $\text{H}_2$ , Hund’s coupling case (b) is used whereby the orbital angular momentum of the electrons,  $\mathbf{L}$ , has a well defined projection upon the internuclear axis,  $\Lambda$ . This is then coupled to the rotational angular momentum of the nuclei,  $\mathbf{R}$ . The addition of these gives the spin excluded total angular momentum of the molecule such that  $\mathbf{N} = \mathbf{R} + \mathbf{\Lambda}$ . The spin angular momentum of the electrons,  $\mathbf{S}$  is then coupled to this vector to give the total angular momentum of the molecule,  $\mathbf{J} = \mathbf{N} + \mathbf{S}$ . The rotational transition selection rule for the total angular momentum is given by  $\Delta J = 0, \pm 1$  provided  $0 \leftrightarrow 0$ . The spin excluded total angular momentum selection rule is  $\Delta N = 0, \pm 1$  where  $\Delta N \neq 0$  for  $\Sigma \leftrightarrow \Sigma$ . There are also parity selection rules regarding the nuclear spin wavefunctions. If the total molecular wavefunction excluding nuclear spin is symmetric and is combined with an anti-symmetric nuclear spin wavefunction, then the rovibrational levels are symmetric regarding  $\hat{P}$  and are denoted  $s$ . If the symmetry/anti-symmetry of the previous wavefunctions are reversed, then the rovibrational levels are anti-symmetric regarding  $\hat{P}$  and are denoted  $a$ . The selection rules for nuclear symmetry are  $s \leftrightarrow s$ ,  $a \leftrightarrow a$ ,  $s \leftrightarrow a$ . There are also rotational states due to the spin of the nuclei. When they are aligned anti-parallel the net nuclear spin,  $I$  is even and is called *para* hydrogen. When they are aligned in parallel,  $I$  is odd and is called *ortho* hydrogen. In cold molecular clouds, the ground state of  $\text{H}_2$  is predominantly in the  $J = 0$  and the  $J = 1$  states

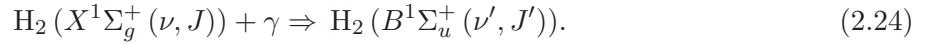
corresponding to  $I = 0$  and  $I = 1$  states. The degeneracy of these states in equilibrium due to the Boltzmann distribution is in the ratio of 1:3 for *para* to *ortho* [48]. Electric-quadrupole transitions determine the rotational transitions and so have the transition rules  $\Delta J = 0, \pm 2$ .

For transitions between vibrational levels, there aren't selection rules regarding the vibrational states. These transitions are governed by the Franck-Condon principle which gives greater probability for transitions to occur that minimize the change in kinetic energy of the molecule. Thus the square of the transition dipole moment between different electronic states and the square of the overlap integral between vibrational wavefunctions in these electronic states will have a greater likelihood of occurring if internuclear separation is minimized during the transition. As discussed earlier, at cold molecular cloud temperatures  $T \sim 100$  K, the ground  $X^1\Sigma_g^+$  state is typically in the  $\nu = 0$  vibrational level and  $J = 0$  or 1. The transition strength of a particular line absorption is given by

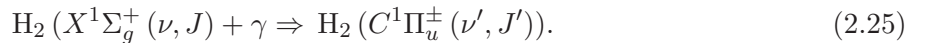
$$a_\nu = a f \phi_\nu \quad [\text{cm}^2 \text{s}^{-1} \text{Hz}^{-1}] \quad \text{where} \quad a = \frac{\pi e^2}{m_e c} \quad [\text{cm}^2 \text{s}^{-1}]. \quad (2.23)$$

Here  $a$  is the total atomic absorption coefficient,  $f$  is the oscillator strength related to the induced Einstein absorption coefficient  $B_{lu}$  (and hence spontaneous Einstein emission coefficient and the induced Einstein emission coefficient,  $A_{ul}$  and  $B_{ul}$  respectively), and  $\phi_\nu$  is the line profile. Details of these rules can be found in various sources on molecular physics [49, 50, 51]. Further discussion of equation (2.23) will be given in § 2.1.3.2.

In the Lyman band transition, photons shortward of 1108 Å can be absorbed into the first excited singlet electronic state through



In the Werner band transition, photons shortward of 1008 Å can be absorbed into the second excited singlet electronic state through



For absorptions in the Lyman-Werner band, there are a few different decay mechanisms that can occur. The least likely, but the one that is most significant for the creation of atomic hydrogen

is a decay into the vibrational continuum of  $\text{H}_2$  at 4.476 eV. This leads to the dissociation of the hydrogen molecule. In this process, there is a fluorescent decay from the  $B^1\Sigma_u^+$  or  $C^1\Pi_u$  into an unbound ( $\nu \geq 14$ ) vibrational level of the  $X^1\Sigma_g^+$  state given rise respectively to the radiative dissociation reaction

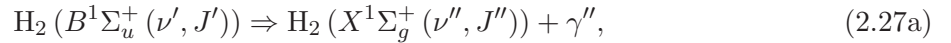


or

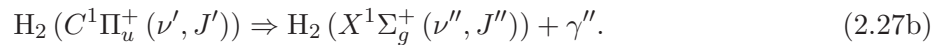


where  $\gamma'$  is of longer wavelength than the respective  $\gamma$  for absorption. Dissociation from the Lyman band has a greater probability than the Werner band and various researchers have determined these probabilities [43, 48, 52, 53, 54, 55, 56, 57, 58]. A mean dissociation probability for  $\text{H}_2$  for a transition from the LW band for a Draine FUV radiation spectrum has been calculated as  $\langle f_d \rangle = 0.12$  [2].

For decays that don't lead to dissociation, then the molecule de-excites through a radiative transition to one of the excited rovibrational states of the ground electronic state of  $\text{H}_2$  through



or



Molecules that are in excited rovibrational levels of the ground electronic state can undergo electric quadrupole transitions in an infrared cascade [12, 59, 60, 61, 62, 11, 1, 63]. For UV radiation fields of sufficient intensity, then molecules in an excited vibrational level of the ground electronic state ( $2 \leq \nu \leq 13$ ) have the possibility of being directly photodissociated ( $\nu \geq 3$ ), of being re-pumped into an excited  $B^1\Sigma_u^+$  or  $C^1\Pi_u^+$  state, or of being directly photoionized [43, 64, 61].

### 2.1.3 Attenuation of Ultraviolet Radiation

The attenuation of FUV radiation decreases the destruction rate of  $\text{H}_2$  as it is absorbed or scattered by dust particles and also by the removal of preferential photons with the Solomon process of

dissociating  $\text{H}_2$ . With this then the attenuation term in equation (2.1) is

$$f_{\text{att},U}(N_{\text{H}}, N_{\text{H}_2}) = f_{\text{d},U}(N_{\text{H}}) f_{\text{s},U}(N_{\text{H}_2}) \quad (2.28)$$

where  $f_{\text{d},U}(N_{\text{H}})$  is the total hydrogen column density dependent dust attenuation term,  $f_{\text{s},U}(N_{\text{H}_2})$  is the molecular hydrogen column density dependent self-shielding term, and  $N_{\text{H}} \equiv N_{\text{H}^0} + 2N_{\text{H}_2}$  is the total hydrogen column density. To find the column density, one integrates along the line of sight which gives a projected number density contained in a cylinder of unit area. For the total hydrogen column density this is given by

$$N_{\text{H}} \equiv \int n_{\text{H}}(s') ds' \quad [\text{cm}^{-2}] \quad (2.29)$$

where for a planar slab intervening between the object and the detector along the line of sight that has a fixed total hydrogen number density, the limits of integration are  $\int_{s'=0}^{s'=s}$  and the total hydrogen column density simply becomes  $N_{\text{H}} = n_{\text{H}} s \text{ [cm}^{-2}\text{]}$ . Aspects of the physics discussed in this section can be found in [65, 66, 67].

### 2.1.3.1 Extinction due to Interstellar Dust

Interstellar dust plays an important role in the extinction of electromagnetic radiation in intra-galactic regions especially in the visible and ultraviolet wavelength range. This section looks at extinction due to the absorption and scattering from interstellar dust particles. The composition of the dust ranges from graphite, amorphous carbon and silicates, to simple molecules such as water and ammonia and to more complex structures such as polycyclic aromatic hydrocarbons (PAHs). The absorption and scattering of FUV radiation which reduces the dissociation rate of  $\text{H}_2$  needs to be accounted for.

The measurement of light reaching a detector is given in units of magnitude, which is defined as a difference of 5 magnitudes is a ratio of 100 in intensity. This can be represented as

$$\frac{I_0}{I} = 100^{(m-m_0)/5}, \quad (2.30)$$

where  $I_0$  is the unattenuated intensity of the source,  $m_0$  is the reference magnitude of the source,

$I$  is the intensity received by the detector,  $m$  is the observed magnitude of the source,  $I_0 > I$ , and  $m > m_0$ , or recast in the form

$$m - m_0 = 2.5 \log\left(\frac{I_0}{I}\right) \quad [\text{mag}]. \quad (2.31)$$

The intensity of the radiation now needs to be determined at some location in a cloud containing dust and the following paragraph is a brief description of how the radiation is attenuated. The specific intensity of electromagnetic radiation as it traverses space will undergo changes in the total intensity as it is absorbed and/or emitted by the medium in question. For emission from the medium, the change in specific intensity increases and its differential is  $dI_\nu = j_\nu ds$  where  $j_\nu$  is the emission coefficient with units of  $\text{erg cm}^{-3} \text{s}^{-1} \text{\AA}^{-1} \text{sr}^{-1}$  and  $s$  is the distance in cm along the ray path. The absorption of the radiation leads to a decrease in the specific intensity which is given by  $dI_\nu = -\kappa_\nu I_\nu ds$  where  $\kappa_\nu$  is the absorption coefficient with units  $\text{cm}^{-1}$ . The net change in the specific intensity after the radiation has traversed the medium and undergone absorption and emission is

$$dI_\nu = j_\nu ds - \kappa_\nu I_\nu ds \quad [\text{erg cm}^{-2} \text{s}^{-1} \text{Hz}^{-1} \text{sr}^{-1}]. \quad (2.32)$$

Dividing equation (2.32) by  $\kappa_\nu ds$ , defining  $S_\nu \equiv j_\nu/\kappa_\nu$  as a term called the source term and which has the same units as the specific intensity, and defining  $d\tau_\nu \equiv \kappa_\nu ds$  where  $\tau_\nu$  is dimensionless and is called the optical depth (or opacity). From this then equation (2.32) becomes what is called the equation of transfer and is given by

$$\frac{dI_\nu}{d\tau_\nu} = S_\nu - I_\nu \quad [\text{erg cm}^{-2} \text{s}^{-1} \text{Hz}^{-1} \text{sr}^{-1}]. \quad (2.33)$$

Assuming that the medium only absorbs and does not emit radiation ( $S_\nu = 0$ ), then equation (2.33) simply becomes

$$\frac{dI_\nu}{d\tau_\nu} = -I_\nu \quad [\text{erg cm}^{-2} \text{s}^{-1} \text{Hz}^{-1} \text{sr}^{-1}]. \quad (2.34)$$

To find then the specific intensity of the radiation at some optical depth into the medium one integrates equation (2.34) from the surface of the cloud, (where the optical depth is zero) to a

specific optical depth as

$$\int_{I'_\nu=I_{\nu,0}}^{I'_\nu=I_{\nu,\tau}} \frac{dI'_\nu}{I'_\nu} = - \int_{\tau'=0}^{\tau'=\tau_\nu} d\tau'_\nu, \quad (2.35)$$

the solution of which finally gives the specific intensity into the cloud as

$$I_{\nu,\tau} = I_{\nu,0} e^{-\tau_\nu} \quad [\text{erg cm}^{-2} \text{ s}^{-1} \text{ Hz}^{-1} \text{ sr}^{-1}]. \quad (2.36)$$

With equation (2.36) then the dust attenuation term in equation (2.28) becomes

$$f_{d,U}(N_H) = e^{-\tau_{d,U}}, \quad (2.37)$$

where

$$\tau_{d,U} \equiv N_H \sigma_{d,U}, \quad (2.38)$$

with  $N_H$  being the total hydrogen column density,  $\sigma_{d,U}$  the effective cross section for dust attenuation by FUV radiation, and  $\tau_{d,U}$  is the optical depth due to interstellar dust grains.

Extinction of light (e.g., electromagnetic radiation from the FUV to the FIR), is commonly measured using the UBV (Ultraviolet, Blue, and Visual) photometric system which measures the color excess, or the amount of reddening of the observed light as shorter wavelength light is preferentially attenuated by dust. This color excess is represented by  $E(B - V)$  which is the difference between observed and intrinsic values of the color index [68]. The extinction at a given wavelength of light increases the apparent magnitude of an observed object. The difference in magnitudes can be related to the extinction in magnitudes,  $A_\lambda$ , as

$$m_\lambda - m_{0,\lambda} \equiv 2.5 \log\left(\frac{I_{0,\lambda}}{I_\lambda}\right) = A_\lambda \quad [\text{mag}]. \quad (2.39)$$

For the extinction at a given wavelength  $A_\lambda$ , a relation can be made with the column density of hydrogen. With the use of equations (2.36) - (2.39) the extinction in magnitudes becomes

$$A_\lambda = 1.086 \sigma_{d,\lambda} N_H \quad [\text{mag}]. \quad (2.40)$$

where  $\sigma_{d,\lambda}$  is the effective attenuation cross section at wavelength  $\lambda$ .

The ratio of the total extinction in the visual band to the color excess in the same band is denoted by  $R_V \equiv A_V/(A_B - A_V) \equiv A_V/E(B - V)$ , with  $B$  being measured at 4405 Å and  $V$  at 5470 Å [65]. The average extinction value is taken to be  $R_V \approx 3.1$ , based on sightlines through the Milky Way galaxy for diffuse gas.

The ratio of the total hydrogen column density to the color excess in these diffuse Milky Way regions was found to be [69]

$$\frac{N_{\text{H}}}{E(B - V)} = 5.8 \times 10^{21} \quad [\text{mag}^{-1} \text{cm}^{-2}]. \quad (2.41)$$

As seen in the previous paragraph,  $1/E(B - V) = R_V/A_V$ , then equation (2.41) becomes,

$$\frac{R_V N_{\text{H}}}{A_V} = 5.8 \times 10^{21} \quad [\text{mag}^{-1} \text{cm}^{-2}], \quad (2.42)$$

or for  $R_V = 3.1$

$$\frac{A_V}{N_{\text{H}}} = 5.35 \times 10^{-22} \quad [\text{mag cm}^2]. \quad (2.43)$$

The extinction of FUV radiation due to dust needs to take into account both the scattering of the radiation off of the dust grains as well as its absorption by the grains. The total extinction for a given wavelength can be given in terms of an effective cross section taking into account the aforementioned scattering and absorption. This can be denoted by

$$\sigma_{\text{ex},\lambda} = \sigma_{\text{sc},\lambda} + \sigma_{\text{ab},\lambda} \quad [\text{cm}^2]. \quad (2.44)$$

The albedo represents the reflectivity of the dust particle and is given as the ratio of the scattering cross section to the total extinction cross section with

$$w_\lambda = \frac{\sigma_{\text{sc},\lambda}}{\sigma_{\text{ex},\lambda}}, \quad (2.45)$$

with  $\sigma_{\text{ex},\lambda}$  being given by equation (2.44). The absorption cross section is then found from equations (2.44) and (2.45) giving

$$\sigma_{\text{ab},\lambda} = (1 - w_\lambda) \sigma_{\text{ex},\lambda} \quad [\text{cm}^2]. \quad (2.46)$$

For the radiation that is scattered from the dust, there is some mean value that the unpolarized light will take, its value depending on the wavelength of the radiation relative to the grain size and the physical nature of the grain (e.g., the optical properties of the dust, such as graphites (metals) or silicates (dielectrics) which determine the optical constants: the refractive and absorption indexes; as well as the geometric structure of the grain (spherical or non-spherical). Taking a random orientation of grains then, unpolarized radiation has only a polar component regarding the preferential scattering direction. This mean value that the scattered radiation takes is the scattering asymmetry factor and is generally denoted by the mean of the cosine of the scattered polar angle as

$$g_\lambda \equiv \langle \cos \theta \rangle_\lambda = \frac{2\pi}{\sigma_{\text{sc},\lambda}} \int_0^\pi \cos \theta \frac{d\sigma_{\text{sc},\lambda}}{d\Omega} \sin \theta d\theta, \quad (2.47)$$

where  $d\sigma_{\text{sc},\lambda}/d\Omega$  is the differential scattering cross section. At an extinction ratio of  $R_V = 3.1$  and an FUV wavelength of  $1000 \text{ \AA}$ , the grain albedo is  $w_{1000} = 0.273$ ,  $g_{1000} = 0.649$  and  $\sigma_{\text{ex,tot},1000} = 2.11 \times 10^{-21} \text{ cm}^2$  [13]. For a total extinction cross section with scattering in only the forward direction, then

$$\sigma_{\text{ex,for},\lambda} = \sigma_{\text{ex,tot},\lambda} (1 + w_\lambda (\langle \cos \theta \rangle_\lambda - 1)) \quad [\text{cm}^2], \quad (2.48)$$

from equations (2.44) - (2.47). With the values given above,  $\sigma_{\text{ex,for},1000} = 1.91 \times 10^{-21} \text{ cm}^2$  which is the same as the rounded values of  $\sigma_{\text{ex,for},1000} = 1.9 \times 10^{-21} \text{ cm}^2$  in [2, 16] and  $\sigma_{\text{ex,for},1000} = 2 \times 10^{-21} \text{ cm}^2$  in [12]. From the `save grain opacity` command in Cloudy 17.01, a range of values for  $\sigma_{\text{ex,for,LW}}$  can be calculated across the Lyman-Werner photon band [70]. These cross sections range from  $\sigma_{\text{ex,for},1110} = 1.60 \times 10^{-21} \text{ cm}^2$  to  $\sigma_{\text{ex,for},912} = 2.02 \times 10^{-21} \text{ cm}^2$  across the LW band with a value of  $\sigma_{\text{ex,for},1000} = 1.87 \times 10^{-21} \text{ cm}^2$  at  $1000 \text{ \AA}$ , where  $g$  ranges from  $g_{1110} = 0.570$  to  $g_{912} = 0.559$  with a value of  $g_{1000} = 0.546$  at  $1000 \text{ \AA}$  and  $\sigma_{\text{ex,for},\lambda} = \sigma_{\text{sc},\lambda} \langle \cos \theta \rangle_\lambda + \sigma_{\text{ab},\lambda}$  was used. The wavelength specific extinction cross section is taken to be  $\sigma_{\text{ex,for},1000} = 1.91 \times 10^{-21} \text{ cm}^2$  as is used in [12, 2, 16] and which is consistent with [70] across the entire LW band.

Based on the values given above, the assumption is made that the metallicity affects the dust to gas ratio in a linear relation so that [2, 16]

$$\sigma_{\text{d},U} = 1.91 \times 10^{-21} Z \quad [\text{cm}^2], \quad (2.49)$$

where  $\sigma_{\text{ex,for,1000}}$  is denoted as  $\sigma_{\text{d},U}$  and  $Z$  is the metallicity relative to solar values,  $Z_{\odot}$ . Normalizing equation (2.49) as a standard Galactic value gives [16]

$$\tilde{\sigma}_{\text{d}} \equiv \frac{\sigma_{\text{d},U}}{1.91 \times 10^{-21} \text{ cm}^2}. \quad (2.50)$$

### 2.1.3.2 Line Profiles

The physical process of photodissociation removes photons that would be capable of photodissociating other additional  $\text{H}_2$  molecules. The removal of these photons is called *self-shielding* and its net effect is to reduce the flux of FUV that would be available for the destruction of  $\text{H}_2$  molecules. This is represented in the second term of equation (2.28),  $f_{\text{s},U}(N_{\text{H}_2})$ , and a brief description of how this process attenuates the FUV radiation field follows in § 2.1.3.3. This section describes some of the underlying physics of line absorption cross sections and equivalent width.

The attenuation of radiation due to absorption by molecular hydrogen has the same form as its attenuation due to dust, i.e. equation (2.36). As radiation is absorbed by a particular rovibrational line, it reduces the flux of radiation at the specific frequency that makes up that transition. This equation is given by

$$I_{\nu} = I_c e^{-\tau_{\nu}} \quad [\text{erg cm}^{-2} \text{ s}^{-1} \text{ Hz}^{-1} \text{ sr}^{-1}], \quad (2.51)$$

where  $I_{\nu}$  is the frequency dependent specific intensity of radiation that is detected,  $I_c$  is the intensity of continuum radiation across all wavelengths received by the detector, and  $\tau_{\nu}$  is the opacity due to absorption of the radiation at the rovibrational transition frequency,  $\nu$ . Equation (2.51) is often given in terms of the line and continuum fluxes that are observed and it becomes  $F_{\nu} = F_c e^{-\tau_{\nu}} \text{ erg cm}^{-2} \text{ s}^{-1}$ . In either the intensity or the flux case, the optical depth,  $\tau_{\nu}$ , varies from the opacity due to dust. Here, it is given by

$$\tau_{\nu} \equiv a_{\nu} N_{\text{H}}, \quad (2.52)$$

or in an expanded form as

$$\tau_{\nu} \equiv a f \phi_{\nu} N_{\text{H}}, \quad (2.53)$$

where as mentioned in equation (2.23),  $a_{\nu} = a f \phi_{\nu} \text{ cm}^2 \text{ s}^{-1} \text{ Hz}^{-1}$  and  $a = \pi e^2 / m_e c \text{ cm}^2 \text{ s}^{-1}$ .

The  $a_\nu$  term is an absorption cross section for a specific rovibrational transition frequency. This cross section represents the line strength of the transition and the three terms that make up the absorption cross section are discussed briefly below.

The oscillator strength,  $f$ , is a dimensionless measure of the intrinsic strength of the transition. Each transition has a different value for the oscillator strength, which can be given in terms of the Einstein induced transition coefficient,  $B$ . For a transition from a lower energy level  $i$ , to a higher energy level  $j$ , the absorption oscillator strength is given by

$$f_{ij} = \frac{\pi e^2}{m_e c} \frac{h\nu_{ij}}{4\pi} B_{ij}, \quad (2.54)$$

where the total atomic absorption coefficient is  $a = \pi e^2/m_e c \text{ cm}^2 \text{ s}^{-1}$ , the energy difference between the levels  $i$  and  $j$  is  $E_j - E_i$  is represented by the photon with the same energy as  $h\nu_{ij}$ , and the Einstein induced absorption coefficient,  $B_{ij} [\text{s g}^{-1}]$ .

The  $\phi_\nu$  term is the line profile function, or also called the line broadening function, and has units of  $\text{Hz}^{-1}$ , or equivalently s. This profile represents the shape of the absorption curve about a given frequency. If one assumes that there is no broadening to the function at all, then the line function would be given by

$$\phi_\nu = \delta(\nu - \nu_{ij}) \quad [\text{Hz}^{-1}], \quad (2.55)$$

such that  $\phi_\nu = 0$  for  $\nu \neq \nu_{ij}$  and  $\int_0^\infty \phi_\nu d\nu = 1$  (normalization). This is an idealization of the profile function and there are effects that cause the line to broaden out so that absorptions away from the natural oscillation frequency of the molecule can occur. The main causes of line broadening that are considered here are natural broadening and doppler broadening.

The theoretical development of line formation was based on a classical model of a driven underdamped harmonic oscillator. The natural frequency of the system is given by the transition frequency and the radiative losses of the electron due to this oscillation is the damping portion of the differential equation that models the motion. This differential equation is

$$m_e \ddot{z} + m_e \gamma \dot{z} + m_e \omega_0^2 z = e E e^{i\omega t} \quad [\text{dyne}], \quad (2.56)$$

where the second term is the damping force, the third term is the restoring force, the fourth term

is the driving force,  $m_e$  is the mass of the electron,  $e$  is the fundamental unit of charge, and  $E$  is the magnitude of the incident electric field. The damping force term represents the radiative loss of energy from the accelerating electron due to its oscillatory motion. Based on classical electromagnetic arguments, the damping constant can be shown to be

$$\gamma = \frac{8\pi}{3} \frac{\pi e^2}{m_e c} \frac{\nu_0^2}{c^2} \quad [\text{Hz}]. \quad (2.57)$$

The restoring force term is the response to the resonance that occurs when a spring is acted upon about its natural frequency. This is an analog of the absorption of radiation by the molecule at the transition frequency, where the angular frequency  $\omega_0 = 2\pi\nu_0$ , is the natural angular frequency of the oscillator. The driving force term is the interaction of the electric field on the charged oscillator. The sinusoidal exponential term contains the angular frequency of the incoming electromagnetic wave,  $\omega$ . Thus this model is representative of an oscillating electric field of angular frequency  $\omega$  interacting with a damped harmonic oscillator of natural angular frequency  $\omega_0$ .

Using classical electromagnetic theory, it can be shown that if a solution of the form  $z = z_0 e^{i\omega t}$  is assumed for equation (2.56), then

$$a \phi_\nu = \left( \frac{\pi e^2}{m_e c} \right) \frac{\gamma/(4\pi^2)}{(\nu - \nu_0)^2 + (\gamma/4\pi)^2} \quad [\text{cm}^2 \text{s}^{-1} \text{Hz}^{-1}], \quad (2.58)$$

where  $\phi_\nu = \frac{\gamma/(4\pi^2)}{(\nu - \nu_0)^2 + (\gamma/4\pi)^2} \text{Hz}^{-1}$ . This function is called a *Lorentzian profile* and has a peak where  $\nu = \nu_0$ , centered about  $\nu_0$ . Since this is a classical treatment, a modification needs to be made so that there is a quantum mechanical analog to equation (2.58). For an electron that is in an excited state, the lifetime before decay occurs is finite, thus there is an uncertainty in the width of the energy levels between states. Heisenberg's uncertainty principle gives this relation as

$$\Delta E \approx \frac{\hbar}{\tau_j} \quad [\text{erg}]. \quad (2.59)$$

where  $\tau_j$  is the lifetime in level  $j$ . Due to this, the classical damping constant is given in terms of

the Einstein spontaneous emission coefficient,  $A_{ji}$ , and,

$$\gamma \rightarrow \Gamma_{ij} \equiv \Gamma_{ji} = \sum_{k<i} A_{ik} + \sum_{k<j} A_{jk} \quad [\text{Hz}]. \quad (2.60)$$

The quantum mechanical modification to natural broadening then modifies the Lorentz profile so that the Lorentz profile of the classical harmonic oscillator is then modified to its quantum mechanical analog as

$$\phi_{\nu, \text{Lor}} = \frac{\Gamma/(4\pi^2)}{(\nu - \nu_0)^2 + (\Gamma/4\pi)^2} \quad [\text{Hz}^{-1}], \quad (2.61)$$

where the normalization condition  $\int_0^\infty \phi_{\nu, \text{Lor}} d\nu = 1$  has been imposed.

Further broadening of the absorption line profile occurs due to the random thermal motion of the molecules as well as the bulk motion of the gas. Generally for most interstellar clouds, thermal motion dominates the broadening features. The broadening of absorption lines is caused by the Doppler shift of the absorption frequency due to line-of-sight motion of the molecules. The frequency shift that occurs due to the Doppler shift is given by the non-relativistic Doppler formula

$$\frac{\nu - \nu_0}{\nu_0} = \frac{v_r}{c}, \quad (2.62)$$

where  $\nu$  is the frequency of absorption in the observers frame of rest frame,  $\nu_0$  is the frequency of absorption in the molecular rest frame,  $v_r$  is the radial velocity of the molecule with respect to the observer, and  $c$  is the speed of light.

Assuming thermal motion only and ignoring the turbulent motion of the cloud, then the most probable speed in the radial direction is

$$b = \sqrt{\frac{2kT}{m}} \quad [\text{cm s}^{-1}], \quad (2.63)$$

where  $k$  is Boltzmann's constant,  $T$  is the kinetic temperature of the gas, and  $m$  is the mass of the molecule. For molecules with a velocity given by equation (2.63), a Maxwellian distribution gives a range of radial velocities between  $v_r$  and  $v_r + dv_r$  as

$$f_{v_r} dv_r = \frac{1}{\sqrt{\pi}} \frac{e^{-(v_r^2/b^2)}}{b} dv_r. \quad (2.64)$$

If turbulent motion of the gas is considered, then this contributes an additional velocity component to the Doppler parameter. The Doppler parameter, equation (2.63) is modified to

$$u = \sqrt{u_{\text{th}}^2 + u_{\text{tu}}^2} \quad [\text{cm s}^{-1}], \quad (2.65)$$

where  $u_{\text{th}}$  is the thermal velocity given by equation (2.63) and  $u_{\text{tu}}$  is the turbulent velocity of the gas. For a Gaussian curve, which describes the Doppler parameter, then  $b \equiv \sqrt{2}\sigma$  where  $\sigma$  is the standard deviation. A quantity called the Doppler width can be defined such that  $\Delta\nu_D = \nu_0 (b/c) \text{ s}^{-1}$ , from which it can be shown that  $v_r/b = \Delta\nu/\Delta\nu_D$ . Then with consideration that a fraction of the intensity that is absorbed over a narrow strip  $d\nu$  vs.  $d\nu_D$  over all of the absorption lines, gives a Gaussian, or *Doppler profile*:

$$\phi_{\nu, \text{Dop}} = \frac{1}{\sqrt{\pi}} \frac{e^{-(\Delta\nu^2/\Delta\nu_D^2)}}{\Delta\nu_D} \quad [\text{Hz}^{-1}], \quad (2.66)$$

where the normalization condition  $\int_{\Delta\nu=-\infty}^{\Delta\nu+\infty} \phi_{\nu, \text{Dop}} d\nu = 1$  has been imposed.

Since there are two line profile functions, given by  $\phi_{\nu, \text{Lor}}$  and  $\phi_{\nu, \text{Dop}}$ , the natural (damping) broadening function (Lorentzian), and the Doppler broadening function (Gaussian) respectively, they need to be combined to get a single profile function. This is a convolution of the two aforementioned functions, which is called Voigt function. Performing this convolution, gives the absorption profile cross section

$$a_{\nu, \text{Voi}} = \left( \frac{af}{\sqrt{\pi}\Delta\nu_D} \right) \left( \frac{w}{\pi} \right) \int_{-\infty}^{+\infty} \frac{e^{-y^2}}{(u-y)^2 + w^2} dy \quad [\text{cm}^2], \quad (2.67)$$

where  $u \equiv (\nu - \nu_0)/\Delta\nu_D$ ,  $w \equiv \Gamma/(4\pi\Delta\nu_D)$ , and  $y \equiv \Delta\nu/\Delta\nu_D$ . The convolution of the Lorentz and Doppler profiles is given by

$$H(w, u) = \left( \frac{w}{\pi} \right) \int_{-\infty}^{+\infty} \frac{e^{-y^2}}{(u-y)^2 + w^2} dy \quad (2.68)$$

where  $H(w, u)$  is the *Voigt profile*.

The Voigt profile is dominated about the line center,  $\nu \simeq \nu_0$ , by the Doppler portion of the convolution function, and is known as the Doppler core. As larger frequency shifts are considered

away from the line center, the Gaussian (Doppler) portion dies off faster than the Lorentzian (natural) component and the absorptions become more significant in the line wings.

The total strength of a given absorption line is given by the amount of flux that is removed about the center of the line versus the flux from the radiation field. In practice the shape of the line profile may not be resolvable but the amount of absorbed flux can be determined. The frequency equivalent width is a method for converting the amount of absorbed flux from a line profile shape to a rectangle with the same area. Mathematically this is given by

$$W_\nu \equiv \int_0^\infty \left(1 - \frac{F_\nu}{F_c}\right) d\nu \quad [\text{Hz}], \quad (2.69)$$

where  $F_\nu$  is the flux at the line frequency  $\nu$ ,  $F_c$  is the flux of the continuum. The integrand is called the line depth and is defined as  $A_\nu \equiv 1 - F_\nu/F_c$ . The continuum flux can be considered as a constant about the narrow frequency range of a line. Equation (2.69) is also given in wavelength equivalent widths, velocity equivalent widths and as normalized equivalent widths. From equations (2.51), (2.53), and (2.69) the equivalent width can be given in terms of the optical depth as

$$W_\nu = \int_0^\infty (1 - e^{-\tau_\nu}) d\nu \quad [\text{Hz}]. \quad (2.70)$$

For the optically thin case,  $\tau_\nu < 1$ , the equivalent width can be approximated by

$$W_\nu \approx \left(\frac{\pi e^2}{m_e c}\right) \frac{f_{ij} N_i}{\nu} \quad [\text{Hz}], \quad (2.71)$$

where  $f_{ij}$  is the oscillator strength between levels  $i$  and  $j$  corresponding to the absorption frequency  $\nu$ . Denoting the optical depth at line-center as

$$\tau_0 \simeq \frac{a}{\sqrt{\pi}} \frac{f_{ij} N_i}{b\nu}, \quad (2.72)$$

where  $a = \pi e^2/m_e c$ . Equation (2.71) can then be written to first order as  $W_\nu \approx \sqrt{\pi} (b/c) \tau_0$ . From equation (2.71) it can be seen that the equivalent width is directly proportional to the column density as  $W_\nu \propto N_i$ . This is called the *linear portion* of the curve of growth. As the column density increases, the absorption of photons at the line center becomes saturated and Doppler broadening

becomes the dominant part of the line profile. The equivalent width in this optically thick ( $\tau_0 \gtrsim 10$ ) region is approximated as

$$W_\nu \approx \frac{2b}{c} \sqrt{\ln(\tau_0/\ln 2)} \quad [\text{Hz}]. \quad (2.73)$$

This is called the *saturated* (or *flat*) *portion* of the curve of growth as it is proportional to  $\sqrt{\ln N_i}$ . As  $\tau_0$  increases further, the Doppler core is completely saturated and the "damping wings" of the Lorentz profile are the only optically thin regions. In this region it is assumed that only the Lorentz profile determines the line profile and then the equivalent width becomes

$$W_\nu = \sqrt{\frac{b}{c} \frac{\tau_0}{\sqrt{\pi}} \frac{\Gamma_{ij}}{\nu}} \quad [\text{Hz}]. \quad (2.74)$$

This is called the *damped* (or *square-root*) *portion* of the curve of growth as the equivalent width is proportional to  $\sqrt{N_i}$ .

### 2.1.3.3 Self-Shielding of Molecular Hydrogen

The effects of the processes discussed in § 2.1.2 and 2.1.3.2 diminishes the FUV radiation field needed to dissociate  $\text{H}_2$ , as the radiation is absorbed in the transition lines. This decreases the radiation that is available to photoexcite  $\text{H}_2$  into the Lyman-Werner bands necessary for photodissociation. Since the line absorption strength is a determinant of the equivalent width for that line, then the relative attenuation that occurs (relative to there being no attenuation) as the FUV radiation traverses the cloud is proportional to the derivative of the equivalent width with respect to the attenuating column density. This can be written as [9, 10]

$$f_s(N_{\text{H}_2}, \nu) = \left( \frac{\pi e^2}{m_e c} f_{ij} \right)^{-1} \frac{dW_{\nu,ij}}{dN_{\text{H}_2,i}}, \quad (2.75)$$

where  $W_{\nu,ij}$  is the frequency dependent equivalent width given by equation (2.69) and  $N_{\text{H}_2,i}$  is the column density of molecular hydrogen in the initial rovibrational level  $i$ . From equation (2.69) it can be seen that

$$f_s(N_{\text{H}_2}, \nu) < 1 \quad (2.76)$$

At low column densities the line absorption is optically thin and if there is assumed to be no coincidental overlap between absorption lines then equation (2.75) is a good approximation to self-shielding [12]. As column densities increase and absorptions start to occur out in the Lorentzian damping wings, overlap between nearby lines may occur and the self-shielding function needs to be modified from the form of equation (2.75). A more accurate equation for the self-shielding function is given by [12]

$$f_{s,U}(N_{\text{H}_2}) = \frac{0.965}{(1 + x/b_5)^2} + \frac{0.035}{(1 + x)^{0.5}} e^{(-8.5 \times 10^{-4}(1+x)^{0.5})}, \quad (2.77)$$

where  $x \equiv N_{\text{H}_2}/(5 \times 10^{14} \text{ cm}^{-2})$  and  $b_5 \equiv b/(10^5 \text{ cm s}^{-1})$  where  $b$  is the Doppler parameter, equation (2.65).

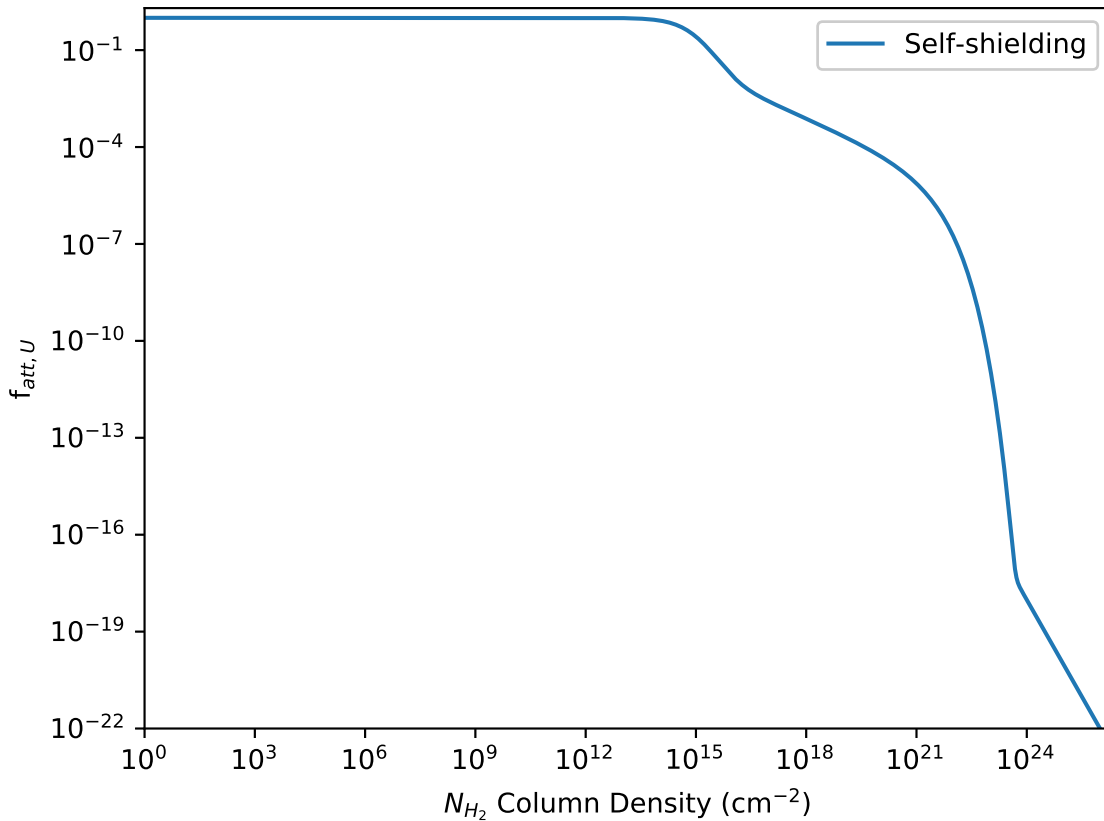


Figure 2.1: The self-shielding function given by equation (2.77)

## 2.1.4 Molecular Hydrogen Formation

The formation of molecular hydrogen occurs through two main pathways. The first discussed here is the formation of  $\text{H}_2$  through mechanisms in the gas-phase chemistry. The second is its formation on dust grains, a process known as grain-catalyzed  $\text{H}_2$  formation.

### 2.1.4.1 Formation in the Gas Phase

As was discussed in § 2.1.2, the direct formation of  $\text{H}_2$  via radiative association



has an extremely slow reaction rate ( $\lesssim 10^{-23} \text{ cm}^3 \text{ s}^{-1}$ ) due to the forbidden transition by the  $\Delta S = 0$  selection rule [14, 39]. The three-body reaction



with the H atom carrying away the energy of formation as kinetic energy is another possible mechanism to create  $\text{H}_2$  however this mechanism has a negligible rate to occur in typical molecular cloud densities. Another mechanism is the two step reaction involving the  $\text{H}^+$  ion (proton). The first is by radiative association



followed by charge transfer



however the former reaction has a rate coefficient of  $k \approx 7 \times 10^{-20} \text{ cm}^3 \text{ s}^{-1}$  and so is also an insignificant route of  $\text{H}_2$  formation [71, 72].

In gas-phase chemistry with low metallicity, the dominant pathway to the creation of  $\text{H}_2$  is by the two step reaction involving the  $\text{H}^-$  ion. The first is by radiative attachment



followed by associative detachment



The rate of formation of  $\text{H}_2$  via this channel in a low ionization environment can be given by [73]

$$R_{\text{H}^- \rightarrow \text{H}_2} = 8 \times 10^{-19} x_{e,-3} T_3^{0.88} \quad [\text{cm}^3 \text{s}^{-1}], \quad (2.82)$$

where  $x_e \equiv n_e/(10^{-3} n_{\text{H}})$  is the normalized ionization fraction and  $T_3 \equiv T/(1000 \text{ K})$ . In clouds with a temperature of  $T \sim 100 \text{ K}$  this gives a formation rate constant  $R_{\text{H}^- \rightarrow \text{H}_2} \sim 10^{-19} \text{ cm}^3 \text{ s}^{-1}$ .

#### 2.1.4.2 Formation on Dust Grains

For the formation of molecular hydrogen to occur at faster rates, a different mechanism than gas-phase chemistry is needed. The idea of forming  $\text{H}_2$  on the surface of dust grains was put forward as an alternative mechanism [14, 74]. Further elaboration on the rates of grain-catalyzed  $\text{H}_2$  formation, including theoretical, numerical, and experimental methods has been discussed by various authors, some of which include [15, 34, 75, 76, 77, 78, 79, 80, 81, 82, 83] with a summary of these topics given in [84].

Formation of  $\text{H}_2$  on the surface of dust grains occurs when an  $\text{H}^0$  atom strikes the surface of a dust grain and sticks to its surface. A second hydrogen atom then approaches the *adsorbed*  $\text{H}^0$  atom and in doing so forms an  $\text{H}_2$  molecule which leaves the surface of the dust grain. There are two types of mechanisms that allow dust grain surfaces to be used as heterogenous catalysts in the formation of hydrogen molecules from  $\text{H}^0$  atoms. In this way it may be considered as a three-body reaction:



The first way that  $\text{H}_2$  can be formed on dust grain surfaces is called the Langmuir-Hinshelwood (LH) mechanism. In this process an  $\text{H}^0$  atom is *physisorbed* on the surface of the dust grain and is loosely bound to its surface by electrostatic attraction (e.g., Van de Waals forces). The bound  $\text{H}^0$  atom is considered to be able to migrate by a random walk across the surface of the dust grain. If another hydrogen atom leaves the gas phase and also becomes adsorbed to the surface of the dust

grain, it too can migrate about the surface of the dust grain and if it comes close enough to the first physisorbed  $\text{H}^0$  atom, they may form a molecule of  $\text{H}_2$  and leave the surface of the dust grain. The formation of  $\text{H}_2$  by this mechanism is allowed versus the gas-phase formation mechanism because the excess energy of formation, up to its ground state binding energy of 4.478 eV, can be given to the dust grain lattice as thermal energy. The ejection of  $\text{H}_2$  from the dust grain surface often leaves it an excited state which will then re-radiate in an infrared cascade.

The second way that molecular hydrogen is formed on the surface of dust grains is the Eley-Rideal (ER) mechanism. In this mechanism, an  $\text{H}^0$  atom is *chemisorbed* from the gas phase into sites on the dust grain surface. This binds the hydrogen atom into a lower potential well than being physisorbed. Because of the deeper potential well in chemisorption, the grain can be of higher temperatures than those in the LH case, however this limits the ability of the chemisorbed hydrogen atom to move about the surface and it needs to quantum mechanically tunnel between neighboring potential wells. Formation of  $\text{H}_2$  occurs in this case by the reaction of a chemisorbed  $\text{H}^0$  atom with a gas-phase hydrogen atom where energy is lost to overcoming the potential barrier of the well, the excitation (heating) of the dust grain lattice, rovibrational excitation of the  $\text{H}_2$  molecule, and the kinetic energy of the hydrogen molecule.

In either formation mechanism, the idea is that  $\text{H}^0$  atoms become either physisorbed or chemisorbed on the dust grain surface and will form  $\text{H}_2$  before they are desorbed from the dust grain surface by thermal excitation from the dust grain, or by an external radiation field. The energy of formation is given up as heat to the dust grain, excitation of the  $\text{H}_2$  rovibrational levels, and to the external kinetic energy of the molecule.

The formation rate of  $\text{H}_2$  on the surface of dust grains is dependent on a number of factors. These include the nature of the material that makes up the dust grain, the probability that an initial  $\text{H}^0$  atom sticks to the surface of the dust grain, the probability that an adsorbed  $\text{H}^0$  encounters another  $\text{H}^0$  atom, the thermal speed of the hydrogen atoms in the gas-phase, the temperature of the dust grain, the number density of dust grains, the number density of  $\text{H}^0$  atoms, and the effective cross section of the dust grain. The  $\text{H}_2$  formation rate on dust grains can then be given as

$$\frac{dn_{\text{H}_2,\text{d}}}{dt} = \frac{1}{2} S(T, T_d) \eta \langle \sigma_d \rangle \langle v_{\text{H}^0} \rangle n_{\text{H}^0} n_{\text{H}} \quad [\text{cm}^{-3} \text{s}^{-1}], \quad (2.84)$$

where the factor  $1/2$  represents the fact that two  $\text{H}^0$  atoms are required for the formation of one hydrogen molecule,  $S(T, T_d)$  is the sticking factor, which represents the probability for a hydrogen atom of temperature  $T$  to be adsorbed on the surface of the dust grain with temperature  $T_d$ ,  $\eta$  is the probability that an adsorbed  $\text{H}^0$  atom will interact with another  $\text{H}^0$  atom and form a molecule of hydrogen,  $\langle\sigma_d\rangle$  is the mean effective surface area of the grains in units of  $\text{cm}^2$ ,  $n_{\text{H}^0}$  is the number density of  $\text{H}^0$  atoms in the gas phase and  $\langle v_{\text{H}^0}\rangle$  is the mean thermal velocity of gas phase  $\text{H}^0$  atoms. The sticking factor will be denoted by  $S(T, T_d) \rightarrow S$  where the gas-phase temperature and the dust grain temperature is implicit. Based on a Maxwell-Boltzmann distribution the mean thermal velocity of the gas-phase  $\text{H}^0$  is

$$\langle v_{\text{H}^0}\rangle = \left( \frac{8kT}{\pi m_{\text{H}^0}} \right)^{1/2} \quad [\text{cm s}^{-1}], \quad (2.85)$$

where  $m_{\text{H}^0}$  is the atomic mass of  $\text{H}^0$ .

In order for  $\text{H}_2$  to form on the surface of dust grains,  $\text{H}^0$  atoms must be able to be adsorbed and bind with another hydrogen atom to create a molecule of hydrogen before they are ejected from the dust grain surface. This means that the rate of adsorption exceeds the rate of desorption on the dust grain surface as

$$S\langle\sigma_d\rangle\langle v_{\text{H}^0}\rangle n_{\text{H}^0} > \nu_0 e^{-q_{\text{ads}}/kT}, \quad (2.86)$$

where  $\langle\sigma_d\rangle$  is the effective average surface area per grain,  $\nu_0$  is the frequency of surface vibration of an adsorbed atom and  $q_{\text{ads}}$  is the adsorption binding energy. From this then there is a critical dust grain temperature below which  $\text{H}_2$  formation can take place as its formation rate is greater than the thermal desorption of the  $\text{H}^0$  atoms. The maximum critical dust grain temperature is thus [75, 79]

$$T_{\text{d,c}} < \frac{q_{\text{ads}}}{k} \left[ \ln \left( \frac{\nu_0}{S\langle\sigma_d\rangle\langle v_{\text{H}^0}\rangle n_{\text{H}^0}} \right) \right]^{-1} \quad [\text{K}]. \quad (2.87)$$

This shows that the greater the adsorption binding energy  $q_{\text{ads}}$ , the greater temperature that a dust grain can have. The Eley-Rideal mechanism which involves the chemisorption of  $\text{H}^0$  atoms is favored over the physisorption involved in the Langmuir-Hinshelwood mechanism.

The grain-catalyzed rate of formation molecular hydrogen can be cast into a simplified form by

combining the terms

$$S \eta \equiv \epsilon, \quad (2.88)$$

which represents the formation efficiency of molecular hydrogen. The mean surface area of the grains can be given as

$$\langle \sigma_d \rangle \equiv \int \frac{dn_d}{da} \pi a^2 da \quad [\text{cm}^2]. \quad (2.89)$$

Combining equations (2.85), (2.88) and (2.89) into equation (2.84) gives

$$\frac{dn_{\text{H}_2, \text{d}}}{dt} = R_d n_{\text{H}^0} n_{\text{H}} \quad [\text{cm}^{-3} \text{s}^{-1}], \quad (2.90)$$

where the formation rate coefficient is given numerically as

$$R_d \equiv 7.3 \times 10^{-18} T^{1/2} \epsilon \quad [\text{cm}^3 \text{s}^{-1}]. \quad (2.91)$$

At a gas-phase temperature of  $T \approx 70$  K and assuming an  $\epsilon \approx 0.5$  gives [85]

$$R_d = 3 \times 10^{-17} \quad [\text{cm}^3 \text{s}^{-1}]. \quad (2.92)$$

If it is taken that the formation rate coefficient is dependent on the square root of the gas temperature and that the formation efficiency scales with the dust grain cross section, then the  $\text{H}_2$  formation rate on dust grain surfaces can be recast as [2, 16]

$$R_d = 3 \times 10^{-18} T^{1/2} \tilde{\sigma}_d \quad [\text{cm}^3 \text{s}^{-1}], \quad (2.93)$$

where  $\tilde{\sigma}_d$  is normalized dust grain cross section, equation (2.49). If a fixed gas temperature of  $T = 100$  K is assumed, then equation (2.93) can be given as

$$R_d = 3 \times 10^{-17} \tilde{\sigma}_d \quad [\text{cm}^3 \text{s}^{-1}], \quad (2.94)$$

so that only the normalized dust grain cross-section  $\tilde{\sigma}_d$ , enters as a parameter.

## 2.2 Steady State FUV Field Creation - Destruction of Molecular Hydrogen

Starting with equation (2.1) which can be rearranged to give

$$\frac{n_{\text{H}^0}}{n_{\text{H}_2}} = \frac{1}{2} \frac{D_U}{R_d n_{\text{H}}} f_{\text{att},U}, \quad (2.95)$$

which is the dimensionless ratio of the atomic hydrogen to molecular hydrogen number densities given in terms of the attenuated  $\text{H}_2$  FUV dissociation rate to the  $\text{H}_2$  formation rate. The coefficient  $1/2$  is inserted to account for the decrease in surface flux of the free space FUV radiation field when an optically thick gas slab is inserted and the incident FUV radiation field is considered to be beamed. This discussion on the relation of flux in beamed and isotropic fields is given in § 2.1.1. The free space dissociation rate,  $D_U$ , is the product of the the mean weighted photon flux in the LW-band (912 - 1108 Å) and the total  $\text{H}_2$  dissociation cross section and has a value of  $D_U = 5.81 \times 10^{-11} \text{ s}^{-1}$  in a unit Draine FUV spectrum [2],  $R_d$  is the molecular hydrogen formation rate coefficient on dust grain surfaces and is given in equation (2.93). The attenuation term,  $f_{\text{att},U}$  accounts for a decrease in the free space dissociation rate due to the self-shielding of molecular hydrogen and the extinction of LW-band photons on dust grains given by equation (2.28).

The free space dissociation rate given above will be used so that,  $D_U = 5.81 \times 10^{-11} \text{ s}^{-1}$  for a unit Draine LW-band FUV-field, which can then be given as the product of an integrated photon flux over the LW-band given in Table A.4 and an effective dissociation cross-section per photon

$$D_U = Q_{\text{LW}} \sigma_{U,Q} \quad [\text{s}^{-1}]. \quad (2.96)$$

This dissociation rate is scaled to the unit free space FUV radiation field in the LW-band, given as  $I_U = 1$ , so that

$$D_U = 5.81 \times 10^{-11} I_U \quad [\text{s}^{-1}]. \quad (2.97)$$

From equation (2.96), an effective dissociation cross section per photon in the LW band can be given by

$$\sigma_{U,Q} = 2.81 \times 10^{-18} \quad [\text{cm}^2 \text{ photon}^{-1}], \quad (2.98)$$

where a photon flux of  $Q_{\text{LW}} = 2.07 \times 10^7 \text{ photon cm}^{-2} \text{ s}^{-1}$  was used. This effective cross-section takes into account that only a fraction of the absorbed LW band radiation leads to a dissociation, a mean value of which can be taken to be  $\langle f_d \rangle = 0.12$  [2]. Thus the effective cross section for absorption is approximately an order of a magnitude greater than that shown in equation (2.98).

The dimensionless ratio of the unattenuated  $\text{H}_2$  FUV dissociation rate to the  $\text{H}_2$  formation rate is defined as  $\alpha$  where [11]

$$\alpha \equiv \frac{D_U}{R_d n_{\text{H}}}. \quad (2.99)$$

In terms of the photon flux and the total cross section over the LW band this is then

$$\frac{D_U}{R_d n_{\text{H}}} = \frac{Q_{\text{LW}} \sigma_{U,Q}}{R_d n_{\text{H}}}. \quad (2.100)$$

Substituting in equations (2.93) and (2.97), and using a fixed gas temperature of  $T = 100 \text{ K}$  give [16]

$$\alpha = 1.94 \times 10^6 \frac{I_U}{\tilde{\sigma}_d n_{\text{H}}}. \quad (2.101)$$

where  $\tilde{\sigma}_d$  comes from  $R_d = 3 \times 10^{-17} \tilde{\sigma}_d \text{ cm}^3 \text{ s}^{-1}$  at  $T = 100 \text{ K}$  and is given by equation (2.50). In this form  $\alpha$  is dependent on the ratio of the scaled Draine FUV spectrum to the total hydrogen number density and the normalized galactic dust cross section. As a comparison,  $\alpha$  can also be written in terms of the FUV flux over the LW band. Since  $I_U$  is the unit Draine field and from equation (A.44) and Table (A.4), then  $I_U = (F_{\text{LW}}/3.99 \times 10^{-4}) \text{ erg cm}^{-2} \text{ s}^{-1}$  and,

$$\alpha = 4.85 \times 10^9 \frac{F_{\text{LW}}}{\tilde{\sigma}_d n_{\text{H}}}. \quad (2.102)$$

In this case the free space dissociation rate was given in terms of the FUV energy flux over the LW band as

$$D_U = 1.46 \times 10^{-7} F_{\text{LW}} \text{ [s}^{-1}\text{]}. \quad (2.103)$$

The dimensionless FUV attenuation function  $A$  is defined as

$$A \equiv f_{s,U}(N_{\text{H}}) f_{d,U}(N_{\text{H}_2}) = \left( \frac{0.965}{(1+x/b_5)^2} + \frac{0.035}{(1+x)^{0.5}} e^{(-8.5 \times 10^{-4}(1+x)^{0.5})} \right) e^{-\tau_{d,U}}, \quad (2.104)$$

where the terms  $x$  and  $b_5$  were defined below equation (2.77) and  $\tau_{d,U}$  is given by equation (2.38). This represents the attenuation of the FUV radiation field due to self-shielding of  $\text{H}_2$ , and the extinction of the radiation on dust grains. Again the notation is adopted from [2]. The value of  $A$  is dependent on both the molecular hydrogen column density and the total hydrogen column density, with the self-shielding term being dependent on  $N_{\text{H}_2}$  and the dust absorption term being dependent on  $N_{\text{H}}$ , and is implicitly dependent on the normalized dust grain cross section  $\tilde{\sigma}_d$  in the  $\tau_{d,U}$  term.

Combining equations (2.99) and (2.104) leads to

$$\alpha A \equiv \frac{D_U f_{s,U}(N_{\text{H}}) f_{d,U}(N_{\text{H}_2})}{R_d n_{\text{H}}} = \frac{Q_{\text{LW}} \sigma_U f_{s,U}(N_{\text{H}}) f_{d,U}(N_{\text{H}_2})}{R_d n_{\text{H}}}. \quad (2.105)$$

Thus,  $\alpha A$  represents the ratio of the attenuated (due to *self-shielding* and *extinction*)  $\text{H}_2$  dissociation rate per hydrogen nucleus and the free space  $\text{H}_2$  formation rate.

Using equations (2.38), (2.101), and (2.104) casts  $\alpha A$  into the form

$$\alpha A = 1.94 \times 10^6 \frac{I_U}{n_{\text{H}} \tilde{\sigma}_d} \left( \frac{0.965}{(1+x/b_5)^2} + \frac{0.035}{(1+x)^{0.5}} e^{(-8.5 \times 10^{-4}(1+x)^{0.5})} \right) e^{-\tau_{d,U}}, \quad (2.106)$$

as in § 2.1.3.3, where  $x \equiv N_{\text{H}_2}/(5 \times 10^{14} \text{ cm}^{-2})$  and  $b_5 \equiv b/(10^5 \text{ cm s}^{-1})$ . In this form it can be seen that  $\alpha A$  is dependent on the ratio of the multiple of a normalized free-space Draine FUV radiation field per hydrogen nucleus  $I_U/n_{\text{H}}$ , to the normalized dust grain cross section  $\tilde{\sigma}_d$ , attenuated by terms dependent on the molecular hydrogen and total hydrogen column densities,  $N_{\text{H}_2}$  and  $N_{\text{H}}$  respectively, as well as a normalized dust grain cross section  $\tilde{\sigma}_d$  implicit in the optical depth term  $\tau_{d,U}$ . In terms of the FUV LW-band flux, equation (2.106) is given by

$$\alpha A = 4.85 \times 10^9 \frac{F_{\text{LW}}}{n_{\text{H}} \tilde{\sigma}_d} \left( \frac{0.965}{(1+x/b_5)^2} + \frac{0.035}{(1+x)^{0.5}} e^{(-8.5 \times 10^{-4}(1+x)^{0.5})} \right) e^{-\tau_{d,U}}. \quad (2.107)$$

The ratio of atomic-to-molecular hydrogen for an attenuated FUV radiation field can then be given as

$$\frac{n_{\text{H}^0}}{n_{\text{H}_2}} = \frac{1}{2} \alpha A. \quad (2.108)$$

The modeling of these density profiles is done in §4.2.

The attenuation function  $A$  is a complicated function of the total hydrogen column density  $N_{\text{H}}$ . An analytic fit to this attenuation function that is parameterized by the normalized grain cross section is given by [16]

$$G = 3.0 \times 10^{-5} \tilde{\sigma}_{\text{d}} \left( \frac{9.9}{1 + 8.9 \tilde{\sigma}_{\text{d}}} \right)^{0.37}, \quad (2.109)$$

and is fixed for a given  $\tilde{\sigma}_{\text{d}}$ . Combining equations (2.101) and (2.109) gives an analytic approximation to the shielded atomic-to-molecular hydrogen density ratio  $n_{\text{H}^0}/n_{\text{H}_2}$  as [16]

$$\alpha G = 59 \left( \frac{I_{\text{U}}}{n_{\text{H}}} \right) \left( \frac{9.9}{1 + 8.9 \tilde{\sigma}_{\text{d}}} \right)^{0.37}, \quad (2.110)$$

and in terms of the LW-band flux this then becomes

$$\alpha G = 1.5 \times 10^5 \left( \frac{F_{\text{LW}}}{n_{\text{H}}} \right) \left( \frac{9.9}{1 + 8.9 \tilde{\sigma}_{\text{d}}} \right)^{0.37}. \quad (2.111)$$

The model used in this dissertation calculates  $A$  instead of the parameterized form  $G$ . The  $\alpha G$  term will be used in order to pick an  $\alpha$  for input into the model. From this then  $F_{\text{LW}}/n_{\text{H}}$  can be determined. Comparisons between these models is given in §4.2.

# Chapter 3

## XDR - Model

### 3.1 Physical Processes

The basic equation for the creation-destruction of  $\text{H}_2$  in steady state, isothermal, non-turbulent conditions with a low ionization fraction ( $x_e \lesssim 10^{-3}$ ) for a beamed hard X-ray spectrum radiation field into an optically thick plane parallel slab is given by

$$R_d n(\text{H}^0) n(\text{H}) = \frac{1}{2} D_X f_{\text{att},X} n(\text{H}_2) \quad [\text{cm}^{-3} \text{s}^{-1}]. \quad (3.1)$$

Similar to equation (2.1), the left side of equation (3.1) represents the formation rate per unit volume of  $\text{H}_2$   $\text{cm}^{-3} \text{s}^{-1}$ , and conversely, the right hand side is the destruction rate per unit volume of  $\text{H}_2$  with the same units. The volumetric formation rate of  $\text{H}_2$  is dependent upon the formation rate coefficient  $R_d$   $\text{cm}^3 \text{s}^{-1}$ , the atomic hydrogen number density  $n(\text{H}^0)$   $\text{cm}^{-3}$ , and the total hydrogen nuclei number density  $n(\text{H})$   $\text{cm}^{-3}$ . The factor of  $1/2$  comes from the reduction in the surface flux density of a total free-space radiation field when an optically thick semi-infinite slab is inserted and the impinging field is considered to be beamed. The volumetric destruction rate of  $\text{H}_2$  due to a hard X-ray radiation field (HXR) depends on the free space destruction rate  $D_X$   $\text{s}^{-1}$ , the dimensionless depth dependent attenuation of the radiation field  $f_{\text{att},X}$ , and the molecular hydrogen number density  $n(\text{H}_2)$   $\text{cm}^{-3}$ . The number densities  $n(\text{H}^0)$ ,  $n(\text{H}_2)$ , and  $n(\text{H})$  shall be denoted by  $n_{\text{H}^0}$ ,  $n_{\text{H}_2}$ , and  $n_{\text{H}}$  respectively. The total hydrogen nuclei number density is conserved so that  $n_{\text{H}} \equiv n_{\text{H}^0} + 2n_{\text{H}_2}$ .

### 3.1.1 Hard X-Ray Radiation Field

The radiation field due to hard X-rays (HXR) can come from a variety of sources that exist in astrophysical environments. These X-rays are generally classified by a spectrum that has an energy of greater than 1 keV. Sources of these X-rays range from accretion onto compact objects, supernova shocks, radiation surrounding T Tauri stars and active galactic nuclei.

The energy deposition to the cloud is determined by the amount of radiation transferred into kinetic energy of matter. This energy deposition rate is then given by

$$H_X = \int_{E_{\min}}^{E_{\max}} \sigma_{\text{pa}}(E) F(E) dE \quad [\text{erg s}^{-1}]. \quad (3.2)$$

Ignoring the rate of primary photoionizations compared to the rate of secondary ionizations due to the primary photoelectron, the total hydrogen ionization rate is then

$$\zeta_X \simeq N_{\text{sec}}(x_e) H_X \quad [\text{s}^{-1}]. \quad (3.3)$$

A detailed analysis of the spectrum of a hard X-ray field was provided by Maloney et al. [3]. This section is an outline of the derivation they used in determining the energy deposition rate, and hence the ionization rate of atomic and molecular hydrogen due to the aforementioned spectrum. It will also be the spectrum that is used for the perturbation in this dissertation. We denote the number of secondary ionizations produced with a regular text capital  $N$  to demarcate it from the italicized  $N$  used to denote column density.

A flux of high energy X-ray photons that enter a molecular cloud are attenuated through the preferential photoionization of the lowest energy photons in the spectrum. This is due to the cross-section for both photoelectric and Compton scattering to have an inverse dependence on the energy of the incident X-ray. For X-rays with an energy of  $E \lesssim 4$  keV the interactions are dominated by the photoelectric effect. As the energy of the X-ray increases into the  $4 \text{ keV} \lesssim E \lesssim 10 \text{ keV}$  Compton scattering becomes more predominant and dominates when  $E \gtrsim 10 \text{ keV}$  [86]. At an X-ray energy of greater than 1.02 MeV, pair production is capable of occurring but is not of a concern in this analysis. The SED is structured so that X-rays of an energy less than 1 keV are attenuated through a column density of  $N_{\text{H}} \approx 10^{22} \text{ cm}^{-2}$ . For the purposes of the perturbation model used in this

dissertation, the spectrum is considered to be only in the 1 - 100 keV range and that no attenuation of photons of less than 1 keV need occur.

The spectral energy distribution shape is assumed to be a power-law so that the spectral energy distribution is given by

$$F_X(E) = F_{0X} \left( \frac{E}{1 \text{ keV}} \right)^{-\alpha_X} \quad [\text{erg cm}^{-2} \text{ s}^{-1} \text{ keV}^{-1}], \quad (3.4)$$

where  $F_X$  is the incident X-ray flux into a cloud,  $F_{0,X}$  is the initial X-ray flux at 1 keV, and  $\alpha_X$  determines the spectral index. In this case the spectral index will be chosen to be  $\alpha_X = 0.7$  [87].

The X-ray flux incident on the cloud then is attenuated through an optical depth such that

$$F(E) = F_X(E) e^{-\tau_X(E)} \quad [\text{erg cm}^{-2} \text{ s}^{-1} \text{ keV}^{-1}], \quad (3.5)$$

where  $\tau_X(E) = \sigma_X(E) N_{\text{H}}$  is the energy dependent optical depth,  $\sigma_X(E)$  is the relevant cross section at solar metallicity for a photoionizing photon of energy  $E$  traversing an attenuating hydrogen column  $N_{\text{H}}$ , and  $F(E)$  represents the local X-ray flux per keV.

A beamed field of normally incident X-ray photons is assumed where the total photoionization rate of hydrogen is given by

$$\zeta_X = \int_{E_{\text{min}}}^{E_{\text{max}}} \frac{F(E)}{E} [\sigma_{\text{H}}(E) + \sigma_{\text{pa}}(E)(E - E_{\text{th}})N_{\text{sec}}(E, x_e)] dE \quad [\text{s}^{-1}], \quad (3.6)$$

This represents the ionization rate due to both primary and secondary ionizations. Here  $\sigma_{\text{H}}(E)$  is the photoionization cross section of hydrogen and  $\sigma_{\text{pa}}(E)$  is the X-ray photoelectric cross section due to all elements per hydrogen nucleus.  $E - E_{\text{th}}$  energy difference between the incoming X-ray and the threshold energy of the ionization potential for a cross section at energy  $E$ . The number of secondary ionizations per unit energy of hydrogen that are produced by a photoelectron from a primary photoionization is given by  $N_{\text{sec}}(E, x_e)$  which is a function of the energy of the photoionizing X-ray and the ionization fraction,  $x_e$ . The probability that a photon has an energy in the interval  $dE$  is given by  $dE/E$ . There are a few simplifying approximations that are made in order to make the integral more tractable. The first approximation is that the hydrogen cross-section is on the order of 10 - 1000 times smaller than that of all elements combined over the

1 - 100 keV energy range [86]. The second is that the secondary ionization rate of hydrogen due to photoelectrons is significantly greater than the primary photoionization rate and that both of these then lead to  $\sigma_{\text{H}}(E) \ll \sigma_{\text{pa}}(E)(E - E_{\text{th}})N_{\text{sec}}(E, x_e)$ . The third approximation is that the energy contribution due to Auger electrons is equivalent to the photoionization threshold energy which leads to  $E - E_{\text{th}} + E_{\text{aug}} = E$  [3, 88]. Finally the fourth is that the number of secondary ionizations is independent of energy per keV and is only dependent on the ionization fraction such that  $N_{\text{sec}}(E, x_e) \simeq N_{\text{sec}}(x_e)$ . With these simplifying approximations in place equation (3.6) becomes

$$\zeta_X \simeq N_{\text{sec}}(x_e) \int_{E_{\text{min}}}^{E_{\text{max}}} F(E) \sigma_{\text{pa}}(E) dE \quad [\text{s}^{-1}]. \quad (3.7)$$

The photoionization cross section per hydrogen nucleus for 1 - 100 keV X-ray photons is then split into a power law fit that is inversely proportional to the energy

$$\sigma_{\text{pa}}(E) = \sigma_X (E/1 \text{ keV})^{-\gamma} \quad [\text{cm}^2], \quad (3.8)$$

where  $\sigma_X = 2.6 \times 10^{-22} \text{ cm}^2$  for  $1 \leq E \leq 7 \text{ keV}$  and  $\sigma_X = 4.4 \times 10^{-22} \text{ cm}^2$  for  $7 \leq E \leq 100 \text{ keV}$  and  $\gamma = 8/3$ . The difference at 7 keV is due to K-shell interactions with Fe. The value used in the model is  $\sigma_X = 2.6 \times 10^{-22} \text{ cm}^2$  [3].

Substituting equations (3.4), (3.5) and (3.8) into equation (3.7) gives

$$\zeta_X \simeq N_{\text{sec}}(x_e) \sigma_X F_{0,X} \int_{E_{\text{min}}}^{E_{\text{max}}} (E/1 \text{ keV})^{-\gamma} (E/1 \text{ keV})^{-\alpha_X} e^{-\tau_X(E)} dE \quad [\text{s}^{-1}], \quad (3.9)$$

where the energy deposition rate in equation (3.9) is given by

$$H_X \simeq \sigma_X F_{0,X} \int_{E_{\text{min}}}^{E_{\text{max}}} (E/1 \text{ keV})^{-\gamma} (E/1 \text{ keV})^{-\alpha_X} e^{-\tau_X(E)} dE \quad [\text{erg s}^{-1}]. \quad (3.10)$$

The attenuation term is energy dependent as  $\tau_X(E) = \sigma_X(E)N_{\text{H}}$ . A change of variables is now made such that  $u \equiv \tau_X E_k^{-\gamma}$  where  $E_k = (E/1 \text{ keV})$  and  $\tau_X$  is the optical depth over the HXR spectrum so that  $e^{-\tau_X(E)} \rightarrow e^u$ ,  $\tau_X = \sigma_X N_{\text{H}}$ , and  $\sigma_X = 2.6 \times 10^{-22} \text{ cm}^2$ . The differential then becomes  $dE = -\tau_X^{-1} \gamma^{-1} E_k^{-\gamma+1} du$ , and the limits of integral go as  $\int_{E_{\text{min}}}^{E_{\text{max}}} \rightarrow \int_{u_{E,\text{min}}}^{u_{E,\text{max}}}$ . Making these

substitutions into equation (3.10) then gives

$$H_X \simeq \frac{\sigma_X F_{0,X}}{\gamma \tau_X} \int_{u_{\min}}^{u_{\max}} E_k^{-(\alpha_X-1)} e^u du \quad [\text{erg s}^{-1}], \quad (3.11)$$

where  $u_{\min} \equiv u_{E,\max}$  and  $u_{\max} \equiv u_{E,\min}$ . Note that the limits of integration flipped from equation (3.10)  $\rightarrow$  (3.11) since  $dE \propto -du$ . Substituting  $E_k = (u/\tau_X)^{-1/\gamma}$  into equation (3.11),  $H_X$  becomes

$$H_X \simeq \frac{\sigma_X F_{0,X}}{\gamma \tau_X^{\phi+1}} \int_{u_{\min}}^{u_{\max}} u^\phi e^u du \quad [\text{erg s}^{-1}] \quad (3.12)$$

where  $\phi \equiv (\alpha_X - 1)/\gamma$ .

The integral in equation (3.12) represents the total energy dependent attenuation of the HXR field over the energy range being considered up to a column density  $N_H$ . Its form is of the generalized incomplete gamma function. The upper incomplete gamma function is represented by

$$\Gamma(\phi + 1, x) = \int_x^\infty u^\phi e^{-u} du. \quad (3.13)$$

The integral in can then be represented by the difference of upper incomplete gamma functions <sup>1</sup> and will be defined as

$$S(\tau_X) \equiv \Gamma(\phi + 1, u_{\min}) - \Gamma(\phi + 1, u_{\max}) = \int_{u_{\min}}^\infty u^\phi e^{-u} du - \int_{u_{\max}}^\infty u^\phi e^{-u} du, \quad (3.14)$$

where  $u_{\min} = \tau_X E_{k,\max}^{-\gamma}$ ,  $u_{\max} = \tau_X E_{k,\min}^{-\gamma}$ ,  $E_{k,\max} = 100$  keV,  $E_{k,\min} = 1$  keV, and gamma is the energy proportionality of photoionization cross section of  $E_k \gtrsim 1$  keV.

Thus the energy deposition rate from the hard X-ray spectrum, equation (3.12) becomes

$$H_X \simeq \frac{\sigma_X}{\gamma} \frac{S(\tau_X)}{\tau_X^{\phi+1}} F_{0,X} \quad [\text{erg s}^{-1}]. \quad (3.15)$$

Further details on the attenuation of the HXR spectrum  $S(\tau_X)/\tau_X^{\phi+1}$  and its effect on the energy deposition rate  $H_X$  is given in Appendix B.

The integrated X-ray flux over the 1 - 100 keV at the cloud face is given by integrating the

---

<sup>1</sup> This can also be represented as the difference of lower incomplete gamma functions where  $\gamma(\phi + 1, x) = \int_0^x u^\phi e^{-u} du$  so that  $\gamma(\phi + 1, u_{\max}) - \gamma(\phi + 1, u_{\min}) = \int_0^{u_{\max}} u^\phi e^{-u} du - \int_0^{u_{\min}} u^\phi e^{-u} du$ .

X-ray SED, equation (3.4), and is given by

$$F_X = F_{0,X} \int_{E_{k,\min}}^{E_{k,\max}} E_k^{-\alpha_X} dE_k \quad [\text{erg cm}^{-2} \text{ s}^{-1}], \quad (3.16)$$

where  $E_k$  has been normalized to 1 keV as mentioned earlier. Denoting the integral by  $F_{\alpha_X}$ , the energy deposition rate in terms of the 1 - 100 keV X-ray flux becomes

$$H_X \simeq \frac{\sigma_X}{\gamma F_{\alpha_X}} \frac{S(\tau_X)}{\tau_X^{\phi+1}} F_X \quad [\text{erg s}^{-1}], \quad (3.17)$$

where

$$\begin{aligned} F_{\alpha_X} &= \frac{E_{k,\max}^{1-\alpha_X} - E_{k,\min}^{1-\alpha_X}}{1 - \alpha_X} \quad (\alpha_X \neq 1) \\ F_{\alpha_X} &= \ln\left(\frac{E_{k,\max}}{E_{k,\min}}\right) \quad (\alpha_X = 1). \end{aligned} \quad (3.18)$$

The energy deposition rate per hydrogen nucleus can be given as

$$\frac{H_X}{n_H} \simeq \frac{\sigma_X}{\gamma F_{\alpha_X}} \frac{S(\tau_X)}{\tau_X^{\phi+1}} \frac{F_X}{n_H} \quad [\text{erg cm}^3 \text{ s}^{-1}]. \quad (3.19)$$

For a source of X-ray radiation with a given luminosity of  $L_X \text{ erg s}^{-1}$ , the flux is found through the relation  $F_X = L_X/4\pi r^2$  where  $r$  is the distance from the source to the point in question. The ratio of the photon luminosity to the total number density of hydrogen nuclei is given by the ionization parameter [89]

$$\xi \equiv \frac{L_X}{n_H r^2} \quad [\text{erg cm s}^{-1}]. \quad (3.20)$$

Relating the ionization parameter, equation (3.20), to the photon flux gives

$$\xi = \frac{4\pi F_X}{n_H} \quad [\text{erg cm s}^{-1}]. \quad (3.21)$$

With this, the ratio of the energy deposition rate per nuclei in terms of the ionization parameter is now

$$\frac{H_X}{n_H} \simeq \frac{\sigma_X}{4\pi\gamma F_{\alpha_X}} \frac{S(\tau_X)}{\tau_X^{\phi+1}} \xi \quad [\text{erg cm}^3 \text{ s}^{-1}]. \quad (3.22)$$

### 3.1.2 Molecular Hydrogen Destruction

Now that the energy deposition rate has been found, the rate of total hydrogen ionization, equation (3.3), can be returned to. For low ionization fractions,  $x_e \lesssim 10^{-3}$ , the amount of energy from primary photoelectrons that goes towards the ionization of secondary electrons is on the order of 40%. This is the case for both atomic and molecular hydrogen [3, 88, 90]. As such the ionization rate equation is modified by the fraction of energy that is deposited as secondary ionizations,  $f_i$ .

This low ionization fraction is necessary for the destruction of molecular hydrogen by secondary electrons to be efficient. When ionization fractions start to increase, the kinetic energy of the non-thermal electrons is given up to the thermalization of other electrons due to Coulombic interactions. The pathway to molecular hydrogen destruction by the interaction of secondary electrons begins with the creation of a dihydrogen cation in the ionization reaction



The  $\text{H}_2^+$  ions are then removed from the gas in the proton transfer reaction with  $\text{H}_2$  to create the trihydrogen cation



The removal of  $\text{H}_3^+$  from the gas may occur via the charge transfer reaction with a molecule other than  $\text{H}_2$  in the gas, creating a different ionic species, or else in either of the dissociative recombination reactions



or



where the number in brackets is the probability of occurrence [3].

A significant amount of molecular hydrogen destruction will also occur from FUV photons that are produced by the non-thermal electrons exciting  $\text{H}_2$  into the Lyman-Werner band states. Details of the photodissociation of molecular hydrogen from FUV is discussed in § 2.1.2.1 and it's effect is discussed in § 3.2.1.

The number of secondary ionizations  $N_{\text{sec}}$  is given by the energy deposited towards secondary ionizations divided by the ionization energy of the relevant species. For H this is 13.598 eV, and for H<sub>2</sub> it is 15.426 eV. This can be expressed conveniently in terms of number of ionizations per keV. For 1 keV of deposited energy, with  $f_i \sim 0.4$ , then 0.4 keV goes towards secondary ionizations. As such  $N_{\text{H}^0, \text{sec}} \approx (0.4)/(0.013598 \text{ keV}) \approx 29.4 \text{ keV}^{-1}$  and  $N_{\text{H}_2, \text{sec}} \approx (0.4)/(0.015426 \text{ keV}) \approx 25.9 \text{ keV}^{-1}$ . The ionization energy of H and H<sub>2</sub> can be equivalently given as  $2.1786 \times 10^{-11} \text{ erg}$  and  $2.4715 \times 10^{-11} \text{ erg}$  respectively. Similarly for 1 erg of deposited energy, 0.4 erg goes towards secondary ionizations. As such  $N_{\text{H}^0, \text{sec}} \approx 1.836 \times 10^{10} \text{ erg}^{-1}$  and  $N_{\text{H}_2, \text{sec}} \approx 1.618 \times 10^{10} \text{ erg}^{-1}$ .

The ionization rate, equation (3.3) now becomes

$$\zeta_X \simeq \frac{f_i H_X}{E_i} \quad [\text{s}^{-1}], \quad (3.26)$$

where  $H_X$  is the total energy deposition rate, equation (3.22),  $f_i$  is the fraction of energy deposited towards ionizations, and  $E_i$  is the ionization energy of the particle in question. In terms of the ionization energy per nuclei, equation (3.26) becomes for the ionization rate of atomic hydrogen,

$$\frac{\zeta_{\text{H}^0}}{n_{\text{H}}} \simeq \frac{f_i}{E_{i, \text{H}^0}} \frac{H_X}{n_{\text{H}}} \quad [\text{cm}^3 \text{ s}^{-1}]. \quad (3.27)$$

The above equation can be used in this form as is for atomic hydrogen, with it's ionization energy of 13.598 eV. The ionization rate per molecule of H<sub>2</sub> needs to be modified slightly due to the conservation hydrogen nuclei,  $n_{\text{H}} = n_{\text{H}^0} + 2n_{\text{H}_2}$ . Since there are two H nuclei per molecule of H<sub>2</sub>, then equation (3.27) is

$$\frac{\zeta_{\text{H}_2}}{n_{\text{H}}} \simeq \frac{2f_i}{E_{i, \text{H}_2}} \frac{H_X}{n_{\text{H}}} \quad [\text{cm}^3 \text{ s}^{-1}], \quad (3.28)$$

where  $E_i$  is the ionization energy of H<sub>2</sub>, 15.426 eV. The two ionization rates can then be related by  $\zeta_{\text{H}_2} = 2(E_{i, \text{H}}/E_{i, \text{H}_2})\zeta_{\text{H}}$ .

The reaction of ions in the chemical network will also lead to the dissociation of H<sub>2</sub> molecules. There are on the order of 3 dissociations of H<sub>2</sub> for each hydrogen ionization that occurs [3].

## 3.2 Steady State HXR Field Creation - Destruction of Molecular Hydrogen

Similar to the steady state equation for the formation and destruction of  $\text{H}_2$  in a beamed FUV radiation field, equation (2.1), a creation-destruction equation for a beamed HXR radiation field onto a semi-infinite slab is then

$$R_d n_{\text{H}^0} n_{\text{H}} = \frac{1}{2} D_{\text{HXR}} f_{\text{att},X} n_{\text{H}_2}. \quad (3.29)$$

Here  $R_d$  is the formation rate of  $\text{H}_2$  on grains,  $D_{\text{HXR}}$  is the unattenuated dissociation rate of  $\text{H}_2$  and  $f_{\text{att},X}$  is the attenuation of the X-ray field.

The unattenuated energy deposition rate per hydrogen nucleus, equation (3.19) is denoted as

$$\frac{H_{0,X}}{n_{\text{H}}} \simeq \frac{\sigma_X}{\gamma F_{\alpha_X}} \frac{F_X}{n_{\text{H}}} \quad [\text{erg cm}^3 \text{ s}^{-1}]. \quad (3.30)$$

and the unattenuated ionization rate, equation (3.28) as

$$\frac{\zeta_{0,\text{H}_2}}{n_{\text{H}}} \simeq \frac{2f_i}{E_{i,\text{H}_2}} \frac{H_{0,X}}{n_{\text{H}}} \quad [\text{cm}^3 \text{ s}^{-1}], \quad (3.31)$$

where the number of secondary ionizations of per erg per of deposited X-ray energy per  $\text{H}_2$  molecule is given by

$$N_{\text{H}_2,\text{sec}} \equiv \frac{2f_i}{E_{i,\text{H}_2}} = 3.24 \times 10^{10} \quad [\text{erg}^{-1}], \quad (3.32)$$

and the fixed coefficients making up  $H_{0,X}$  have a numerical value of

$$k_H \equiv \frac{\sigma_X}{\gamma F_{\alpha_X}} = 9.81 \times 10^{-24} \quad [\text{cm}^2]. \quad (3.33)$$

The coefficients making up the energy deposition rate have the units of an effective cross section for the HXR energy flux.

As was done for the PDR case, equation (3.29) can be given as the ratio of atomic-to-molecular hydrogen densities as

$$\frac{n_{\text{H}^0}}{n_{\text{H}_2}} = \frac{1}{2} \frac{D_{\text{HXR}}}{R_d n_{\text{H}}} f_{\text{att},X}. \quad (3.34)$$

From the energy deposition rate per hydrogen nucleus and the molecular hydrogen ionization rate per hydrogen nucleus, equations (3.19) and (3.28) respectively, we define the ratio of the unattenuated dissociation rate of H<sub>2</sub> due to X-rays  $D_{HXR}$ , and its formation rate on grains per hydrogen nucleus by the dimensionless quantity  $\beta_{HXR}$ , where

$$\beta_{HXR} \equiv \frac{12 f_i}{E_{i,H_2}} \frac{\sigma_X}{\gamma F_\alpha} \frac{F_X}{R_d n_H} = \frac{D_{HXR}}{R_d n_H}, \quad (3.35)$$

and

$$D_{HXR} \equiv 3 \zeta_{0,H_2} = \frac{12 f_i}{E_{i,H_2}} \frac{\sigma_X}{\gamma F_\alpha} F_X \quad [\text{s}^{-1}]. \quad (3.36)$$

As previously mentioned, there are on the order of 3 dissociations of H<sub>2</sub> for each hydrogen ionization that occurs which accounts for the in 3 in equation (3.36) [3]. The factor of 12 in equation (3.35) comes from equation (3.28) (a factor of 2 from the number of nuclei in a hydrogen molecule), the discussion below equation (3.28) (a factor of 3 from the number of H<sub>2</sub> molecules destroyed per ionization), and equation (2.13) (a factor of 2 from the increase in surface flux when considering an isotropic free-space flux density of a radiation field from it's beamed equivalent upon a semi-infinite slab). The other constants can be inserted into equation (3.35) in order to simplify the  $\beta$  term. With the assumption that there is a low ionization fraction  $x_e \lesssim 10^{-3}$ , the fraction of energy deposited leading to secondary ionizations is  $f_i \sim 0.4$  [3]. The ionization energy of H<sub>2</sub>,  $E_i$  is  $2.4715 \times 10^{-11}$  erg. The photoionization cross section of 1 keV X-rays is  $\sigma_X = 2.6 \times 10^{-22}$  cm<sup>-2</sup>, the energy dependance at 1 keV is  $\gamma = 8/3$ , and the integral of the spectral shape between 1 keV and 100 keV for a power-law index of  $\alpha_X = 0.7$  gives  $F_{\alpha_X} = 9.9369$ .

We define the constant

$$k_I \equiv \frac{12 f_i}{E_{i,H_2}} = 1.94 \times 10^{11} \quad [\text{erg}^{-1}], \quad (3.37)$$

which represents the number of H<sub>2</sub> molecules destroyed due to ionizations from secondary electrons per erg of deposited energy. In terms of the constants given in equations (3.33) and (3.37), the destruction rate from the HXR spectrum is

$$\frac{D_{HXR}}{n_H} = k_{HXR} \frac{F_X}{n_H} \quad [\text{cm}^3 \text{s}^{-1}], \quad (3.38)$$

where

$$k_{HXR} \equiv k_I k_H = \frac{12 f_i \sigma_X}{E_{i,H_2} \gamma F_\alpha} \quad [\text{cm}^2 \text{erg}^{-1}]. \quad (3.39)$$

The numerical value of the HXR destruction rate per hydrogen nucleus in equation (3.38) is then given as

$$\frac{D_{HXR}}{n_H} = 1.91 \times 10^{-12} \frac{F_X}{n_H} \quad [\text{cm}^3 \text{s}^{-1}]. \quad (3.40)$$

As the  $\text{H}_2$  formation rate on dust grains is proportional to the normalized dust grain cross section, equation (2.93), we can substitute this in so that  $R_d = 3 \times 10^{-17} \tilde{\sigma}_d \text{ cm}^3 \text{ s}^{-1}$ , where we have assumed a gas temperature of  $T = 100 \text{ K}$ . Substituting these values into equation (3.35) leads to

$$\beta_{HXR} = 6.35 \times 10^4 \frac{F_X}{\tilde{\sigma}_d n_H}. \quad (3.41)$$

The terms that enter equation (3.41) as parameters are the free-space hard X-ray flux  $F_X \text{ erg cm}^{-2} \text{ s}^{-1}$ , the total hydrogen number density  $n_H \text{ cm}^{-3}$ , and the normalized dust grain cross section  $\tilde{\sigma}_d$ . Thus  $\beta_{HXR}$  is the ratio of the free-space HXR flux at the cloud face per hydrogen nucleus ( $F_X/n_H$ ), and the normalized dust grain cross-section  $\tilde{\sigma}_d$ .

From equations (3.1) and (3.19) we define the attenuation due to energy dependent optical depth to be denoted by the dimensionless parameter  $B$ , where

$$f_{\text{att},X} \equiv B \equiv \frac{S(\tau_X)}{\tau_X^{\phi+1}}. \quad (3.42)$$

The optical depth in equation (3.42) is given by  $\tau_X = \sigma_X N_H$ , where  $\sigma_X = 2.6 \times 10^{-22} \text{ cm}^2$ , so that  $B$  is dependent on the total hydrogen column density  $N_H$ , and scales as  $N_H^{-\phi-1}$ , where  $\phi = (\alpha_X - 1)/\gamma$  from equation (3.12). With  $\alpha_X = 0.7$  and  $\gamma = 8/3$  from the discussion below equation (3.35),  $\phi = -0.1125$ , and  $\phi + 1 = 0.8875$ . Further discussion on  $S(\tau_X)$  and equation (3.42) is given in Appendix B.

Combining equations (3.35) and (3.42) leads to

$$\beta_{HXR} B \equiv \frac{12 f_i \sigma_X}{E_{i,H_2} \gamma F_{\alpha_X}} \frac{F_X}{R_d n_H} \frac{S(\tau_X)}{\tau_X^{\phi+1}} = \frac{D_{HXR}}{R_d n_H} \frac{S(\tau_X)}{\tau_X^{\phi+1}}. \quad (3.43)$$

Thus,  $\beta_{HXR} B$  represents the ratio of the free space  $\text{H}_2$  destruction rate due to a hard X-ray

spectrum per hydrogen nucleus to the free space  $\text{H}_2$  formation rate attenuated by the HXR optical depth. With the use of the constant in equation (3.39)  $\beta_{HXR}B$  is

$$\beta_{HXR}B = k_{HXR} \frac{F_X}{R_d n_H} \frac{S(\tau_X)}{\tau_X^{\phi+1}}. \quad (3.44)$$

Using equations (3.41) and (3.42) casts  $\beta B$  into the form

$$\beta_{HXR}B = 6.35 \times 10^4 \frac{F_X}{\tilde{\sigma}_d n_H} \frac{S(\tau_X)}{\tau_X^{\phi+1}}. \quad (3.45)$$

The terms that enter equation (3.45) as parameters are the free-space hard X-ray flux  $F_X \text{ erg cm}^{-2} \text{ s}^{-1}$ , the total hydrogen number density  $n_H \text{ cm}^{-3}$ , and the normalized dust grain cross section  $\tilde{\sigma}_d$ , attenuated by the HXR optical depth.

The ratio of atomic-to-molecular hydrogen for an attenuated HXR radiation field can then be given as

$$\frac{n_{\text{H}^0}}{n_{\text{H}_2}} = \frac{1}{2} k_{HXR} \frac{F_X}{R_d n_H} \frac{S(\tau_X)}{\tau_X^{\phi+1}}, \quad (3.46a)$$

or equivalently,

$$\frac{n_{\text{H}^0}}{n_{\text{H}_2}} = \frac{1}{2} \beta_{HXR}B. \quad (3.46b)$$

### 3.2.1 Internally Generated UV Field due to Secondary Electrons

The interaction of secondary electrons due to the flux of HXR into the molecular cloud creates a secondary source of electromagnetic radiation. These non-thermal electrons, in addition to causing the ionization of molecular hydrogen, are also capable of exciting  $\text{H}_2$  into the Lyman-Werner, (i.e. the  $B^1\Sigma_u$  or  $C^1\Pi_u$  states respectively) or higher states [27, 28, 29]. The decay of these excited states leads to the production of FUV photons in the 6 - 13.6 eV energy range. These wavelengths range from 90 to 170 nm for the Lyman lines and 90 to 130 nm for the Werner lines [91]. As discussed in § 2.1.2.1, approximately 12% of the decays will be to the vibrational continuum leading to the photodissociation of  $\text{H}_2$ . When ionization fractions in the gas are low,  $x_e \lesssim 10^{-3}$ , approximately 40% of the deposited energy due to the non-thermal electrons leads to the production of these FUV photons [3]. More recent calculations show that for low ionization fractions, the fraction of deposited energy leads to approximately 50% of the deposited energy going towards excitation

processes [92]. The value of 40% will be used for this model.

A relation between the energy flux from an HXR illuminated cloud and the flux of an internally generated FUV field is given by [3]

$$\frac{G_0}{n_H} = 6 \times 10^{23} f_{X \rightarrow U} \frac{H_X}{n_H} \quad [\text{cm}^3], \quad (3.47)$$

where  $G_0/n_H$  is the ratio of the normalized free-space isotropic Habing FUV radiation field to the total hydrogen density [8],  $f_{X \rightarrow U}$  is the fraction of deposited X-ray energy that is converted to FUV photons, and  $H_X$  is the energy deposition rate due to the HXR flux, equation (3.17). Here  $G_0$  has been normalized over the 6 - 13.6 eV (912 - 2066 Å) energy range of the Habing FUV spectrum, equation (A.10) such that

$$G_0 = \frac{F_{0,XUV}}{1.58 \times 10^{-3} \text{ erg cm}^{-2} \text{ s}^{-1}}, \quad (3.48)$$

where  $F_{0,XUV}$  is the energy flux of secondary electron induced FUV radiation. The coefficient in equation (3.47) has dimensions of  $\text{s erg}^{-1}$  in order for  $G_0$  to be dimensionless. Inserting equation (3.17) into equation (3.47) gives

$$\frac{G_0}{n_H} = 6 \times 10^{23} f_{X \rightarrow U} \frac{\sigma_X}{\gamma F_{\alpha_X}} \frac{F_X}{n_H} \frac{S(\tau_X)}{\tau_X^{\phi+1}} \quad [\text{cm}^3], \quad (3.49)$$

and then inserting the values of  $f_{X \rightarrow U} = 0.4$ ,  $\sigma_X = 2.6 \times 10^{-22} \text{ cm}^2$ ,  $\gamma = 8/3$ , and  $F_{\alpha_X} = 9.94$  leads to

$$\frac{G_0}{n_H} = 2.35 \frac{F_X}{n_H} \frac{S(\tau_X)}{\tau_X^{\phi+1}} \quad [\text{cm}^3], \quad (3.50)$$

where  $F_X$  is the X-ray energy flux  $\text{erg cm}^{-2} \text{ s}^{-1}$  and  $S(\tau_X)/\tau_X$  is its column density dependent attenuation. Using equation (3.48) in equation (3.50), the induced FUV energy flux can then be given as

$$\frac{F_{0,XUV}}{n_H} = 3.73 \times 10^{-3} \frac{F_X}{n_H} \frac{S(\tau_X)}{\tau_X^{\phi+1}} \quad [\text{erg cm s}^{-1}]. \quad (3.51)$$

If we want to consider the contribution of the internally generated FUV energy flux for the Habing SED over the 11.2 - 13.6 eV range (LW band), then the values from Table (A.1) can be used. Letting  $F_{0,H} = 1.58 \times 10^{-3} \text{ erg cm}^{-2} \text{ s}^{-1}$  be the energy flux over the 6 - 13.6 eV energy range and  $F_{LW,H} = 2.37 \times 10^{-4} \text{ erg cm}^{-2} \text{ s}^{-1}$  over the 11.2 - 13.6 eV energy range. They are then simply

related by  $F_{\text{LW,H}} = 0.1495 F_{0,\text{H}}$ , or equivalently that  $\sim 15\%$  of the FUV photons produced are in the LW band. From this and equation (3.51), the LW-band energy flux of a Habing SED due to the energy deposition of an HXR radiation field is given as

$$\frac{F_{\text{LW,H,XUV}}}{n_{\text{H}}} = 5.58 \times 10^{-4} \frac{F_X}{n_{\text{H}}} \frac{S(\tau_X)}{\tau_X^{\phi+1}} \quad [\text{erg cm s}^{-1}]. \quad (3.52)$$

We define the normalized energy flux of the Sternberg version of the Draine FUV spectrum, equation (A.44), over the 6 - 13.6 eV range as

$$G_{0,\text{DS}} = \frac{F_{0\text{DS},\text{XUV}}}{2.68 \times 10^{-3} \text{ erg cm}^{-2} \text{ s}^{-1}}, \quad (3.53)$$

which corresponds to  $G_{0,\text{DS}} = \chi G_0$ , where a comparison of equations (3.48) and (3.53) gives the scaling factor  $\chi = 1.69$  for both unit  $G_0$  and  $G_{0,\text{DS}}$  over the 6 - 13.6 eV range. The normalized free-space isotropic Sternberg variation of the Draine FUV radiation field for internal UV photons produced by secondary electrons can then be given by modifying equation (3.47) such that

$$\frac{G_{0,\text{DS}}}{n_{\text{H}}} = 3.55 \times 10^{23} f_{X \rightarrow U} \frac{H_X}{n_{\text{H}}} \quad [\text{cm}^3]. \quad (3.54)$$

Referring to equations (3.49) and (3.54) then this can be given as

$$\frac{G_{0,\text{DS}}}{n_{\text{H}}} = 1.39 \frac{F_X}{n_{\text{H}}} \frac{S(\tau_X)}{\tau_X^{\phi+1}} \quad [\text{cm}^3]. \quad (3.55)$$

Using equation (3.53) in equation (3.55), the induced FUV energy flux for an SED given by equation (A.44) is

$$\frac{F_{0\text{DS},\text{XUV}}}{n_{\text{H}}} = 3.73 \times 10^{-3} \frac{F_X}{n_{\text{H}}} \frac{S(\tau_X)}{\tau_X^{\phi+1}} \quad [\text{erg cm s}^{-1}]. \quad (3.56)$$

The change in normalization between the the two forms of  $G_0$  lead to an adjustment of the coefficient in equations (3.47) and (3.49). This maintains the total internal FUV flux,  $F_{\text{XUV}}$  produced by the secondary electrons due to a given amount of HXR flux over the given 6 - 13.6 eV energy range, as this is independent of the normalization used. To consider the contribution of the internally generated FUV energy flux for the Draine SED given by Sternberg over the 11.2 - 13.6 eV range (LW band), then the values from Table (A.4) can be used. Letting  $F_{0,\text{DS}} = 2.68 \times 10^{-3} \text{ erg cm}^{-2} \text{ s}^{-1}$

be the energy flux over the 6 - 13.6 eV energy range and  $F_{\text{LW,DS}} = 3.99 \times 10^{-4} \text{ erg cm}^{-2} \text{ s}^{-1}$  over the 11.2 - 13.6 eV energy range. They are then simply related by  $F_{\text{LW,DS}} = 0.149 F_{0,\text{SD}}$ , or equivalently that  $\sim 15\%$  of the FUV photons produced are in the LW band, approximately the same for the Habing field. This relation can be defined as

$$k_{\text{FLW}} \equiv 6 \times 10^{23} f_{X \rightarrow U} F_{0,\text{H}} \frac{F_{\text{LW,DS}}}{F_{0,\text{DS}}} \quad [\text{cm}^{-2}], \quad (3.57)$$

The energy flux of internally generated LW band photons in the Draine-Sternberg SED from secondary electrons due to HXR is then given by

$$\frac{F_{\text{LW,DS,XUV}}}{n_{\text{H}}} = k_{\text{FXU}} \frac{F_{\text{X}}}{n_{\text{H}}} \frac{S(\tau_{\text{X}})}{\tau_{\text{X}}^{\phi+1}} \quad [\text{erg cm s}^{-1}], \quad (3.58a)$$

where

$$k_{\text{FXU}} \equiv k_{\text{FLW}} k_{\text{H}} = 5.56 \times 10^{-4}, \quad (3.58b)$$

which is unitless, where  $F_{\text{X}}$  is the X-ray energy flux [ $\text{erg cm}^{-2} \text{ s}^{-1}$ ], and  $S(\tau_{\text{X}})/\tau_{\text{X}}^{\phi+1}$  is its column density dependent energy deposition. Note that the HXR flux  $F_{\text{LW,DS,XUV}}$ , in equation (3.58a) is of the same spectrum as  $I_{\text{U}}$ , where  $I_{\text{U}} = (F_{\text{LW,DS,XUV}}/3.99 \times 10^{-4} \text{ erg cm}^{-2} \text{ s}^{-1})$  as described in §2.2.

### 3.3 Steady State XUV Field Creation - Destruction of Molecular Hydrogen

In order to find the combined steady state transition point when the induced FUV radiation field is included a few adjustments need to be made. A key difference to the FUV radiation field produced internally in the cloud due to the non-thermal electrons is that they are isotropic in nature. Also, the external FUV radiation field undergoes an attenuation due to self-shielding and dust absorption as it travels through the cloud. These internal FUV photons cannot then simply be added to the  $\alpha$  parameter from § 2.2 due to these reasons. Below we will show how to include them with the steady-state HXR equation (3.1).

Treating the interaction of the X-ray induced FUV radiation field (denoted as XUV) with the

molecular cloud as an independent steady-state creation-destruction equation in a similar form to equations (2.1) and (3.1) we have

$$R_d n_{\text{H}^0} n_{\text{H}} = \frac{1}{4} D_{\text{XUV}} f_{\text{att},\text{XUV}} n_{\text{H}_2} \quad [\text{cm}^{-3} \text{s}^{-1}], \quad (3.59)$$

where  $D_{\text{XUV}} \text{s}^{-1}$  is the free space dissociation rate due to XUV photons,  $f_{\text{att},\text{XUV}}$  is any attenuation of the XUV,  $R_d \text{cm}^3 \text{s}^{-1}$  is the  $\text{H}_2$  formation rate coefficient as in equation (2.94), and  $n_{\text{H}^0}, n_{\text{H}_2}$  and  $n_{\text{H}}$  are the atomic, molecular, and total hydrogen densities respectively. The factor of 1/4 is due to equation (3.59) being represented by an isotropic radiation field that is considered to only dissociate molecular hydrogen in the forward direction. The flux of an isotropic field is 1/2 that of a beamed field as is given in equations (2.1) and (3.1).

Since we are considering the XUV radiation field to be that described by a Draine-Sternberg FUV spectrum in the Lyman-Werner band, the unattenuated free space dissociation rate  $D_{\text{XUV}}$  is the same as that given in equation (2.97) with the notation

$$D_{\text{XUV}} = 5.81 \times 10^{-11} I_U \quad [\text{s}^{-1}], \quad (3.60)$$

where  $I_U = (F_{\text{LW,DS,XUV}}/3.99 \times 10^{-4} \text{erg cm}^{-2} \text{s}^{-1})$  is the unit Draine field. As in equation (2.96), the dissociation rate is a product of the flux of radiation in the LW band and an effective cross section that leads to dissociation given by

$$D_{\text{XUV}} = F_{\text{LW,XUV}} \sigma_{\text{LW}} \quad [\text{s}^{-1}]. \quad (3.61)$$

An effective dissociation cross section per erg in the over an integrated LW band can be given by

$$\sigma_{\text{LW}} = 1.46 \times 10^{-7} \quad [\text{cm}^2 \text{erg}^{-1}], \quad (3.62)$$

where a photon flux of  $F_{\text{LW}} = 3.99 \times 10^{-4} \text{erg cm}^{-2} \text{s}^{-1}$  was used. As discussed below equation (2.98), this effective dissociation cross section underestimates the effective absorption cross section by approximately an order of magnitude.

Writing equation (3.59) as the ratio of atomic-to-molecular hydrogen densities gives,

$$\frac{n_{\text{H}^0}}{n_{\text{H}_2}} = \frac{1}{4} \frac{D_{XUV}}{R_d n_{\text{H}}} f_{\text{att},XUV}. \quad (3.63)$$

This represents the atomic to molecular hydrogen density profiles for an induced XUV field only. A ratio of atomic to molecular hydrogen densities can now be given that is a combination of the HXR and its associated XUV radiation field. From equations (3.34) and (3.63) this is given as

$$\frac{n_{\text{H}^0}}{n_{\text{H}_2}} = \frac{1}{2} \frac{D_{HXR}}{R_d n_{\text{H}}} f_{\text{att},HXR} + \frac{1}{4} \frac{D_{XUV}}{R_d n_{\text{H}}} f_{\text{att},XUV}. \quad (3.64)$$

Equation (3.64) thus gives the atomic to molecular hydrogen density ratio as a combination of the  $\text{H}_2$  destruction rates based on the direct ionization leading to dissociation from secondary non-thermal electrons (the first term on the right hand side) and the photodissociation due to induced LW band FUV photons from the non-thermal electrons colliding with molecular hydrogen (the second term on the right hand side). The first term in the above equation containing  $D_{HXR}$  has already been given directly as a function the HXR flux,  $F_X$ , as in the numerator of equation (3.40). The second term containing  $D_{XUV}$  can also be given as directly dependent on the HXR flux. Equation (3.64) will be developed further in § 3.4.

A brief summary of the substitutions of the previously derived formulae follows. First note that from equations (3.47) and (3.48), the flux of FUV photons produced in the 6 - 13.6 eV range of a Habing spectrum in terms of the energy deposition per hydrogen nucleus of the HXR field is

$$\frac{F_{0,XUV}}{n_{\text{H}}} = 6 \times 10^{23} f_{X \rightarrow U} F_{0,\text{H}} \frac{H_X}{n_{\text{H}}} \quad [\text{erg cm s}^{-1}], \quad (3.65)$$

where  $F_{0,\text{H}} = 1.58 \times 10^{-3} \text{ erg cm}^{-2} \text{ s}^{-1}$ . This FUV flux can be converted to the amount of energy flux that would be present in the LW band of a Draine-Sternberg FUV spectrum by multiplying it by the ratio  $F_{\text{LW,DS}}/F_{0,\text{DS}}$  so that equation (3.65) becomes

$$\frac{F_{\text{LW},XUV}}{n_{\text{H}}} = 6 \times 10^{23} f_{X \rightarrow U} F_{0,\text{H}} \frac{F_{\text{LW,DS}}}{F_{0,\text{DS}}} \frac{H_X}{n_{\text{H}}} \quad [\text{erg cm s}^{-1}], \quad (3.66)$$

where  $F_{\text{LW,DS}} = 3.99 \times 10^{-4} \text{ erg cm}^{-2} \text{ s}^{-1}$  and  $F_{0,\text{DS}} = 2.68 \times 10^{-3} \text{ erg cm}^{-2} \text{ s}^{-1}$ . Inserting equa-

tion (3.17) into equation (3.66) gives the FUV flux in the LW band of a Draine-Sternberg spectrum produced from the collision of secondary electrons as

$$\frac{F_{\text{LW},XUV}}{n_{\text{H}}} = 6 \times 10^{23} f_{X \rightarrow U} F_{0,\text{H}} \frac{F_{\text{LW,DS}}}{F_{0,\text{DS}}} \frac{\sigma_X}{\gamma F_{\alpha_X}} \frac{F_X}{n_{\text{H}}} \quad [\text{erg cm s}^{-1}]. \quad (3.67)$$

The unattenuated destruction rate of  $\text{H}_2$  per hydrogen nuclei can now be given by inserting equation (3.67) into equation (3.61) giving

$$\frac{D_{XUV}}{n_{\text{H}}} = 6 \times 10^{23} f_{X \rightarrow U} F_{0,\text{H}} \frac{F_{\text{LW,DS}}}{F_{0,\text{DS}}} \sigma_{\text{LW}} \frac{\sigma_X}{\gamma F_{\alpha_X}} \frac{F_X}{n_{\text{H}}} \quad [\text{cm}^3 \text{s}^{-1}], \quad (3.68)$$

with  $\sigma_{\text{LW}} = 1.46 \times 10^{-7} \text{ cm}^2 \text{ erg}^{-1}$  as given in equation (3.62). The gross energy deposition rate ( $\sim 0.4$ ) is the same ratio for both the production of secondary electrons via ionization and for the production of LW band photons via collisions from secondary electrons. From this it can be seen in equations (3.36) and (3.68) that the unattenuated energy deposition rate is identical

$$\frac{H_{0,X}}{n_{\text{H}}} = k_{\text{H}} \frac{F_X}{n_{\text{H}}} \quad [\text{erg cm}^3 \text{s}^{-1}], \quad (3.69a)$$

where

$$k_{\text{H}} \equiv \frac{\sigma_X}{\gamma F_{\alpha_X}} = 9.81 \times 10^{-24} \quad [\text{cm}^2]. \quad (3.69b)$$

The net energy deposition rate is also the same in both cases since the fraction of HXR that is converted to secondary electrons is on the order of  $f_i = f_{X \rightarrow U} \sim 0.4$ .

From equations (3.59) and (3.68) we define the ratio of the unattenuated dissociation rate of  $\text{H}_2$  due to X-ray induced FUV rays,  $D_{XUV}$ , and its formation rate on grains per hydrogen nucleus by the dimensionless quantity  $\beta_{XUV}$  where

$$\beta_{XUV} \equiv 6 \times 10^{23} f_{X \rightarrow U} F_{0,\text{H}} \frac{F_{\text{LW,DS}}}{F_{0,\text{DS}}} \sigma_{\text{LW}} \frac{\sigma_X}{\gamma F_{\alpha_X}} \frac{F_X}{R_{\text{d}} n_{\text{H}}} = \frac{D_{XUV}}{R_{\text{d}} n_{\text{H}}}. \quad (3.70)$$

In a similar manner to equation (3.37) we define the constant

$$k_{\text{DLW}} \equiv 6 \times 10^{23} f_{X \rightarrow U} F_{0,\text{H}} \frac{F_{\text{LW,DS}}}{F_{0,\text{DS}}} \sigma_{\text{LW}} = 8.25 \times 10^{12} \quad [\text{erg}^{-1}], \quad (3.71)$$

which represents the number of dissociations due to internal LW photons produced by molecular excitation from secondary electrons per erg of deposited energy. In terms of the constants given in equations (3.69b) and (3.71), the destruction rate from the XUV spectrum is

$$\frac{D_{XUV}}{n_H} = k_{XUV} \frac{F_X}{n_H} \quad [\text{cm}^3 \text{ s}^{-1}], \quad (3.72a)$$

where

$$k_{XUV} \equiv k_{DLW} k_H = 6 \times 10^{23} f_{X \rightarrow U} F_{0,H} \frac{F_{LW,DS}}{F_{0,DS}} \sigma_{LW} \frac{\sigma_X}{\gamma F_{\alpha X}} \quad [\text{cm}^2 \text{ erg}^{-1}], \quad (3.72b)$$

and

$$k_{XUV} = 8.10 \times 10^{-11} \quad [\text{cm}^2 \text{ erg}^{-1}] \quad (3.72c)$$

The destruction rate of  $\text{H}_2$  per nuclei for a given  $F_X$  is then

$$\frac{D_{XUV}}{n_H} = 8.10 \times 10^{-11} \frac{F_X}{n_H} \quad [\text{cm}^3 \text{ s}^{-1}]. \quad (3.73)$$

As the  $\text{H}_2$  formation rate on dust grains is proportional to the normalized dust grain cross section, equation (2.93), we can substitute this in so that  $R_d = 3 \times 10^{-17} \tilde{\sigma}_d \text{ cm}^3 \text{ s}^{-1}$ , where we have assumed a gas temperature of  $T = 100$  K. Substituting these values into equation (3.35) leads to

$$\beta_{XUV} = 2.70 \times 10^6 \frac{F_X}{\tilde{\sigma}_d n_H}. \quad (3.74)$$

The terms that enter equation (3.74) as parameters are the free-space hard X-ray flux  $F_X$  [ $\text{erg cm}^{-2} \text{ s}^{-1}$ ], the total hydrogen number density  $n_H$  [ $\text{cm}^{-3}$ ], and the normalized dust grain cross section  $\tilde{\sigma}_d$ . Thus  $\beta_{XUV}$  is the ratio of the free-space HXR induced dissociation rate per hydrogen nucleus ( $F_X/n_H$ ), and the normalized dust grain cross-section  $\tilde{\sigma}_d$ .

Since the energy deposition rate is dependent on the optical depth as  $S(\tau_X)/\tau_X^{\phi+1}$ , this attenuation term is also a common factor in the dissociation of  $\text{H}_2$  for both the ionizing effects of secondary electrons as well as the dissociation from LW band photons produced by molecular collisions. When these LW - XUV photons are produced during molecular collisions, we are assuming that they travel only a short distance before they are absorbed by an  $\text{H}_2$  molecule; therefore, they

undergo no additional attenuation, either due to self-shielding or by scattering/absorption from dust. This on-the-spot approximation (or Case B) means the only attenuation we need to account for the production of the XUV radiation field is that due to the strength of the hard X-ray field at depth so that

$$f_{\text{att},XUV} \equiv B = \frac{S(\tau_X)}{\tau_X^{\phi+1}}. \quad (3.75)$$

The discussion below equation (3.42) details the properties of  $B$ .

Combining equations (3.70) and (3.75) leads to

$$\beta_{XUV} B \equiv 6 \times 10^{23} F_{0,H} \frac{F_{\text{LW,DS}}}{F_{0,DS}} \sigma_{\text{LW}} f_{X \rightarrow U} \frac{\sigma_X}{\gamma F_{\alpha X}} \frac{F_X}{R_d n_H} \frac{S(\tau_X)}{\tau_X^{\phi+1}} = \frac{D_{XUV}}{R_d n_H} \frac{S(\tau_X)}{\tau_X^{\phi+1}}. \quad (3.76)$$

Thus,  $\beta_{XUV} B$  represents the ratio of the free space  $\text{H}_2$  destruction rate from the internally generated LW band spectrum per hydrogen nucleus to the free space  $\text{H}_2$  formation rate attenuated by the HXR optical depth. With the use of constants in equations (3.69b) and (3.71),  $\beta_{XUV} B$  is

$$\beta_{XUV} B = k_{XUV} \frac{F_X}{R_d n_H} \frac{S(\tau_X)}{\tau_X^{\phi+1}}. \quad (3.77)$$

Using equations (3.74) and (3.75) puts  $\beta_{XUV}$  into the form

$$\beta_{XUV} B = 2.70 \times 10^6 \frac{F_X}{\tilde{\sigma}_d n_H} \frac{S(\tau_X)}{\tau_X^{\phi+1}}. \quad (3.78)$$

Again as in the HXR case, the terms that enter equation (3.78) as parameters are the free-space hard X-ray flux  $F_X \text{ erg cm}^{-2} \text{ s}^{-1}$ , the total hydrogen number density  $n_H \text{ cm}^{-3}$ , and the normalized dust grain cross section  $\tilde{\sigma}_d$ , attenuated by the HXR optical depth. The ratio of atomic-to-molecular hydrogen for a depth attenuated XUV radiation field can then be given as

$$\frac{n_{\text{H}^0}}{n_{\text{H}_2}} = \frac{1}{4} k_{XUV} \frac{F_X}{R_d n_H} \frac{S(\tau_X)}{\tau_X^{\phi+1}}, \quad (3.79a)$$

or equivalently,

$$\frac{n_{\text{H}^0}}{n_{\text{H}_2}} = \frac{1}{4} \beta_{XUV} B. \quad (3.79b)$$

As described below equation (3.59), the internally generated FUV radiation field is considered to

be isotropic in the forward direction accounting for the factor of 1/4 in the above two atomic-to-molecular hydrogen ratio equations.

### 3.4 Steady State HXR Field Creation - Destruction of Molecular Hydrogen including an XUV Field

We are now in a position to combine the steady-state creation-destruction equations for both the HXR only field and the XUV only field. This will give the effect of a beamed hard X-ray radiation field impinging onto an optically thick plane parallel semi-infinite molecular cloud slab with the addition of an isotropic LW band radiation field produced in the interior of the slab. Combining equations (3.1) and (3.59) for the HXR field and XUV field respectively, the steady state creation-destruction equation for molecular hydrogen becomes

$$R_d n_{H^0} n_H = \left\{ \frac{1}{2} D_{HXR} f_{att,X} + \frac{1}{4} D_{XUV} f_{att,X} \right\} n_{H_2} \quad [\text{cm}^{-3} \text{s}^{-1}]. \quad (3.80)$$

In terms of the ratio of atomic-to-molecular hydrogen densities this combined field becomes

$$\frac{n_{H^0}}{n_{H_2}} = \left\{ \frac{1}{2} D_{HXR} f_{att,X} + \frac{1}{4} D_{XUV} f_{att,X} \right\} \frac{1}{R_d n_H}. \quad (3.81)$$

For computational purposes and our analytic model developed in Chapter 4 we write this as

$$\frac{n_{H^0}}{n_{H_2}} = \frac{1}{2} \left\{ D_{HXR} f_{att,X} + \frac{1}{2} D_{XUV} f_{att,X} \right\} \frac{1}{R_d n_H}. \quad (3.82)$$

With use of equations (3.46a) and (3.79a), equation (3.82) can be given in terms of the constants describing the ratio of atomic-to-molecular hydrogen densities and using  $f_{att,X} \equiv f_{att,XUV}$

After inserting the constants defined earlier, this then becomes after simplification

$$\frac{n_{H^0}}{n_{H_2}} = \frac{1}{2} \left\{ k_I + \frac{1}{2} k_{DLW} \right\} k_H \frac{F_X}{R_d n_H} \frac{S(\tau_X)}{\tau_X^{\phi+1}}, \quad (3.83)$$

where the constants  $k_I = 1.94 \times 10^{11} \text{ erg}^{-1}$ ,  $k_{DLW} = 8.25 \times 10^{12} \text{ erg}^{-1}$ , and  $k_H = 9.81 \times 10^{-24} \text{ cm}^2$  are given by equations (3.37), (3.71), and (3.33) (or (3.69b)). The terms  $k_I$  and  $k_{XUV}$  represent

the number of dissociations per erg of deposited energy due to ionization from secondary electrons and from the internally generated FUV field respectively. The ratio of these constants, from FUV induced dissociation compared to direct ionization is

$$\frac{k_{DLW}}{2k_I} \simeq 21. \quad (3.84)$$

This result shows that the number of dissociations due to the Solomon process due to the internally generated FUV field is on the order of 20 times greater than that from direct ionizations. Combining the constants in equations (3.83) gives the new constant,  $k_X$

$$k_{XU} = k_I + \frac{1}{2} k_{DLW} = 4.32 \times 10^{12} \quad [\text{erg}^{-1}]. \quad (3.85)$$

The ratio of atomic-to-molecular hydrogen densities with this new constant is

$$\frac{n_{\text{H}^0}}{n_{\text{H}_2}} = \frac{1}{2} k_{XU} k_H \frac{F_X}{R_d n_{\text{H}}} \frac{S(\tau_X)}{\tau_X^{\phi+1}}. \quad (3.86)$$

Now, a constant that represents the cross section per unit energy is given as  $k_X$

$$k_X \equiv k_{XU} k_H = 4.24 \times 10^{-11} \quad [\text{cm}^2 \text{erg}^{-1}]. \quad (3.87)$$

Thus, the density ratio becomes

$$\frac{n_{\text{H}^0}}{n_{\text{H}_2}} = \frac{1}{2} k_X \frac{F_X}{R_d n_{\text{H}}} \frac{S(\tau_X)}{\tau_X^{\phi+1}}. \quad (3.88)$$

It can be seen from the above equation the net destruction rate per hydrogen nucleus for the combined HXR and XUV radiation fields is

$$\frac{D_X}{n_{\text{H}}} = k_X \frac{F_X}{n_{\text{H}}} = 4.24 \times 10^{-11} \frac{F_X}{n_{\text{H}}} \quad [\text{s}^{-1}]. \quad (3.89)$$

The atomic-to-molecular hydrogen ratio can be given in a simple form that is due to an HXR spectrum with an XUV radiation field. Using the dimensionless terms  $\beta_{\text{HXR}B}$  and  $\beta_{\text{XUV}B}$  that

are given in equations (3.43) and (3.76) respectively leads to

$$\frac{n_{\text{H}^0}}{n_{\text{H}_2}} = \frac{1}{2} \left\{ \beta_{\text{HXR}} + \frac{1}{2} \beta_{\text{XUV}} \right\} B. \quad (3.90)$$

The terms in brackets are combined into the new term  $\beta$

$$\beta \equiv \beta_{\text{HXR}} + \frac{1}{2} \beta_{\text{XUV}} = \frac{D_X}{R_d n_{\text{H}}} \quad (3.91)$$

which now represents the ratio of the unattenuated dissociation rate of  $\text{H}_2$  due to the dissociation of the combined effects of ionizations from secondary electrons and the dissociation from the Solomon process from secondary electron collisions,  $D_X$ , and its formation rate on grains,  $R_d$  per hydrogen nucleus. The attenuated ratio of the dissociation rate versus the formation rate per hydrogen nucleus is defined in terms of the dimensionless quantities  $\beta B$

$$\beta B \equiv k_X \frac{F_X}{R_d n_{\text{H}}} \frac{S(\tau_X)}{\tau_X^{\phi+1}} = \frac{D_X}{R_d n_{\text{H}}} \frac{S(\tau_X)}{\tau_X^{\phi+1}}, \quad (3.92)$$

or numerically as

$$\beta B = 4.24 \times 10^{-11} \frac{F_X}{R_d n_{\text{H}}} \frac{S(\tau_X)}{\tau_X^{\phi+1}}. \quad (3.93)$$

Thus,  $\beta B$  represents the ratio of the free space  $\text{H}_2$  destruction rate due to the HXR spectrum with an internally generated FUV field to the free space  $\text{H}_2$  formation rate per hydrogen nucleus attenuated by the HXR optical depth.

As the  $\text{H}_2$  formation rate on dust grains is proportional to the normalized dust grain cross section  $R_d = 3 \times 10^{-17} \tilde{\sigma}_d \text{ cm}^3 \text{ s}^{-1}$ , equation (3.93) becomes upon this substitution

$$\beta B = 1.41 \times 10^6 \frac{F_X}{\tilde{\sigma}_d n_{\text{H}}} \frac{S(\tau_X)}{\tau_X^{\phi+1}}. \quad (3.94)$$

The terms that enter equation (3.94) as parameters are the free-space hard X-ray flux  $F_X \text{ erg cm}^{-2} \text{ s}^{-1}$ , the total hydrogen number density  $n_{\text{H}} \text{ cm}^{-3}$ , and the normalized dust grain cross section  $\tilde{\sigma}_d$ .

The ratio of atomic-to-molecular hydrogen densities for the combined HXR and XUV fields is

finally given in a simple form in terms of dimensionless quantities as

$$\frac{n_{\text{H}^0}}{n_{\text{H}_2}} = \frac{1}{2}\beta B. \quad (3.95)$$

With this equation we now have the density profiles for atomic-to-molecular hydrogen from the total of the HXR spectrum and its induced FUV radiation field in a completely analogous form to the FUV only radiation field in a PDR, equation (2.108).

## Chapter 4

# Density Profiles and Transition Points

### 4.1 PDR Analytical Model

The basis for the analytical model of a PDR in this dissertation is one that has steady state, isothermal, non-turbulent conditions with a low ionization fraction ( $x_e \lesssim 10^{-3}$ ) for a beamed far-ultraviolet (11.2 - 13.6 eV) radiation field into an optically thick plane parallel slab. This PDR is modeled on that given by Sternberg & Bialy [2, 11, 16], the relevant details of which are given in § 2.2.

The point of interest is where there is a transition of the atomic-to-molecular hydrogen density profiles, from the region where atomic hydrogen dominates to the region where molecular hydrogen dominates under steady-state conditions, specifically the location where the atomic hydrogen number density equals the molecular hydrogen number density. In the PDR case this is given by equations (2.1) and (2.108) which is given here as,

$$\frac{n_{\text{H}^0}}{n_{\text{H}_2}} = \frac{1}{2} \frac{D_U}{R_d n_{\text{H}}} f_{\text{att},U} = \frac{1}{2} \alpha A. \quad (4.1)$$

Here the parameter  $\alpha A$  determines the ratio of the number density of  $\text{H}^0$  to  $\text{H}_2$ . As  $\alpha$  is proportional to the ratio of the free-space dissociation rate of  $\text{H}_2$  to its formation rate, an increase in  $\alpha$  leads to an increased ratio of  $n_{\text{H}^0}$  to  $n_{\text{H}_2}$ , thus atomic hydrogen is favored. The attenuation function  $A \leq 1$  is a continuously declining function at a column density of  $N_{\text{H}} \gtrsim 10^{14} \text{ cm}^2$  so that it begins to reduce the free-space dissociation rate, and as such a decrease in  $A$  results in a decrease in attenuation

so that  $n_{\text{H}^0}/n_{\text{H}_2}$  decreases and molecular hydrogen is favored. Using the conservation of hydrogen nuclei number density  $n_{\text{H}} \equiv n_{\text{H}^0} + 2n_{\text{H}_2}$ , equation (4.1) can be given in terms of the  $\text{H}^0$  and  $\text{H}_2$  fractions,  $n_{\text{H}^0}/n_{\text{H}}$  and  $n_{\text{H}_2}/n_{\text{H}}$  respectively. At the specific transition point under consideration, where the normalized number density of atomic hydrogen equals the normalized number density of molecular hydrogen (i.e.  $x_{\text{H}^0} = x_{\text{H}_2}$ ), equation (4.1) then becomes,

$$\frac{n_{\text{H}^0}}{n_{\text{H}}} \equiv x_{\text{H}^0} = \frac{0.25 \alpha A}{1 + 0.25 \alpha A}, \quad (4.2a)$$

$$\frac{2n_{\text{H}_2}}{n_{\text{H}}} \equiv 2x_{\text{H}_2} = \frac{1}{1 + 0.25 \alpha A}, \quad (4.2b)$$

for the respective  $\text{H}^0$  and  $\text{H}_2$  atomic nuclei fractions.

## 4.2 PDR Computational Results

The PDR was modeled with code written in Python 2.7.10 based on the equations and discussion given in §§ 2.2 and 4.1. The procedure involves solving equation (4.1) for  $n_{\text{H}^0}$  and  $n_{\text{H}_2}$ . There were 16 different variations of the parameters  $\alpha A$  and  $\tilde{\sigma}_d$ . The steady state density profiles for  $\text{H}^0$  and  $\text{H}_2$  are shown in Figure 4.2. At low column densities the gas is predominantly atomic hydrogen (cyan curve). This represents the face of the cloud and the radiation has not been significantly attenuated. In this regime the shielding function is  $A \lesssim 1$  and the ratio of atomic-to-molecular hydrogen density is  $n_{\text{H}}/n_{\text{H}_2} \rightarrow \frac{1}{2}\alpha$ . As the radiation gets attenuated as it traverses the cloud, the gas becomes increasingly molecular (magenta curve) due to attenuation as  $A \gtrsim 0$ . The transition point in Figure 4.2 is given by the black dot and represents an equal ratio of atomic and molecular hydrogen fractions such that,

$$\frac{n_{\text{H}^0}}{n_{\text{H}}} = \frac{2n_{\text{H}_2}}{n_{\text{H}}} \quad (4.3)$$

or equivalently

$$x_{\text{H}^0} = 2x_{\text{H}_2}, \quad (4.4)$$

from equations (4.2a) and (4.2b). With the use of the conservation of hydrogen nuclei number, equation (2.2) gives the transition point of interest as,

$$x_{\text{H}^0} \equiv 2x_{\text{H}_2} = 0.5. \quad (4.5)$$

#### 4.2.1 PDR density profiles and transition points for Bialy & Sternberg 2016

As a first step, a PDR model based on the five step analytical method given in [16] was used. This was to give the code a benchmark for the atomic-to-molecular hydrogen transition points (see Figure 4 of [16]). The density profiles from this procedure are shown in Figure 4.1 with the transition points where  $n_{\text{H}^0}/n_{\text{H}} = 2n_{\text{H}_2}/n_{\text{H}} = 0.5$  given in Table 4.1.

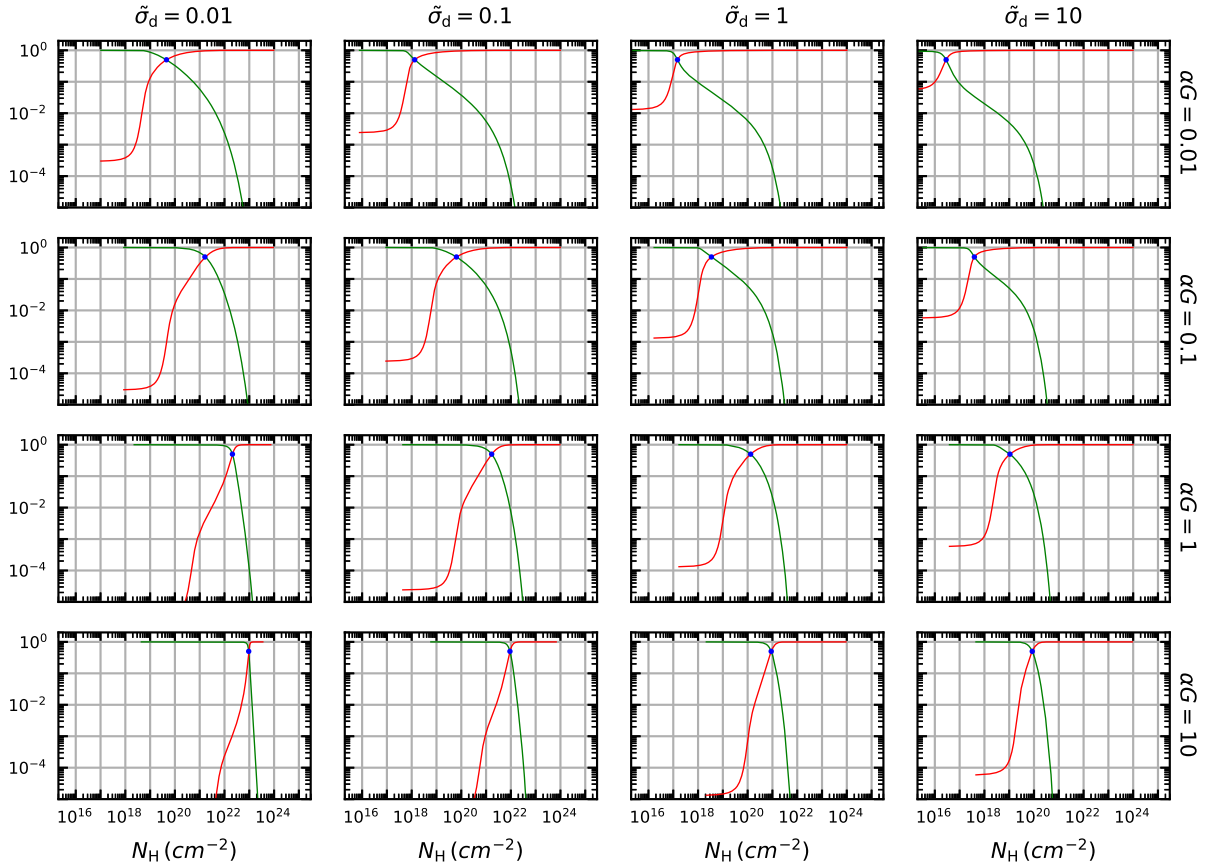


Figure 4.1: The  $\text{H}^0$  and  $\text{H}_2$  density profiles and transition points (blue dot) for  $n_{\text{H}^0}/n_{\text{H}}$  (green curve) and  $2n_{\text{H}_2}/n_{\text{H}}$  (red curve) with an FUV radiation field. This figure was created using the five step analytical procedure for generating depth-dependent atomic and molecular densities (see Bialy & Sternberg 2016).

Table 4.1: H<sup>0</sup>-to-H<sub>2</sub> FUV transition points  $N_{\text{H}}$  [cm<sup>2</sup>] for  $\alpha G$

$\alpha G$	$\tilde{\sigma}_d$			
	0.01	0.1	1	10
0.01	$4.56 \times 10^{19}$	$1.32 \times 10^{18}$	$1.48 \times 10^{17}$	$2.85 \times 10^{16}$
0.1	$1.62 \times 10^{21}$	$6.39 \times 10^{19}$	$3.46 \times 10^{18}$	$3.93 \times 10^{17}$
1	$2.09 \times 10^{22}$	$1.68 \times 10^{21}$	$1.32 \times 10^{20}$	$1.07 \times 10^{19}$
10	$9.46 \times 10^{22}$	$9.18 \times 10^{21}$	$8.90 \times 10^{20}$	$8.49 \times 10^{19}$

#### 4.2.2 PDR density profiles and transition points from computational model

The computational model used is given by equation (2.107), which differs from equation (22) in [16] in that the analytic form for attenuation explicitly uses the total column density  $N_{\text{H}}$  and isn't given solely by the parameter  $\tilde{\sigma}_d$ . This term is composed of the analytic form for self-shielding given in [12] and the dust attenuation term given in [2, 16].

A starting point for a given  $\alpha A$  was based on their parameterized  $\alpha G$ . The first step involved picking an  $\alpha G = 0.01, 0.1, 1, \text{ or } 10$ , and then determining  $\alpha$  using equations (2.109) and (2.111). This is calculated for each of the normalized grain cross-sections  $\tilde{\sigma}_d = 0.01, 0.1, 1, 10$ .

Since the molecular hydrogen formation rate coefficient is dependent only on the normalized dust grain cross section  $\tilde{\sigma}_d$  for a fixed gas temperature, only fixed ratios of  $I_U/n_{\text{H}}$  for a given  $\alpha$  are considered.

The goal of the code is to solve equation (4.1) for  $n_{\text{H}^0}$  and  $n_{\text{H}_2}$  as functions of the column density. Using,

$$n_{\text{H}^0} = dN_{\text{H}^0}/ds \quad \text{and} \quad n_{\text{H}_2} = dN_{\text{H}_2}/ds, \quad (4.6)$$

for semi-infinite slab geometry, where  $ds$  is the differential depth into the cloud, equation (4.1) can be integrated since  $A(N_{\text{H}_2}, N_{\text{H}})$  is a function of both the molecular hydrogen and total hydrogen column density. In this way and with the use of  $N_{\text{H}} = N_{\text{H}^0} + 2N_{\text{H}_2}$ , the number densities  $n_{\text{H}^0}$  and  $n_{\text{H}_2}$  can be solved for. The integration was done using the `scipy` package `odeint`. The density profiles from our computation are shown in Figure 4.2 with the transition points where  $n_{\text{H}^0}/n_{\text{H}} = 2n_{\text{H}_2}/n_{\text{H}} = 0.5$  given in Table 4.2.

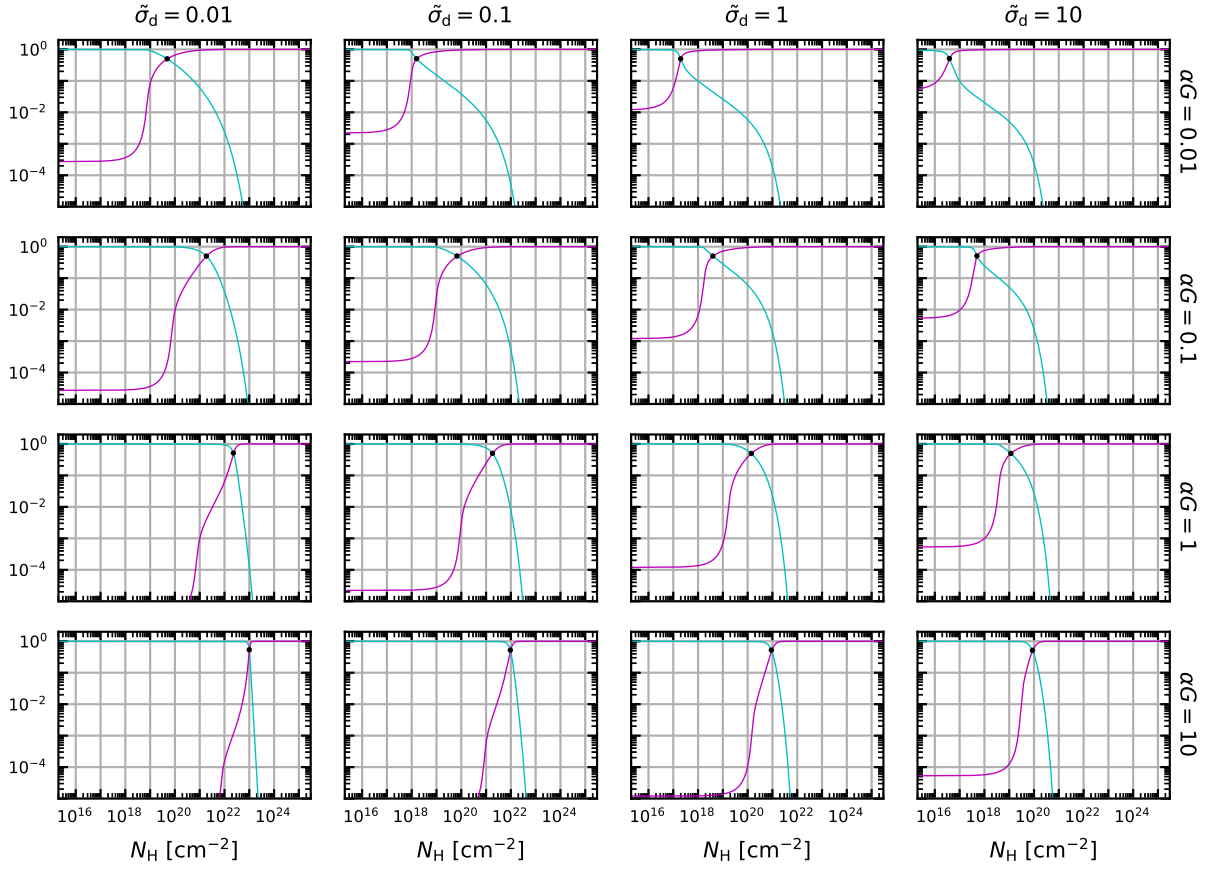


Figure 4.2: The  $\text{H}^0$  and  $\text{H}_2$  density profiles and transition points (black dot) for  $n_{\text{H}^0}/n_{\text{H}}$  (cyan curve) and  $2n_{\text{H}_2}/n_{\text{H}}$  (magenta curve) as functions of the total hydrogen column density  $N_{\text{H}}$  from an FUV radiation field for the computational model. The profiles and transition points are calculated using  $\alpha A$ . The right y-axis gives the  $\alpha G$  used. The transition points occur deeper into the cloud as the FUV strength increases (greater  $\alpha G$ ) or as dust attenuation decreases (smaller  $\tilde{\sigma}_{\text{d}}$ ).

Table 4.2: H<sup>0</sup>-to-H<sub>2</sub> FUV transition points  $N_{\text{H}}$  [cm<sup>2</sup>] calculating  $\alpha A$  for a given  $\alpha G$

$\alpha G$	$\tilde{\sigma}_{\text{d}}$			
	0.01	0.1	1	10
0.01	$4.91 \times 10^{19}$	$1.59 \times 10^{18}$	$1.98 \times 10^{17}$	$3.91 \times 10^{16}$
0.1	$1.87 \times 10^{21}$	$6.87 \times 10^{19}$	$3.98 \times 10^{18}$	$5.03 \times 10^{17}$
1	$2.31 \times 10^{22}$	$1.83 \times 10^{21}$	$1.41 \times 10^{20}$	$1.17 \times 10^{19}$
10	$1.01 \times 10^{23}$	$9.66 \times 10^{21}$	$9.29 \times 10^{20}$	$8.79 \times 10^{19}$

The analytic ( $\alpha G$ ) and computational ( $\alpha A$ ) models are superimposed from Figures 4.1 and 4.2 to show a comparison of the density profiles and transition points. This is given in Figure 4.3. It can be seen from the plots that there is excellent agreement between the two models. The transition point for the computational model for all 16 plots occurs slightly deeper into the cloud than the analytic model. The approximate percentage increase in total hydrogen column density that the transition point occurs is given in Table 4.3.

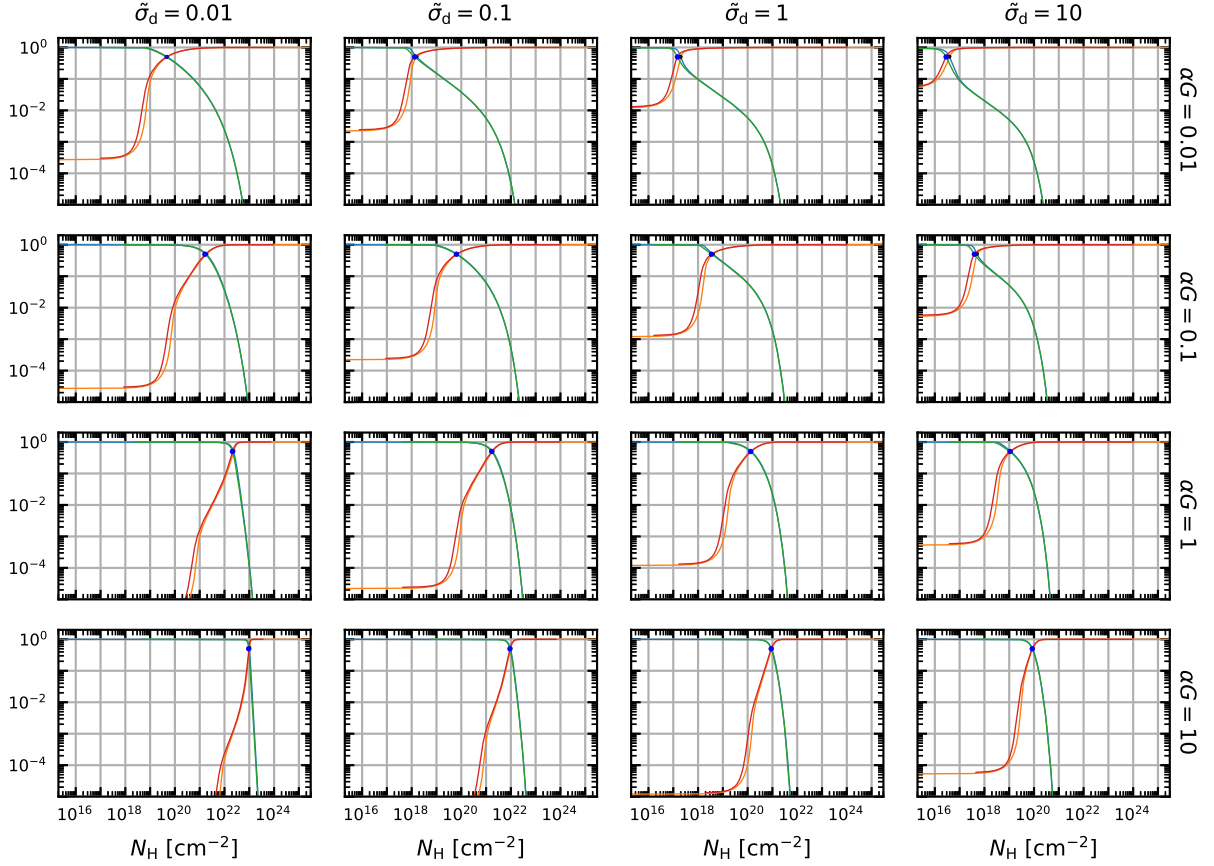


Figure 4.3: Superposition of the analytic and computational models for  $\text{H}^0$  and  $\text{H}_2$  density profiles and transition points (blue dot - analytic; black dot - computational) for  $n_{\text{H}^0}/n_{\text{H}}$  (green curve - analytic; cyan curve - computational) and  $2n_{\text{H}_2}/n_{\text{H}}$  (red curve - analytic; magenta curve - computational) as functions of the total hydrogen column density  $N_{\text{H}}$  from an FUV radiation field.

Table 4.3: Percentage increase in column density of transition point - Computational ( $\alpha A$ ) vs. Analytical ( $\alpha G$ )

$\alpha G$	$\tilde{\sigma}_d$			
	0.01	0.1	1	10
0.01	$\sim 8$	$\sim 20$	$\sim 34$	$\sim 37$
0.1	$\sim 15$	$\sim 8$	$\sim 15$	$\sim 28$
1	$\sim 11$	$\sim 9$	$\sim 7$	$\sim 9$
10	$\sim 7$	$\sim 5$	$\sim 4$	$\sim 4$

### 4.3 Analytic response of the PDR transition points to HXR field

For the response of the transition points of the far-ultraviolet only radiation field to a hard X-ray spectrum, we consider a combination of the steady state PDR with the inclusion of the steady state XDR model. The atomic-to-molecular hydrogen ratio  $n_{\text{H}}/n_{\text{H}_2}$  is now a function of both a steady-state attenuated PDR given by  $\frac{1}{2}\alpha A$  and a steady-state attenuated XDR given by  $\frac{1}{2}\beta B$  from equations (2.108) and (3.95) respectively. The energy flux of the hard X-rays that causes the response at the new transition point can then be determined.

This combination leads to the simple expression

$$\frac{n_{\text{H}^0}}{n_{\text{H}_2}} = \frac{1}{2}\delta, \quad (4.7)$$

where

$$\delta = \alpha A + \beta B. \quad (4.8)$$

The ratio of number densities of atomic hydrogen to total hydrogen and also the ratio of number densities of molecular hydrogen to total hydrogen can be given for  $\delta$  in a similar manner to equations (4.2a) and (4.2b) as

$$x_{\text{H}^0} = \frac{0.25\delta}{1 + 0.25\delta}, \quad (4.9a)$$

$$2x_{\text{H}_2} = \frac{1}{1 + 0.25\delta}, \quad (4.9b)$$

where  $x_{\text{H}^0} \equiv n_{\text{H}^0}/n_{\text{H}}$  and  $x_{\text{H}_2} \equiv n_{\text{H}_2}/n_{\text{H}}$  for the respective  $\text{H}^0$  and  $\text{H}_2$  fractions respectively.

For a given value of delta, which represents the atomic-to-molecular hydrogen ratio, the contribution due to attenuated HXR's then ranges from

$$0 \leq \beta B \leq \delta. \quad (4.10)$$

When the flux from the HXR radiation field is negligible in regards to creating a response in the PDR,  $\beta B \rightarrow 0$  and  $\alpha A \rightarrow \delta$ . As greater fluxes of X-rays are considered,  $\beta B$  starts making a contribution to  $\delta$ . When the HXR flux increases further, the contribution due to the FUV radiation field becomes less significant, and as such  $\alpha A \rightarrow 0$ , which leads to  $\beta B \rightarrow \delta$ .

## 4.4 Computational response of the PDR transition points to HXR field

This section compares the response of the PDR only transition point to two forms of the HXR energy deposition. The first is the exact analytic form with a hyperbolic approximation representing  $S(\tau_X)$  in § 4.4.1. The second ignores the  $S(\tau_X)$  term and only takes into account the  $\tau_X^{-\phi-1}$  attenuation function in § 4.4.2.

### 4.4.1 $H_X \propto S(\tau_X)\tau_X^{-\phi-1}$

The calculation of the response of the transition point of the PDR to a HXR field follows the same procedure as that done in § 4.2.2. The code now solves equation (4.7) for  $n_{\text{H}^0}$  and  $n_{\text{H}_2}$  from which the number density ratios given in equations (4.9a) and (4.9b) can be found. This was done for each of the normalized grain cross-sections  $\bar{\sigma}_d = 0.01, 0.1, 1, 10$  that we considered.

The same values of  $\alpha G = 0.01, 0.1, 1, \text{ or } 10$  were used to determine  $\alpha$  with the FUV shielding function  $A(N_{\text{H}_2}, N_{\text{H}})$  being used in place of  $G$ . The attenuated energy deposition rate of the HXR spectrum  $B$  is given by the hyperbolic function in equation (B.4). This replaces the analytic form of the HXR energy deposition rate attenuation given in (3.12).

The location of the transition point in terms of  $N_{\text{H}}$  can be seen in Figure 4.4. From this the amount of HXR energy flux per hydrogen nuclei needed to cause this response can be determined.

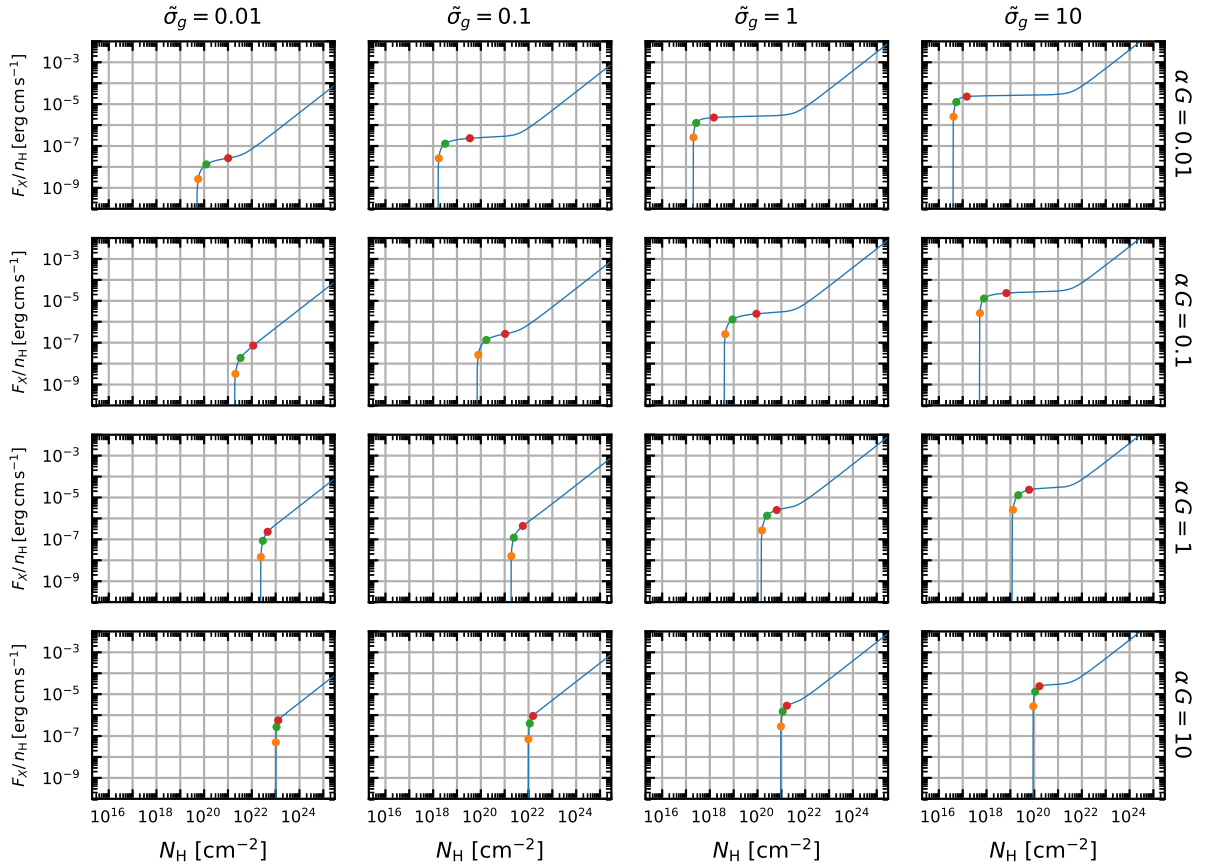


Figure 4.4: The transition point curve where  $x_{\text{H}^0} = 2x_{\text{H}_2}$  for the response of a PDR to an HXR field with  $S(\tau_X)\tau^{-\phi-1}$  attenuation. The vertical portion of the curve represents the FUV only transition point. The contribution of  $\beta B$  as a percentage of  $\delta$  to the column density of the transition point is shown at 10% (orange dot), 50% (green dot), and 90% (red dot).

As is noted in § Appendix B significant attenuation of the HXR flux doesn't occur until  $N_{\text{H}} \approx 10^{20} \text{ cm}^{-2}$ . When the transition point due to the FUV only field occurs less than this column density there is a regime where there is no further significant attenuation of the HXR field until  $N_{\text{H}} \approx 10^{20} \text{ cm}^{-2}$ . This is represented by the horizontal portion of the curve. Once the HXR flux is great enough for the transition point to occur after  $10^{20} \text{ cm}^{-2}$ , whether or not the FUV only transition point occurs before or after this point, an increasing flux causes a linear increase in the transition point on a log-log scale. This represents the energy deposition rate being  $H_X \propto \tau_X^{-\phi-1}$ .

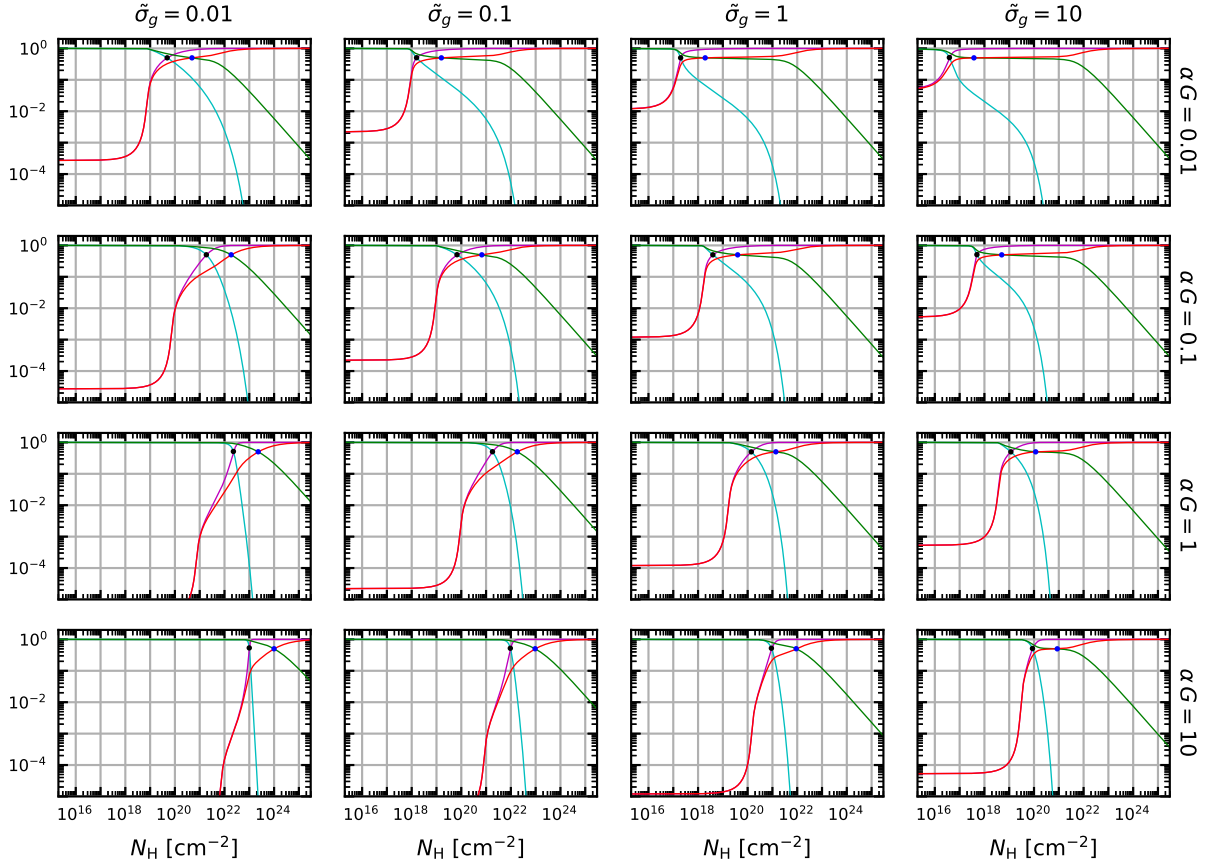


Figure 4.5: The  $\text{H}^0$  and  $\text{H}_2$  density profiles and transition points for  $x_{\text{H}^0}$  and  $2x_{\text{H}_2}$  of an FUV only flux superimposed with an HXR flux  $S(\tau_X)\tau^{-\phi-1}$  attenuation that causes a response in the PDR transition point by one order of magnitude.

Table 4.4: HXR energy flux  $F_X/n_{\text{H}} [\text{erg cm s}^{-1}]$  at the  $\text{H}^0$ -to- $\text{H}_2$  combined FUV-HXR transition points at one order of magnitude increase in  $N_{\text{H}}$  column density for  $S(\tau_X)\tau^{-\phi-1}$  attenuation.

$\alpha G$	$\tilde{\sigma}_{\text{d}}$			
	0.01	0.1	1	10
0.01	$2.27 \times 10^{-8}$	$2.16 \times 10^{-7}$	$2.34 \times 10^{-6}$	$2.44 \times 10^{-5}$
0.1	$1.14 \times 10^{-7}$	$2.39 \times 10^{-7}$	$2.15 \times 10^{-6}$	$2.28 \times 10^{-5}$
1	$1.05 \times 10^{-6}$	$1.17 \times 10^{-6}$	$3.01 \times 10^{-6}$	$2.62 \times 10^{-5}$
10	$3.9 \times 10^{-6}$	$4.89 \times 10^{-6}$	$6.86 \times 10^{-6}$	$2.91 \times 10^{-5}$

Table 4.5: HXR energy flux  $F_X/n_H$  [erg cm s<sup>-1</sup>] at the H<sup>0</sup>-to-H<sub>2</sub> combined FUV-HXR transition points at one order of magnitude increase in  $N_H$  column density for  $\tau^{-\phi-1}$  attenuation.

$\alpha G$	$\tilde{\sigma}_d$			
	0.01	0.1	1	10
0.01	$3.50 \times 10^{-9}$	$1.72 \times 10^{-9}$	$3.03 \times 10^{-9}$	$7.58 \times 10^{-9}$
0.1	$1.10 \times 10^{-7}$	$4.90 \times 10^{-8}$	$3.83 \times 10^{-8}$	$6.68 \times 10^{-8}$
1	$1.07 \times 10^{-6}$	$1.13 \times 10^{-6}$	$1.14 \times 10^{-6}$	$1.23 \times 10^{-6}$
10	$3.96 \times 10^{-6}$	$4.95 \times 10^{-6}$	$6.19 \times 10^{-6}$	$7.64 \times 10^{-6}$

#### 4.4.2 $H_X \propto \tau_X^{-\phi-1}$

This section considers HXR attenuation due to the opacity term  $\tau_X^{-\phi-1}$ . This calculation is performed using a modification of equation (3.41) which is given as

$$\beta_{HXR}B = 6.35 \times 10^4 \frac{F_X}{\tilde{\sigma}_d n_H} \frac{1}{\tau_X^{\phi+1}}, \quad (4.11)$$

where  $B \equiv \tau_X^{-\phi-1}$ . The procedure follows the same methodology as that done in § 4.4.

The location of the transition point with this modified attenuation is shown in Figure 4.6 with values of the HXR energy flux required to shift the FUV only transition point by one order of magnitude given in Table 4.5.

These curves have a similar form across the range of column densities considered as the attenuation of the HXR spectrum is now a linearly declining function on a log-log scale. The elimination of the  $S(\tau_X)$  term removes the inability of the HXR spectrum to have any significant energy deposition at column densities of less than  $N_H \approx 10^{20}$  cm<sup>-2</sup>.

A comparison of the two forms of HXR attenuation function considered shows that for transition points from the FUV only model that occur  $N_H \lesssim 10^{20}$  cm<sup>-2</sup>, there is no significant difference in the model used. As the FUV only attenuation curve occurs at smaller column densities, the difference between the two attenuation curves gets more pronounced.

As can be seen in Figure (4.8), when  $\tilde{\sigma}_d \gtrsim 10 \times \alpha G$  the response of the transition point by one order of magnitude due to the HXR attenuation function  $\tau^{-\phi-1}$  deviates from the  $S(\tau_X)\tau^{-\phi-1}$  attenuation function by one or more orders of magnitude. As this discrepancy grows, the simplified

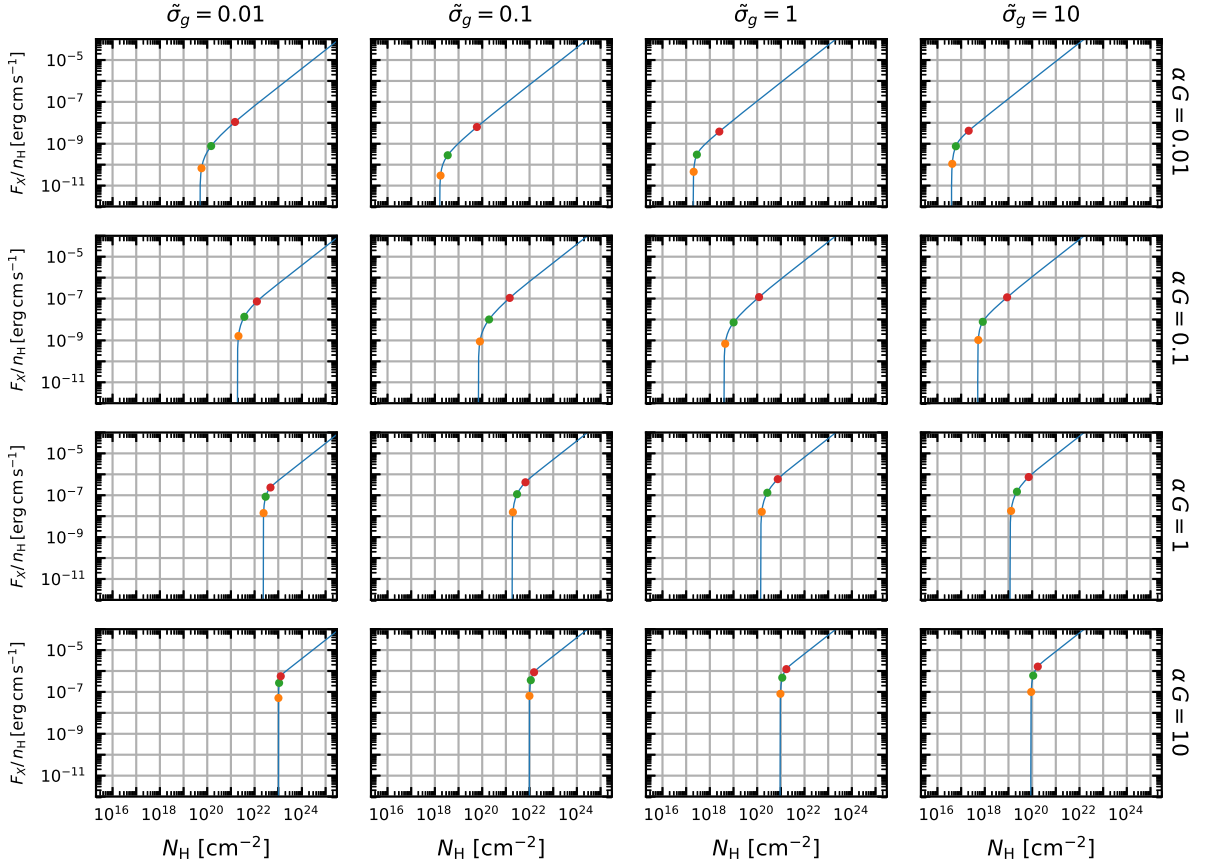


Figure 4.6: The transition point curve where  $x_{\text{H}^0} = 2x_{\text{H}_2}$  for the response of a PDR to an HXR field with  $\tau^{-\phi-1}$  attenuation. The vertical portion of the curve represents the FUV only transition point. The contribution of  $\beta B$  as a percentage of  $\delta$  to the column density of the transition point is shown at 10% (orange dot), 50% (green dot), and 90% (red dot).

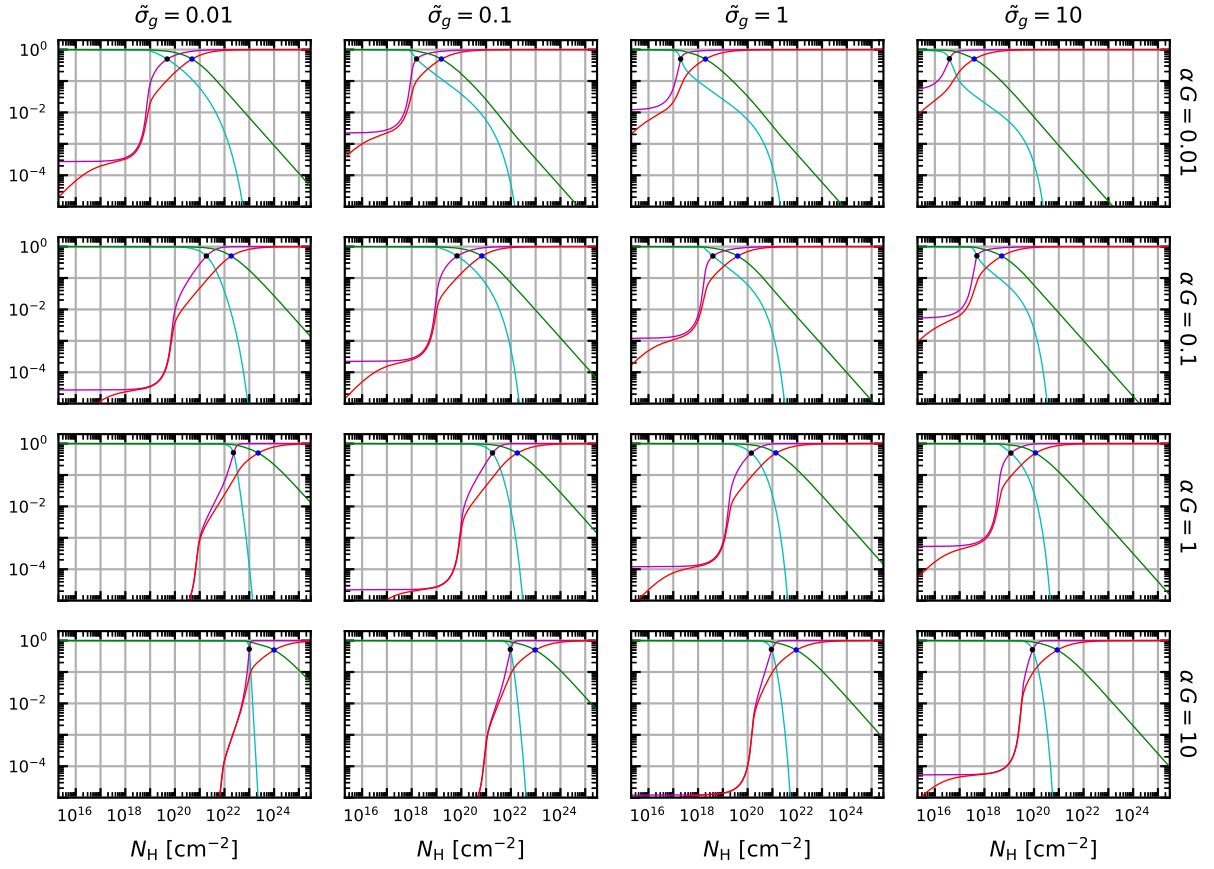


Figure 4.7: The  $\text{H}^0$  and  $\text{H}_2$  density profiles and transition points for  $x_{\text{H}^0}$  and  $2x_{\text{H}_2}$  of an FUV only flux superimposed with an HXR flux  $\tau^{-\phi-1}$  attenuation that causes a response in the PDR transition point by one order of magnitude.

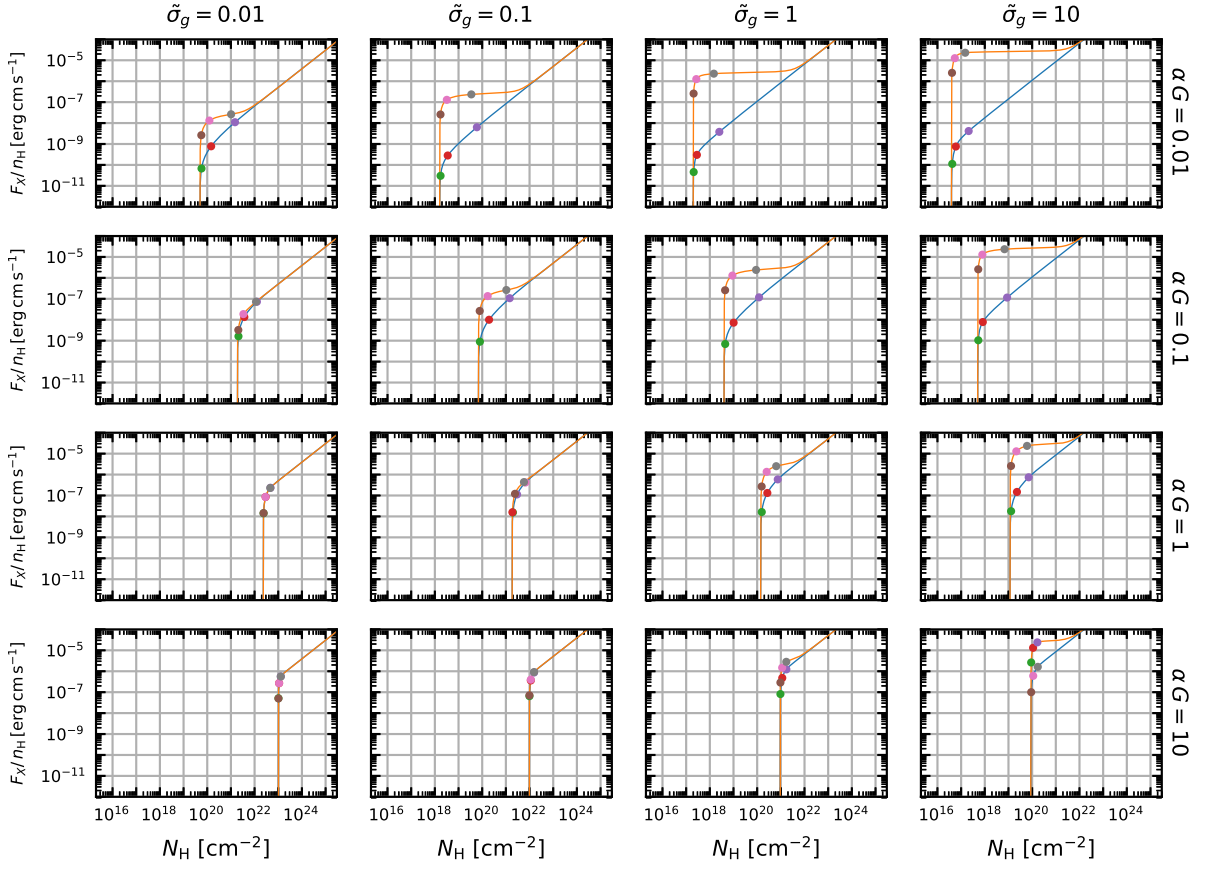


Figure 4.8: Comparison of the response for the attenuation functions  $S(\tau_X)\tau^{-\phi-1}$  and  $\tau^{-\phi-1}$

model becomes less accurate as Table 4.6 shows.

Conversely, when  $\alpha G \gtrsim \tilde{\sigma}_d$ , the two HXR attenuation curves vary by less than one order of magnitude. In the cases where  $\alpha G \gtrsim 10 \times \tilde{\sigma}_d$ , then  $\tau^{-\phi-1} \approx S(\tau_X)\tau^{-\phi-1}$  in terms of the response at one order of magnitude.

Table 4.6: Ratio of the HXR energy flux  $F_X/n_H$  [erg cm s<sup>-1</sup>] at one order of magnitude increase in  $N_H$  column density for  $\tau^{-\phi-1}$  vs.  $S(\tau_X)\tau^{-\phi-1}$ .

$\alpha G$	$\tilde{\sigma}_d$			
	0.01	0.1	1	10
0.01	$1.54 \times 10^{-1}$	$7.97 \times 10^{-3}$	$1.29 \times 10^{-3}$	$3.11 \times 10^{-4}$
0.1	$9.60 \times 10^{-1}$	$2.05 \times 10^{-1}$	$1.78 \times 10^{-2}$	$2.93 \times 10^{-3}$
1	$1.02 \times 10^0$	$9.64 \times 10^{-1}$	$3.79 \times 10^{-1}$	$4.71 \times 10^{-2}$
10	$1.02 \times 10^0$	$1.01 \times 10^0$	$9.03 \times 10^{-1}$	$2.63 \times 10^{-1}$

#### 4.5 Analytic Fit for $H_X \propto \tau_X^{-\phi-1}$

In this section we present an analytic model that estimates the behavior of the transition point curve over the range of hard X-ray fluxes per hydrogen nucleus versus total hydrogen column density for the given values of  $\alpha G$  and  $\tilde{\sigma}_d$  that we have considered in this paper. For this analytic model we required that it took into account the limiting conditions when the amount of attenuated HXR flux per nucleus was low ( $\beta B \gtrsim 0$ ) and when the attenuated HXR flux per nucleus was high ( $\beta B \lesssim \delta$ ). In the first case, the transition point of the curve  $N_{H,\text{trans}}$ , approaches that of the FUV only transition point  $N_{H,\text{trans}} \rightarrow N_{H,\text{FUV}}$ . In the second case, the transition point of the curve  $N_{H,\text{trans}}$ , approaches that of the HXR including XUV only transition point  $N_{H,\text{trans}} \rightarrow N_{H,\text{XUV}}$ .

The analytic expression used for this fit is given by,

$$N_{H,\text{trans}} = (N_{H,\text{FUV}}^{\phi+1} + N_{H,\text{HXR}}^{\phi+1})^{1/(\phi+1)}, \quad (4.12)$$

where  $\phi + 1$  is the same term that describes the behavior of the attenuation function  $B$  of the HXR energy deposition rate  $H_X \propto \tau_X^{-\phi-1}$ . This analytic fit is shown superimposed with our computational models in Figure 4.9. A range of values varying by  $\pm 0.2$  dex are shown about the analytic line.

The analytic fit does a good job when the attenuated FUV radiation field per hydrogen nucleus is low  $\alpha G \lesssim 1$  and the transition point is gradual between  $\alpha G$  and  $\beta B$ . This is shown for the values of  $\alpha G = 0.01, 0.1, \text{ and } 1$ . For the higher attenuated FUV radiation field per hydrogen nucleus that we consider,  $\alpha G = 10$ , the transition between  $\alpha G$  and  $\beta B$  becomes sharp and our analytic fit

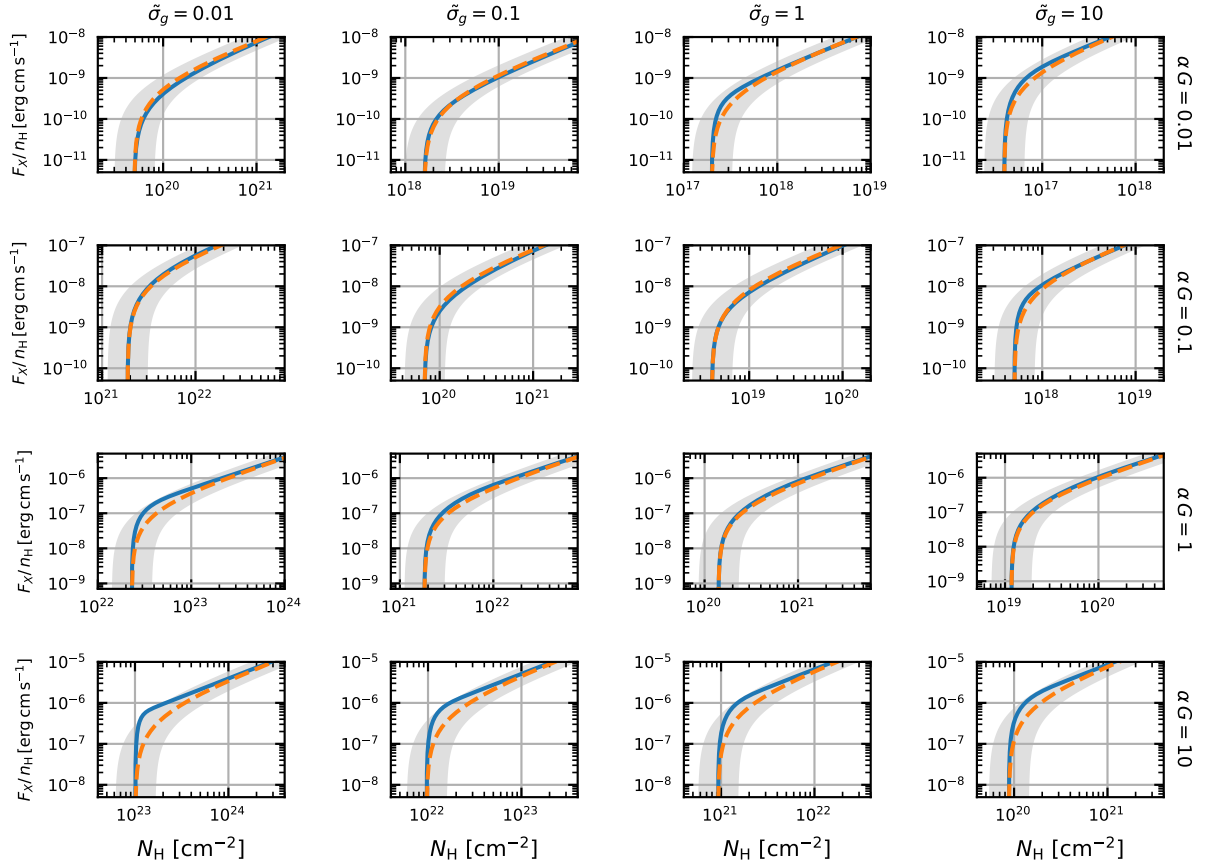


Figure 4.9: The transition point curves for the response of a PDR to an HXR field with  $\tau^{-\phi-1}$  (solid blue line) superimposed with the analytic model (orange dashed line). A variation of  $\pm 0.2$  dex is shown around the analytic fit line (light grey strip).

becomes less accurate at modeling the perturbation point.

The 16 images in Figure 4.9 are shown individually in Figures C.1 - C.16 in Appendix C.

# Chapter 5

## Conclusions

In this dissertation, a simple model is presented that shows the response of the atomic-to-molecular hydrogen transition point in a far-ultraviolet (FUV) only photodissociation region due to the contribution from a hard X-ray (HXR) spectrum over the 1 - 100 keV energy range.

This model is a blend of two existing models of steady state regions, that of a photodissociation region (PDR) [2][16] and that of an X-ray dissociation region (XDR) [3].

The PDR model of [2][16] was used as benchmark in order to determine what the transition points would be for the model developed in this dissertation to be compared against. The transition points where  $n_{\text{H}^0}/2n_{\text{H}_2} = 0.5$  were first found using the analytic model of [16] for a given  $\alpha G$  and  $\tilde{\sigma}_d$ . This was done as the dust-limited self-shielding function  $G$  is given as an analytic fit that is parameterized by the normalized dust-grain cross section  $\tilde{\sigma}_d$  only [16]. In the model developed in this dissertation the dust-limited self-shielding function is denoted by  $A(N_{\text{H}}N_{\text{H}_2})$  which is composed of the optical depth parameterized by  $\tilde{\sigma}_d$  and also by the self-shielding function of [12] (their equation (37)). Our model replaced the parameterized equation (2.109) with the dust-limited self-shielding function, equation (2.104). Thus we use  $\alpha A$  in the code in order to determine the column densities but  $\alpha A$  is being plotted within the  $\alpha G$  values. From this the normalized number densities,  $x_{\text{H}^0}$  and  $2x_{\text{H}_2}$  were found and density profiles plotted and compared to the transition points of [16]. This modification led to a small increase in the PDR only transition point from that ranged from between 4 and 37%.

For the response of the transition points due to the inclusion of an HXR, two forms of the energy deposition function  $H_X$  were used. The first form used the analytic form of the function

$S(\tau_X)\tau_X^{-\phi-1}$ , where for computational efficiency, we found a hyperbolic fit to this given in equation (B.4). Recall that  $\phi \equiv (\alpha_X - 1)/\gamma$  where  $\alpha_X$  is the spectral index of the HXR SED and  $\gamma$  is the energy dependence index for HXR interactions and note that  $S(\tau_X)$  is parameterized by  $\phi$ . When the transition point of the PDR occurs at column densities less than  $N_H \lesssim 10^{20} \text{ cm}^{-2}$  there is a shoulder region where X-ray attenuation decreases significantly until a column density of  $N_H \lesssim 10^{21} \text{ cm}^{-2}$  is reached. Under this form of the energy deposition function it is seen that the variation in HXR flux at the transition point doesn't show much variation within a given  $\tilde{\sigma}_d$ . When  $\tilde{\sigma}_d = 10$ , the HXR flux at the transition point is  $F_X/n_H \sim 10^{-5} \text{ erg cm s}^{-1}$  across the range  $\alpha G = 0.01 - 10$ . For  $\tilde{\sigma}_d = 1$ , this becomes  $F_X/n_H \sim 10^{-6} \text{ erg cm s}^{-1}$  across the range  $\alpha G = 0.01 - 10$ . This same pattern occurs for  $\tilde{\sigma}_d = 0.1$ , where  $F_X/n_H \sim 10^{-7} \text{ erg cm s}^{-1}$  across the range  $\alpha G = 0.01 - 10$ . Some variation to this shows up for  $\tilde{\sigma}_d = 0.01$  where  $F_X/n_H \sim 10^{-8} \rightarrow 10^{-6} \text{ erg cm s}^{-1}$  as  $\alpha G = 0.01 \rightarrow 10$ . These  $F_X/n_H$  values are taken where  $\alpha A \approx \beta B$ . In regions where the attenuated FUV is lower,  $\alpha G = 0.01 - 0.1$ , the transition point of the PDR occurs at hydrogen column densities less than  $N_H \lesssim 10^{20} \text{ cm}^{-2}$  and there is approximately a one magnitude increase in the HXR flux required to cause a response in the transition point per magnitude increase in the metallicity. For  $\alpha G = 0.01$ ,  $F_X/n_H$  ranges from  $\sim 10^{-9}$  to  $\sim 10^{-5}$  as  $\tilde{\sigma}_d = 0.01 \rightarrow 10$ . This is due to the formation rate of  $\text{H}_2$  being dependent on the normalized grain cross section. This effect decreases as  $\alpha G \rightarrow 1 - 10$  as the transition point from the PDR starts to occur at column densities that would attenuate the HXR only field. As a comparison, an HXR only transition point occurs at an energy flux per hydrogen nucleus of  $F_X/n_H \sim 10^{-4} \text{ erg cm s}^{-1}$  [3]. Thus the flux per hydrogen nucleus is on the order of 1 to 4 orders of magnitude less to cause a response in the transition point.

A simplifying modification to the energy deposition function was made by ignoring the  $S(\tau_X)$  term. By doing this, in regimes where the transition point occurs at lower column densities than where HXR attenuation would typically begin, i.e.  $N_H \lesssim 10^{20}$ , a deviation in the amount of HXR flux per hydrogen nucleus required for a response occurs. This difference becomes more pronounced as the PDR only transition point decreases and these ratios are given in Table 4.6. Under this approximation there is essentially no variation in the HXR flux across  $\tilde{\sigma}_d$  for a given  $\alpha G$ . For each magnitude increase in  $\alpha G$ , approximately one magnitude more of HXR flux per hydrogen nucleus is required for a transition point response. This can be seen in Figure 4.4. For  $\alpha G = 0.01, 0.1, 1, 10$  the amount of HXR energy flux per hydrogen nucleus at  $\alpha A \approx \beta B$  is  $F_X/n_H \sim 10^{-9}, 10^{-8}, 10^{-7}, 10^{-7}$

erg cm s<sup>-1</sup> respectively.

In order to make a simple analytic fit to the behavior of the response curve, we used the form of the energy deposition function  $\tau_X^{-\phi-1}$ . For FUV only transition points occurring at  $N_H \gtrsim 10^{19}$  cm<sup>-2</sup>, the response at a one order magnitude increase in the column density of the transition point due to an HXR flux is within one order of magnitude from the response to the  $S(\tau_X)\tau_X^{-\phi-1}$  function. This can be seen in Figure 4.8 and in Table 4.6. The analytic fit we derived for the response of the PDR due to the HXR flux from  $H_X \propto \tau_X^{-\phi-1}$  was given in equation (4.12). The computational curve showing the response compared to the analytic fit was with  $\pm 0.2$  dex across the parameter space of our simulations, except for the  $\tilde{\sigma}_d = 0.01$  and  $\alpha G = 10$  plot. The higher H<sub>2</sub> dissociation rate from the FUV field compared to the low formation rate caused a sharp response in the PDR that caused it to curve more rapidly than in the other scenarios. The  $\alpha G = 10$  plots however all had a more rapid response to the HXR field compared to the other  $\alpha G$  values considered.

Future work on this project could be to develop an analytic fit for the  $S(\tau_X)\tau_X^{-\phi-1}$  model, to examine the effect of metallicity on the HXR radiation field as well as the effect of attenuation of the HXR field due to dust, and finally to use photoionization codes such as Cloudy or Meudon PDR to investigate the transition points of these combined fields.

# Appendix A

## Far-Ultraviolet Spectral Distributions

This appendix describes some of the different forms of a Draine FUV spectrum [7], and the units and conversions (which aren't always obvious) that are found in various papers. Some of the distributions found in the literature are given in terms of energy density [ $\text{ergs cm}^{-3}$ ], or as specific intensities such as photon flux per unit energy [ $\text{photons cm}^{-2} \text{s}^{-1} \text{eV}^{-1}$ ], photon flux per unit frequency [ $\text{photons cm}^{-2} \text{s}^{-1} \text{Hz}^{-1}$ ], energy flux per unit wavelength [ $\text{photons cm}^{-2} \text{s}^{-1} \text{\AA}^{-1}$ ] and so on. These distributions may or may not be given in terms of per solid angle  $(4\pi)^{-1}$  [ $\text{sr}^{-1}$ ] or integrated over all space (full  $4\pi$ ).

In the examples given below, we shall denote the spectral distributions with the following notation: energy density,  $u_\rho$  [ $\text{erg cm}^{-3}$ ]; energy flux,  $f_\rho$  [ $\text{erg cm}^{-2} \text{s}^{-1}$ ]; photon density,  $p_\rho$  [ $\text{photon cm}^{-3}$ ]; and photon flux,  $q_\rho$  [ $\text{photon cm}^{-2} \text{s}^{-1}$ ]. Further, a subscript will denote if the distribution is dependent on the wavelength, frequency, or energy with the symbols  $\lambda$ ,  $\nu$ , and  $E$  respectively. If the distribution and its differential are given in terms of cgs units, then the conversion between the terms above is a relatively straightforward procedure. In some of the distributions given in the references, care must be taken upon calculation as the distribution and its differential could be cast in different units or physical constants may be in cgs units, have wavelengths in  $\text{\AA}$  or have energy units in eV mixed together. We shall show those conversions explicitly in the examples given below as well as convert all of the FUV spectral distributions to have wavelength dependencies in  $\text{\AA}$ .

## A.1 The Habing SED

A fit to the Habing field [6] was given by Draine & Bertoldi [12]

$$u_\lambda = \lambda u_{\rho_\lambda} \equiv \left( -\frac{25}{6} \lambda_3^3 + \frac{25}{2} \lambda_3^2 - \frac{13}{3} \lambda_3 \right) \times 10^{-14} \quad [\text{erg cm}^{-3}], \quad (\text{A.1})$$

where  $\lambda_3 \equiv \lambda/10^3 \text{ \AA}$ . This wavelength specific energy density is defined in terms of wavelength given in units of  $\text{\AA}$  and it has been integrated over all space. This wavelength specific energy density distribution can then be defined by

$$u_{\rho_\lambda} \equiv \frac{du_\lambda}{d\lambda d\Omega} \quad [\text{erg cm}^{-3} \text{ \AA}^{-1} \text{ sr}^{-1}]. \quad (\text{A.2})$$

In terms of equation (A.1) then this becomes

$$u_{\rho_\lambda} = \frac{1}{4\pi} \left( -\frac{25}{6 \times 10^9} \lambda^2 + \frac{25}{2 \times 10^6} \lambda - \frac{13}{3 \times 10^3} \right) \times 10^{-14} \quad [\text{erg cm}^{-3} \text{ \AA}^{-1} \text{ sr}^{-1}]. \quad (\text{A.3})$$

The  $1/4\pi$  term is required for the distribution since equation (A.1) has already been integrated over all space and also it is given in terms of wavelength units of  $\text{\AA}^{-1}$  as the function is defined in those units.

To convert the wavelength specific energy density distribution to a frequency specific energy density distribution, then the conversion  $u_{\rho_\lambda} d\lambda = u_{\rho_\nu} d\nu$  needs to be performed. Using the substitutions  $\lambda = c/\nu$  and  $d\lambda/d\nu = |c/\nu^2|$  casts equation equation (A.3) into the form

$$u_{\rho_\nu} = \frac{1}{4\pi} \left( -\frac{25}{6 \times 10^9} \frac{c_a^3}{\nu^4} + \frac{25}{2 \times 10^6} \frac{c_a^2}{\nu^3} - \frac{13}{3 \times 10^3} \frac{c_a}{\nu^2} \right) \times 10^{-14} \quad [\text{erg cm}^{-3} \text{ Hz}^{-1} \text{ sr}^{-1}]. \quad (\text{A.4})$$

The sign change that is ignored in the absolute value term above is only required in order to flip the limits of integration, if (A.3) is being used within a definite integral, as the wavelength and frequency are inversely related. Care must be taken when using equation (A.4) that the speed of light is given in angstroms which we denote by  $c_a = 2.998 \times 10^{18} \text{ \AA s}^{-1}$ . If the speed of light required is needed in cgs units, then it will be denoted by  $c = 2.998 \times 10^{10} \text{ cm s}^{-1}$ . Similar conversions as those given above equation (A.4) are required when changing between wavelength, frequency and energy. In those other cases, the units that are being used must be examined for the correct

conversions.

In § A.1 we will use the wavelength specific intensity energy density distribution as the basis for the conversions to other quantities of interest.

As given in equation (A.1) the energy density is given by multiplying the wavelength specific energy density by the wavelength,

$$u_\lambda = \lambda u_{\rho_\lambda} \quad [\text{erg cm}^{-3} \text{ sr}^{-1}]. \quad (\text{A.5})$$

From this the energy flux can be found,

$$f_\lambda = c\lambda u_{\rho_\lambda} \quad [\text{erg cm}^{-2} \text{ s}^{-1} \text{ sr}^{-1}], \quad (\text{A.6})$$

the photon density,

$$p_\lambda = \frac{\lambda^2 u_{\rho_\lambda}}{hc_a} \quad [\text{photon cm}^{-3} \text{ sr}^{-1}], \quad (\text{A.7})$$

and the photon flux,

$$q_\lambda = \frac{c\lambda^2 u_{\rho_\lambda}}{hc_a} \quad [\text{photon cm}^{-2} \text{ s}^{-1} \text{ sr}^{-1}]. \quad (\text{A.8})$$

The definite integrals for the energy density, energy flux, photon density, and photon flux, equations (A.5)-(A.8) are then respectively given by

$$U_\lambda = \int_\Omega \int_{\lambda_1}^{\lambda_2} u_{\rho_\lambda} d\lambda d\Omega \quad [\text{erg cm}^{-3}], \quad (\text{A.9})$$

$$F_\lambda = \int_\Omega \int_{\lambda_1}^{\lambda_2} cu_{\rho_\lambda} d\lambda d\Omega \quad [\text{erg cm}^{-2} \text{ s}^{-1}], \quad (\text{A.10})$$

$$P_\lambda = \int_\Omega \int_{\lambda_1}^{\lambda_2} \frac{\lambda u_{\rho_\lambda}}{hc_a} d\lambda d\Omega \quad [\text{photon cm}^{-3}], \quad \text{and} \quad (\text{A.11})$$

$$Q_\lambda = \int_\Omega \int_{\lambda_1}^{\lambda_2} \frac{c\lambda u_{\rho_\lambda}}{hc_a} d\lambda d\Omega \quad [\text{photon cm}^{-2} \text{ s}^{-1} \text{ sr}^{-1}], \quad (\text{A.12})$$

where  $\lambda_1 < \lambda_2$ .

Table A.1: Habing SED

Wavelength specific @ 1000 Å			
$u_\lambda$	$f_\lambda$	$q_\lambda$	$p_\lambda$
[erg cm <sup>-3</sup> sr <sup>-1</sup> ]	[erg cm <sup>-2</sup> s <sup>-1</sup> sr <sup>-1</sup> ]	[photon cm <sup>-2</sup> s <sup>-1</sup> sr <sup>-1</sup> ]	[photon cm <sup>-3</sup> sr <sup>-1</sup> ]
$3.18 \times 10^{-15}$	$9.54 \times 10^{-5}$	$4.80 \times 10^6$	$1.60 \times 10^{-4}$
Integration between 912 and 1108 Å			
$U_\lambda$	$F_\lambda$	$Q_\lambda$	$P_\lambda$
[erg cm <sup>-3</sup> ]	[erg cm <sup>-2</sup> s <sup>-1</sup> ]	[photon cm <sup>-2</sup> s <sup>-1</sup> ]	[photon cm <sup>-3</sup> ]
$7.90 \times 10^{-15}$	$2.37 \times 10^{-4}$	$1.21 \times 10^7$	$4.03 \times 10^{-4}$
Integration between 912 and 2066 Å			
$U_\lambda$	$F_\lambda$	$Q_\lambda$	$P_\lambda$
[erg cm <sup>-3</sup> ]	[erg cm <sup>-2</sup> s <sup>-1</sup> ]	[photon cm <sup>-2</sup> s <sup>-1</sup> ]	[photon cm <sup>-3</sup> ]
$5.28 \times 10^{-14}$	$1.58 \times 10^{-3}$	$1.19 \times 10^8$	$3.97 \times 10^{-3}$

## A.2 The Draine SED

A fit to the FUV interstellar background radiation was given by Draine [7],

$$q_{\rho E} = (1.658 \times 10^6 (E_e) - 2.152 \times 10^5 (E_e)^2 + 6.919 \times 10^3 (E_e)^3) \text{ [photon cm}^{-2} \text{ s}^{-1} \text{ eV}^{-1} \text{ sr}^{-1}], \quad (\text{A.13})$$

where  $E_e \equiv (E/1\text{eV})$ . This energy specific photon flux distribution can then be defined as

$$q_{\rho E} \equiv \frac{dq_E}{dE d\Omega} \text{ [photon cm}^{-2} \text{ s}^{-1} \text{ eV}^{-1} \text{ sr}^{-1}]. \quad (\text{A.14})$$

There is a  $1/4\pi$  term implicit in equation (A.13) which can be pulled out becoming

$$q_{\rho E} = \frac{1}{4\pi} \left( 2.084 \times 10^7 (E) - 2.704 \times 10^6 (E)^2 + 8.695 \times 10^4 (E)^3 \right) \text{ [photon cm}^{-2} \text{ s}^{-1} \text{ eV}^{-1} \text{ sr}^{-1}]. \quad (\text{A.15})$$

To convert the energy specific photon flux distribution to a wavelength specific photon flux distribution then the conversion  $q_{\rho E} dE = q_{\rho\lambda} d\lambda$  needs to be performed. Using the substitutions

$E = h_e c_a / \lambda$  and  $dE/d\lambda = |h_e c_a / \lambda^2|$  casts equation (A.15) into the form,

$$q_{\rho_\lambda} = \frac{1}{4\pi} \left( 2.084 \times 10^7 \left( \frac{h_e^2 c_a^2}{\lambda^3} \right) - 2.704 \times 10^6 \left( \frac{h_e^3 c_a^3}{\lambda^4} \right) + 8.695 \times 10^4 \left( \frac{h_e^4 c_a^4}{\lambda^5} \right) \right) \quad [\text{photon cm}^{-2} \text{s}^{-1} \text{\AA}^{-1} \text{sr}^{-1}], \quad (\text{A.16})$$

where  $h_e = 4.136 \times 10^{-15}$  eV s and  $h_e c_a = 1.240 \times 10^4$  eV \AA. From equation (A.16) the energy density can be found as,

$$u_\lambda = \frac{h c_a}{c} q_{\rho_\lambda} \quad [\text{erg cm}^{-3} \text{sr}^{-1}], \quad (\text{A.17})$$

the energy flux,

$$f_\lambda = h c_a q_{\rho_\lambda} \quad [\text{erg cm}^{-2} \text{s}^{-1} \text{sr}^{-1}], \quad (\text{A.18})$$

the photon flux,

$$q_\lambda = \lambda q_{\rho_\lambda} \quad [\text{photon cm}^{-2} \text{s}^{-1} \text{sr}^{-1}], \quad (\text{A.19})$$

and the photon density,

$$p_\lambda = \frac{\lambda}{c} q_{\rho_\lambda} \quad [\text{photon cm}^{-3} \text{sr}^{-1}]. \quad (\text{A.20})$$

The definite integrals for the energy density, energy flux, photon flux, and photon density, equations (A.17)-(A.20) are then respectively given by

$$U_\lambda = \int_\Omega \int_{\lambda_1}^{\lambda_2} \frac{h c_a}{c \lambda} q_{\rho_\lambda} d\lambda d\Omega \quad [\text{erg cm}^{-3}], \quad \text{and} \quad (\text{A.21})$$

$$F_\lambda = \int_\Omega \int_{\lambda_1}^{\lambda_2} \frac{h c_a}{\lambda} q_{\rho_\lambda} d\lambda d\Omega \quad [\text{erg cm}^{-2} \text{s}^{-1}], \quad (\text{A.22})$$

$$Q_\lambda = \int_\Omega \int_{\lambda_1}^{\lambda_2} q_{\rho_\lambda} d\lambda d\Omega \quad [\text{photon cm}^{-2} \text{s}^{-1}], \quad (\text{A.23})$$

$$P_\lambda = \int_\Omega \int_{\lambda_1}^{\lambda_2} \frac{1}{c} q_{\rho_\lambda} d\lambda d\Omega \quad [\text{photon cm}^{-3}], \quad (\text{A.24})$$

where  $\lambda_1 < \lambda_2$ .

Table A.2: Draine SED

Wavelength specific @ 1000 Å			
$u_\lambda$	$f_\lambda$	$q_\lambda$	$p_\lambda$
[erg cm <sup>-3</sup> sr <sup>-1</sup> ]	[erg cm <sup>-2</sup> s <sup>-1</sup> sr <sup>-1</sup> ]	[photon cm <sup>-2</sup> s <sup>-1</sup> sr <sup>-1</sup> ]	[photon cm <sup>-3</sup> sr <sup>-1</sup> ]
$5.52 \times 10^{-15}$	$1.65 \times 10^{-4}$	$8.33 \times 10^6$	$2.78 \times 10^{-4}$
Integration between 912 and 1108 Å			
$U_\lambda$	$F_\lambda$	$Q_\lambda$	$P_\lambda$
[erg cm <sup>-3</sup> ]	[erg cm <sup>-2</sup> s <sup>-1</sup> ]	[photon cm <sup>-2</sup> s <sup>-1</sup> ]	[photon cm <sup>-3</sup> ]
$1.35 \times 10^{-14}$	$4.06 \times 10^{-4}$	$2.10 \times 10^7$	$7.01 \times 10^{-4}$
Integration between 912 and 2066 Å			
$U_\lambda$	$F_\lambda$	$Q_\lambda$	$P_\lambda$
[erg cm <sup>-3</sup> ]	[erg cm <sup>-2</sup> s <sup>-1</sup> ]	[photon cm <sup>-2</sup> s <sup>-1</sup> ]	[photon cm <sup>-3</sup> ]
$8.97 \times 10^{-14}$	$2.69 \times 10^{-3}$	$1.95 \times 10^8$	$6.50 \times 10^{-3}$

### A.3 The Draine and Bertoldi SED

An alternative version of the Draine FUV interstellar background radiation was given in Draine and Bertoldi [12, 7],

$$u_{\rho\lambda} = \frac{4 \times 10^{-14}}{4\pi} \chi \left( \frac{3.1016 \times 10^{10}}{\lambda^4} - \frac{4.9913 \times 10^{13}}{\lambda^5} + \frac{1.9987 \times 10^{16}}{\lambda^6} \right) \quad [\text{erg cm}^{-3} \text{ \AA}^{-1} \text{ sr}^{-1}], \quad (\text{A.25})$$

where  $u_{\rho\lambda}$  is the wavelength specific energy density and is defined as,

$$u_{\rho\lambda} \equiv \frac{du_\lambda}{d\lambda d\Omega} \quad [\text{erg cm}^{-3} \text{ \AA}^{-1} \text{ sr}^{-1}], \quad (\text{A.26})$$

$\chi$  is a normalization factor to the Habing SED at a wavelength of 1000 Å and is given as,

$$\chi \equiv \frac{(\lambda u_{H\rho\lambda})_{1000 \text{ \AA}}}{4 \times 10^{-14} \text{ erg cm}^{-3}}, \quad (\text{A.27})$$

where  $u_{H\rho\lambda}$  is equation (A.3) and  $\chi = 1.71$ . From equation (A.25) the energy density can be found as,

$$u_\lambda = \lambda u_{\rho\lambda} \quad [\text{erg cm}^{-3} \text{ sr}^{-1}], \quad (\text{A.28})$$

the energy flux,

$$f_\lambda = c\lambda u_{\rho\lambda} \quad [\text{erg cm}^{-2} \text{s}^{-1} \text{sr}^{-1}], \quad (\text{A.29})$$

the photon flux,

$$q_\lambda = \frac{c\lambda^2}{hc_a} u_{\rho\lambda} \quad [\text{photon cm}^{-2} \text{s}^{-1} \text{sr}^{-1}], \quad (\text{A.30})$$

and the photon density,

$$p_\lambda = \frac{\lambda^2}{hc_a} u_{\rho\lambda} \quad [\text{photon cm}^{-3} \text{sr}^{-1}]. \quad (\text{A.31})$$

The definite integrals for the energy density, energy flux, photon flux, and photon density, equations (A.28)-(A.31) are then respectively given by

$$U_\lambda = \int_\Omega \int_{\lambda_1}^{\lambda_2} u_{\rho\lambda} d\lambda d\Omega \quad [\text{erg cm}^{-3}], \quad \text{and} \quad (\text{A.32})$$

$$F_\lambda = \int_\Omega \int_{\lambda_1}^{\lambda_2} cu_{\rho\lambda} d\lambda d\Omega \quad [\text{erg cm}^{-2} \text{s}^{-1}], \quad (\text{A.33})$$

$$Q_\lambda = \int_\Omega \int_{\lambda_1}^{\lambda_2} \frac{c\lambda}{hc_a} u_{\rho\lambda} d\lambda d\Omega \quad [\text{photon cm}^{-2} \text{s}^{-1}], \quad (\text{A.34})$$

$$P_\lambda = \int_\Omega \int_{\lambda_1}^{\lambda_2} \frac{\lambda}{hc_a} u_{\rho\lambda} d\lambda d\Omega \quad [\text{photon cm}^{-3}], \quad (\text{A.35})$$

where  $\lambda_1 < \lambda_2$ .

Table A.3: Draine &amp; Bertoldi SED

Wavelength specific @ 1000 Å			
$u_\lambda$	$f_\lambda$	$q_\lambda$	$p_\lambda$
[erg cm <sup>-3</sup> sr <sup>-1</sup> ]	[erg cm <sup>-2</sup> s <sup>-1</sup> sr <sup>-1</sup> ]	[photon cm <sup>-2</sup> s <sup>-1</sup> sr <sup>-1</sup> ]	[photon cm <sup>-3</sup> sr <sup>-1</sup> ]
$5.93 \times 10^{-15}$	$1.78 \times 10^{-5}$	$8.95 \times 10^6$	$2.99 \times 10^{-4}$
Integration between 912 and 1108 Å			
$U_\lambda$	$F_\lambda$	$Q_\lambda$	$P_\lambda$
[erg cm <sup>-3</sup> ]	[erg cm <sup>-2</sup> s <sup>-1</sup> ]	[photon cm <sup>-2</sup> s <sup>-1</sup> ]	[photon cm <sup>-3</sup> ]
$1.46 \times 10^{-14}$	$4.37 \times 10^{-4}$	$2.26 \times 10^7$	$7.52 \times 10^{-4}$
Integration between 912 and 2066 Å			
$U_\lambda$	$F_\lambda$	$Q_\lambda$	$P_\lambda$
[erg cm <sup>-3</sup> ]	[erg cm <sup>-2</sup> s <sup>-1</sup> ]	[photon cm <sup>-2</sup> s <sup>-1</sup> ]	[photon cm <sup>-3</sup> ]
$9.13 \times 10^{-14}$	$2.74 \times 10^{-3}$	$1.98 \times 10^8$	$6.59 \times 10^{-3}$

## A.4 The Draine - Sternberg SED

Another version of the Draine FUV interstellar background radiation was given by Sternberg [2, 93],

$$q_{\rho\nu} = \frac{1}{4\pi} \left( 1.068 \times 10^{-3} \left( \frac{\nu}{c_a} \right) - 1.719 \times 10^0 \left( \frac{\nu^2}{c_a^2} \right) + 6.853 \times 10^2 \left( \frac{\nu^3}{c_a^3} \right) \right) \quad [\text{photon cm}^{-2} \text{ s}^{-1} \text{ Hz}^{-1} \text{ sr}^{-1}], \quad (\text{A.36})$$

where the substitution  $1/\lambda = \nu/c_a$  was made. This equation varies from that given in equation (A1) of [93], as equation (A.36) is given in wavelength equivalent units of angstroms where as equation (A1) is given in wavelength equivalent units of nanometers. This frequency specific photon flux distribution can be defined as,

$$q_{\rho\nu} \equiv \frac{dq_\nu}{d\nu d\Omega} \quad [\text{photon cm}^{-2} \text{ s}^{-1} \text{ Hz}^{-1} \text{ sr}^{-1}]. \quad (\text{A.37})$$

To convert the frequency specific photon flux distribution to a wavelength specific photon flux distribution the conversion  $q_{\rho\nu} d\nu = q_{\rho\lambda} d\lambda$  needs to be performed. Using the substitutions  $\nu = c_a/\lambda$  and  $d\nu/d\lambda = |c_a/\lambda^2|$  casts equation (A.36) into the form,

$$q_{\rho\lambda} = \frac{c_a}{4\pi} \left( \frac{1.068 \times 10^{-3}}{\lambda^3} - \frac{1.719 \times 10^0}{\lambda^4} + \frac{6.853 \times 10^2}{\lambda^5} \right) \quad [\text{photon cm}^{-2} \text{ s}^{-1} \text{ Å}^{-1} \text{ sr}^{-1}]. \quad (\text{A.38})$$

From equation (A.38) the energy density can be found as,

$$u_\lambda = \frac{hc_a}{c} q_{\rho_\lambda} \quad [\text{erg cm}^{-3} \text{ sr}^{-1}], \quad (\text{A.39})$$

the energy flux,

$$f_\lambda = hc_a q_{\rho_\lambda} \quad [\text{erg cm}^{-2} \text{ s}^{-1} \text{ sr}^{-1}], \quad (\text{A.40})$$

the photon flux,

$$q_\lambda = \lambda q_{\rho_\lambda} \quad [\text{photon cm}^{-2} \text{ s}^{-1} \text{ sr}^{-1}], \quad (\text{A.41})$$

and the photon density,

$$p_\lambda = \frac{\lambda}{c} q_{\rho_\lambda} \quad [\text{photon cm}^{-3} \text{ sr}^{-1}]. \quad (\text{A.42})$$

The definite integrals for the energy density, energy flux, photon flux, and photon density, equations (A.39)-(A.42) are then respectively given by,

$$U_\lambda = \int_\Omega \int_{\lambda_1}^{\lambda_2} \frac{hc_a}{c\lambda} q_{\rho_\lambda} d\lambda d\Omega \quad [\text{erg cm}^{-3}], \quad \text{and} \quad (\text{A.43})$$

$$F_\lambda = \int_\Omega \int_{\lambda_1}^{\lambda_2} \frac{hc_a}{\lambda} q_{\rho_\lambda} d\lambda d\Omega \quad [\text{erg cm}^{-2} \text{ s}^{-1}], \quad (\text{A.44})$$

$$Q_\lambda = \int_\Omega \int_{\lambda_1}^{\lambda_2} q_{\rho_\lambda} d\lambda d\Omega \quad [\text{photon cm}^{-2} \text{ s}^{-1}], \quad (\text{A.45})$$

$$P_\lambda = \int_\Omega \int_{\lambda_1}^{\lambda_2} \frac{1}{c} q_{\rho_\lambda} d\lambda d\Omega \quad [\text{photon cm}^{-3}], \quad (\text{A.46})$$

where  $\lambda_1 < \lambda_2$ .

There are other SED's based on [7] such as those found in [36, 37, 38] where the techniques described in this appendix can be used to find radiation field quantities that may be needed.

Table A.4: Draine - Sternberg SED

Wavelength specific @ 1000 Å			
$u_\lambda$	$f_\lambda$	$q_\lambda$	$p_\lambda$
[erg cm <sup>-3</sup> sr <sup>-1</sup> ]	[erg cm <sup>-2</sup> s <sup>-1</sup> sr <sup>-1</sup> ]	[photon cm <sup>-2</sup> s <sup>-1</sup> sr <sup>-1</sup> ]	[photon cm <sup>-3</sup> sr <sup>-1</sup> ]
$5.42 \times 10^{-15}$	$1.63 \times 10^{-4}$	$8.18 \times 10^6$	$2.73 \times 10^{-4}$
Integration between 912 and 1108 Å			
$U_\lambda$	$F_\lambda$	$Q_\lambda$	$P_\lambda$
[erg cm <sup>-3</sup> ]	[erg cm <sup>-2</sup> s <sup>-1</sup> ]	[photon cm <sup>-2</sup> s <sup>-1</sup> ]	[photon cm <sup>-3</sup> ]
$1.33 \times 10^{-14}$	$3.99 \times 10^{-4}$	$2.07 \times 10^7$	$6.89 \times 10^{-4}$
Integration between 912 and 2066 Å			
$U_\lambda$	$F_\lambda$	$Q_\lambda$	$P_\lambda$
[erg cm <sup>-3</sup> ]	[erg cm <sup>-2</sup> s <sup>-1</sup> ]	[photon cm <sup>-2</sup> s <sup>-1</sup> ]	[photon cm <sup>-3</sup> ]
$8.92 \times 10^{-14}$	$2.68 \times 10^{-3}$	$1.94 \times 10^8$	$6.48 \times 10^{-3}$

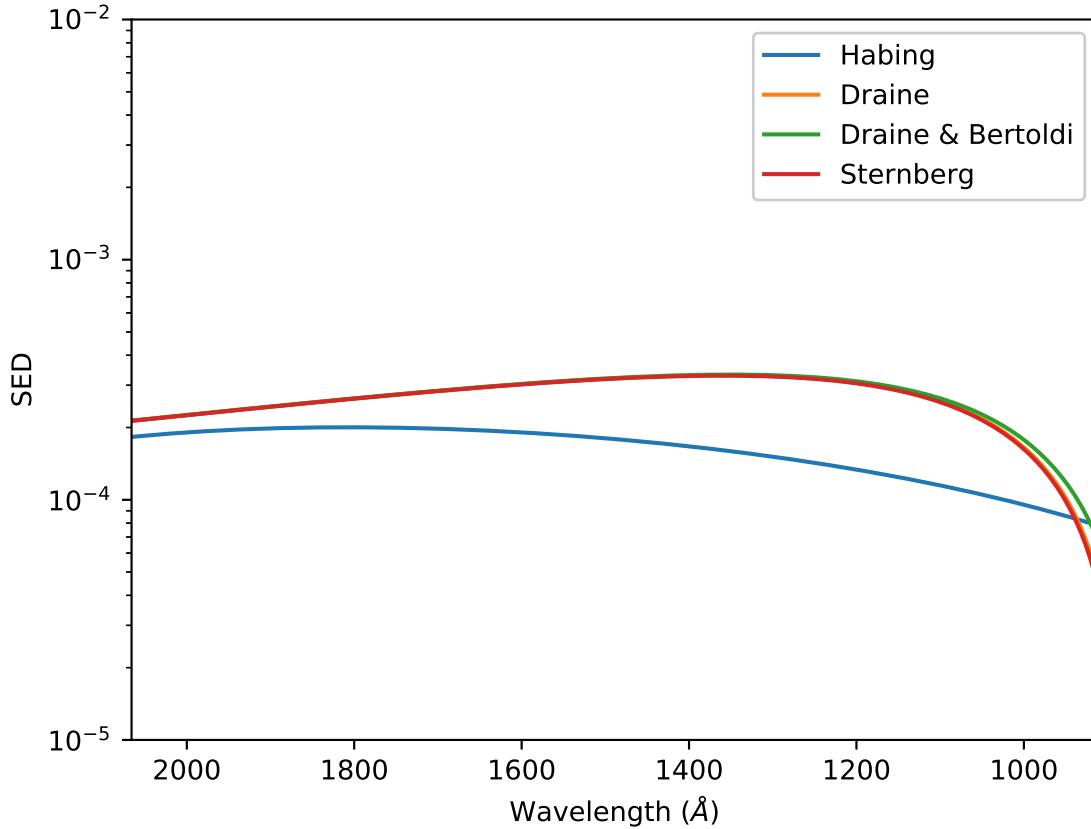


Figure A.1: A comparison of the SED's in this appendix between 6 - 13.6 eV

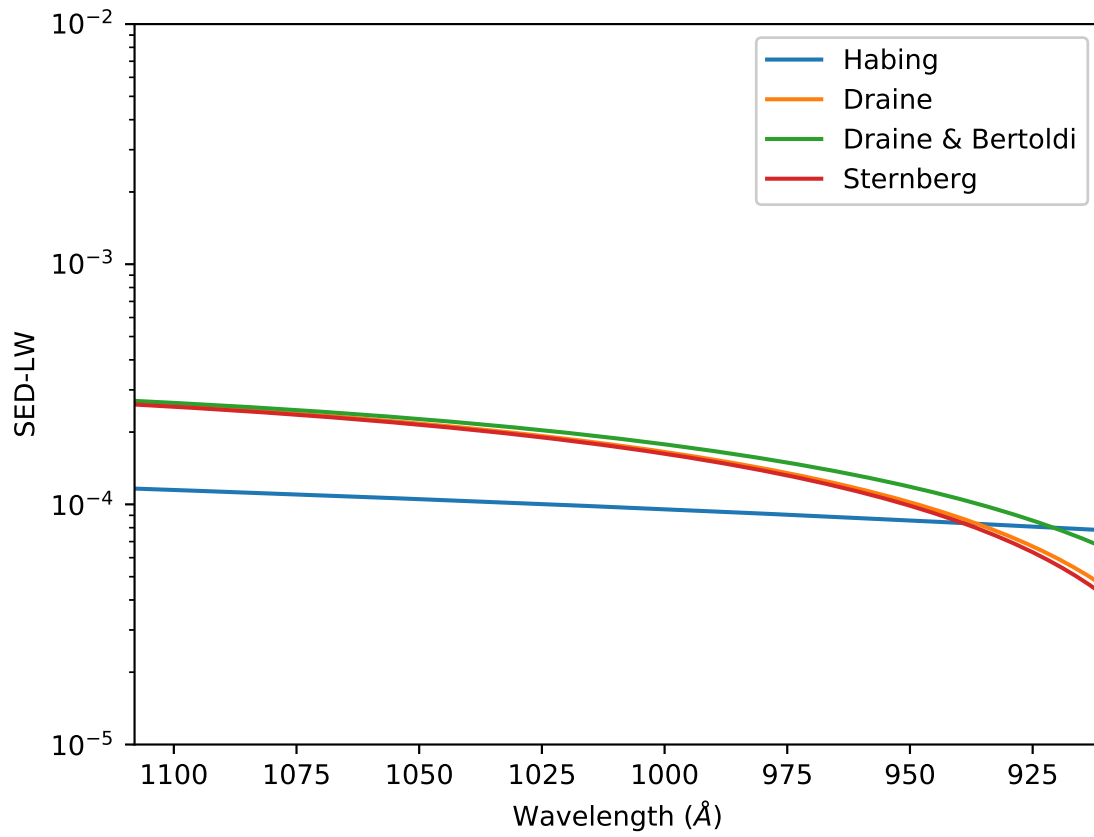


Figure A.2: A comparison of the SED's in this appendix between 11.2 - 13.6 eV

## Appendix B

# Hard X-ray Attenuation and Energy Deposition

This appendix describes the computational solution of the HXR attenuation function as well as its effect on the energy deposition rate. The attenuation function has two components to it, the energy dependent attenuated spectral energy distribution function  $S(\tau_X)$  and the optical depth  $\tau_X^{-\phi-1}$ .

The simpler of the two terms to calculate is the HXR optical depth dependent function  $\tau_X^{-\phi-1}$  that was derived in equations (3.10) - (3.12) and it will be described first. This is simply found by using the optical depth  $\tau_X = \sigma_X N_H$  where  $\sigma_X = 2.6 \times 10^{-22} \text{ cm}^2$ , and the exponent  $\phi = (\alpha_X - 1)/\gamma$  with the relevant values  $\alpha_X = 0.7$  and  $\gamma = 8/3$  being used. This is shown in Figure B.1.

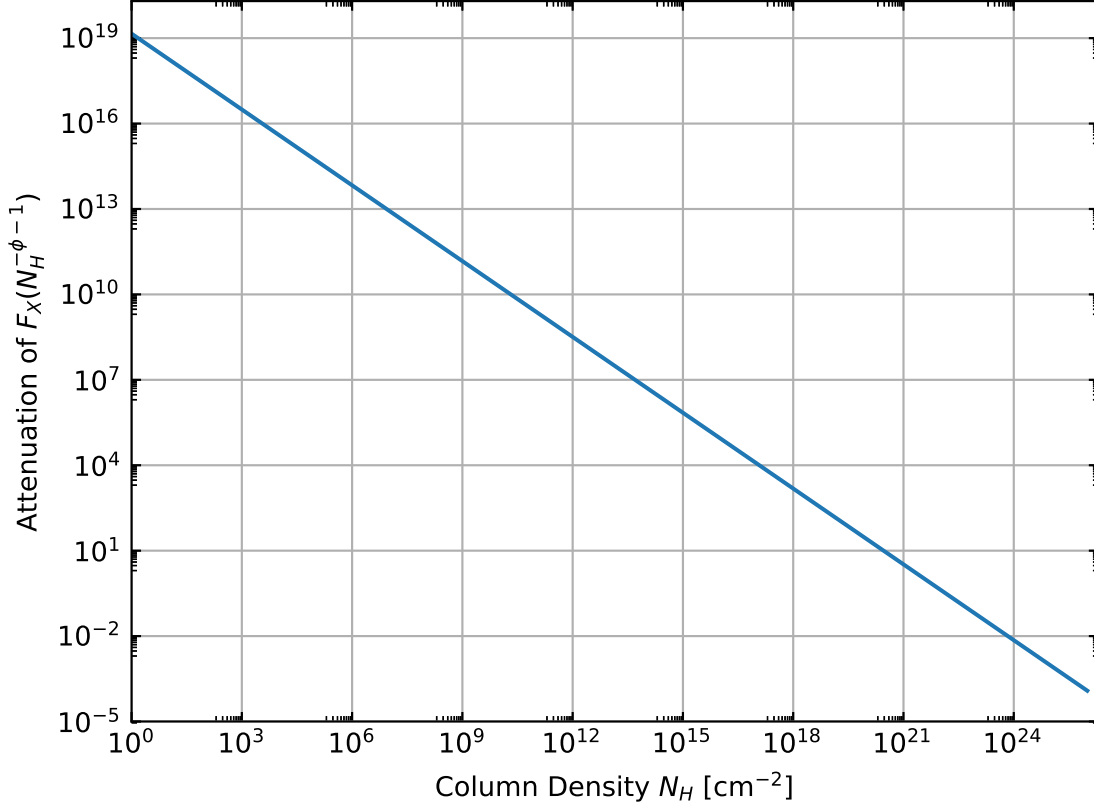


Figure B.1: The attenuation of  $F_X(N_H^{-\phi-1})$ .

As described in § 3.1.1, the function  $S(\tau_X)$  is found by calculating the generalized incomplete gamma function up to the total hydrogen column density  $N_H$  in question. This is given here again as

$$S(\tau_X) \equiv \int_{u_{\min}}^{u_{\max}} u^\phi e^u du \quad (\text{B.1})$$

where  $u \equiv \tau_X E_k^{-\gamma}$ ,  $\tau_X = \sigma_X N_H$ ,  $u_{\min} = \tau_X E_{k,\max}^{-\gamma}$ ,  $u_{\max} = \tau_X E_{k,\min}^{-\gamma}$ ,  $E_{k,\max} = 100$  keV,  $E_{k,\min} = 1$  keV,  $\phi = (\alpha_X - 1)/\gamma$ ,  $\alpha_X = 0.7$  and  $\gamma = 8/3$ .

The calculation of the generalized incomplete gamma function was done as a difference of the normalized lower incomplete gamma function. The relevant commands from the `scipy.special` package in Python 2.7.10 are `gamma(a)` and `gammaincc(a, x)`. This was done in two different ways: one using a difference of upper incomplete gamma functions and the other using a difference of lower incomplete gamma functions. Both gave identical results however the method using the

lower incomplete gamma functions was on the order of 4 times faster than the upper incomplete gamma functions and so that was used for the calculations. It will be seen in Figure B.2 that floating point errors led to the function being non-smooth over its entire domain.

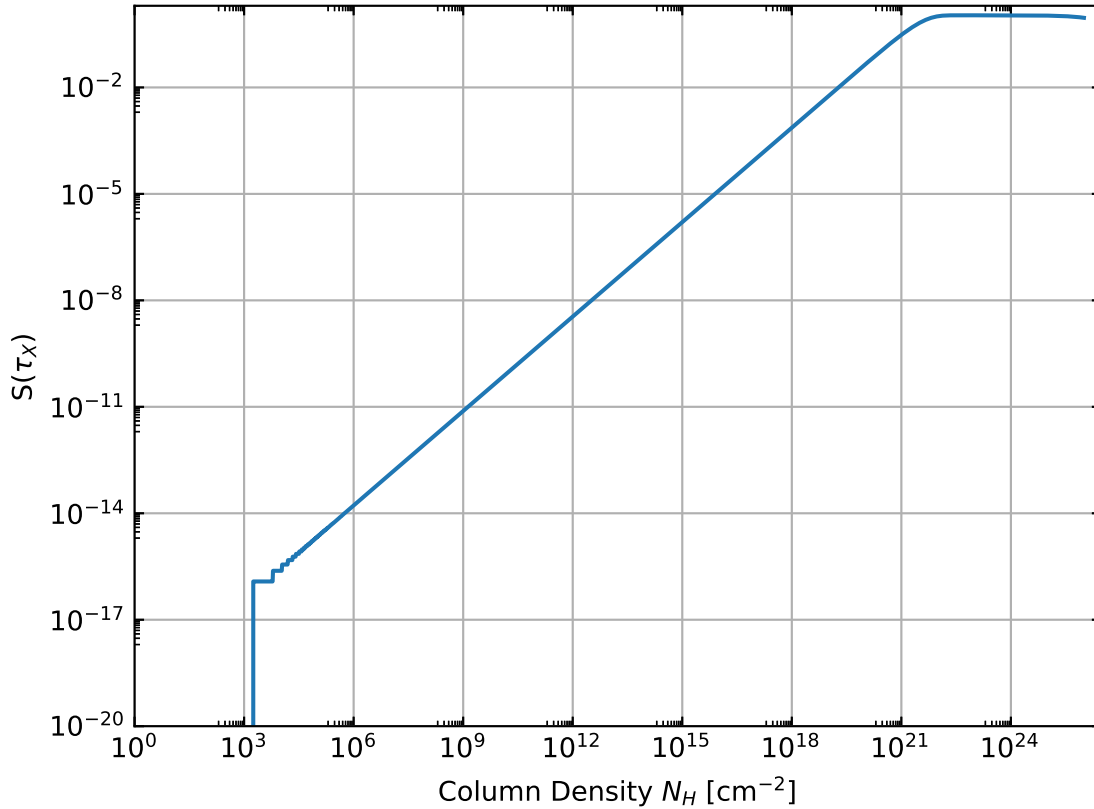


Figure B.2: The attenuation term  $S(\tau_X)$  calculated as a difference of lower incomplete gamma functions using the `scipy.special` package.

To rectify this problem, the `mpmath` package was used to increase the number of decimal places that the calculation used. This used the `gammainc_gen_low(a, x1, x2)` command which gave the smooth curve in Figure B.3

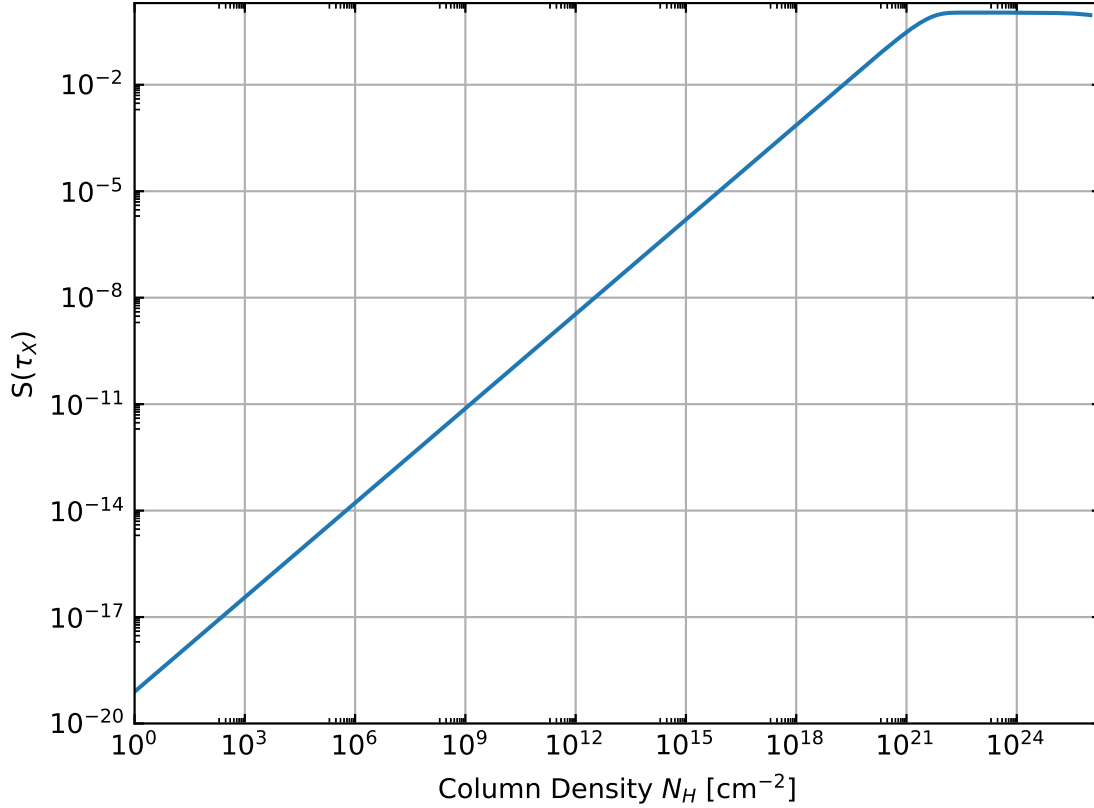


Figure B.3: The attenuation term  $S(\tau_X)$  calculated as a difference of lower incomplete gamma functions using the `mpmath` package.

The total attenuation term  $B$  for the HXR field is given by the combination

$$B \equiv \frac{S(\tau_X)}{\tau_X^{\phi+1}}. \quad (\text{B.2})$$

This is shown in Figure B.4 It can be seen that the attenuation doesn't become significant until a total hydrogen column density of about  $N_H \sim 10^{20} \text{ cm}^{-2}$  is reached. Note that the attenuation term  $B$  is not normalized to 1 as it would be if it was strictly attenuating the HXR radiation field. It is a part of the total energy deposition rate of the HXR along with the "unattenuated" portion  $\beta$ . This is not a problem as the computation uses the combined  $\beta B$  term to determine densities.

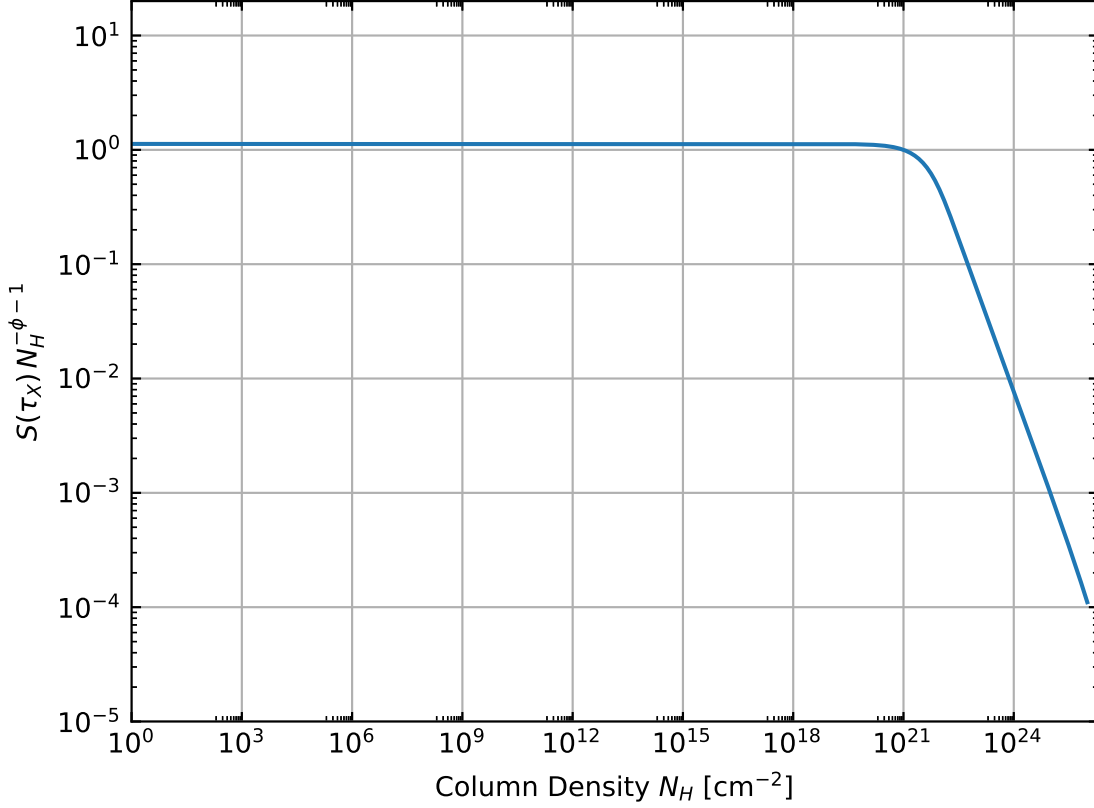


Figure B.4: The total attenuation term of the HXR spectrum.

As the solution of  $S(\tau_X)$  is a function of the hydrogen column density, solving for the atomic and molecular hydrogen fractions equations (4.2a) and (4.2b) respectively, is computationally intensive so an analytic approximation to  $B$  was found. A close approximation was found for  $B$  in log-log scale that is more computationally efficient. This approximation can be given by an oblique hyperbola which is given in asymptotic form as

$$(0.000007268N_H + B - 0.0522466)(0.8987N_H + B - 19.4507) = 0.04. \quad (\text{B.3})$$

For the computational model, equation (B.3) is given in terms of  $B(N_H)$

$$B = -5.26963 \sqrt{7.27113 \times 10^{-3} N_H^2 - 3.13897 \times 10^{-1} N_H + 3.38921} - 0.44935 N_H + 9.75147 \quad (\text{B.4})$$

A comparison of equation (B.2) and (B.3) is shown in Figures (B.5) and (B.6)

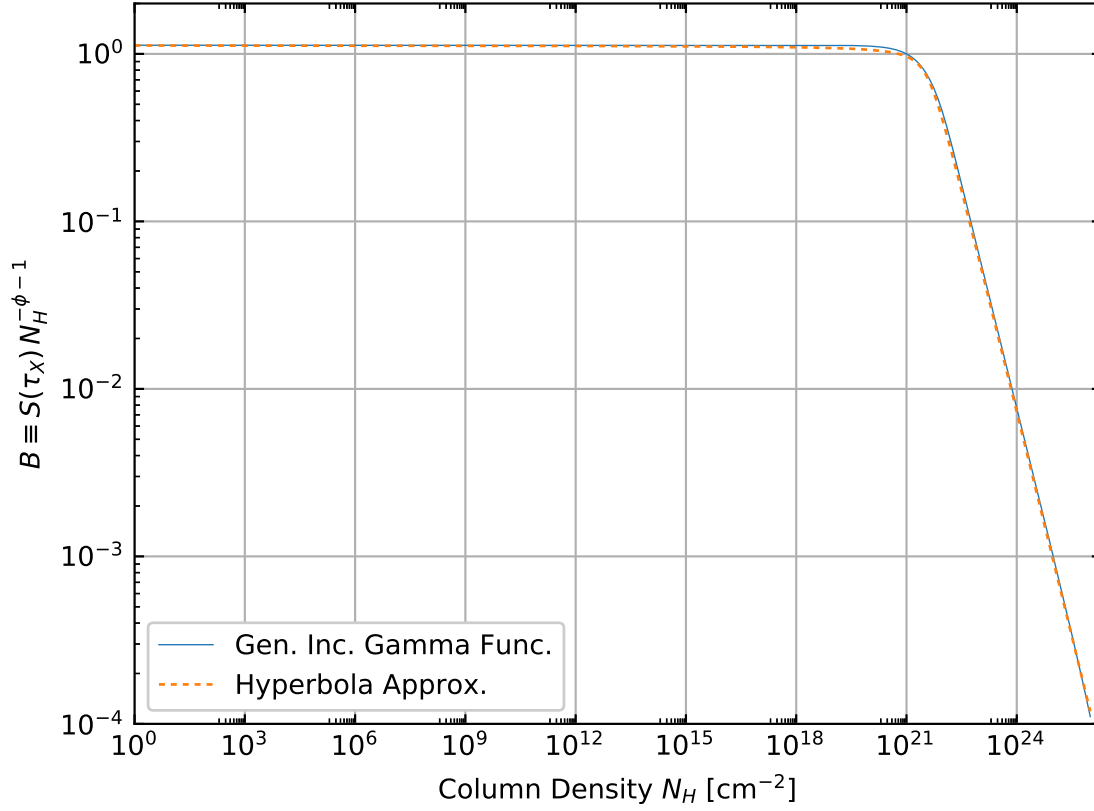


Figure B.5: A comparison of the analytic and numerical forms of  $S(\tau_X)N_H^{-\phi-1}$ .

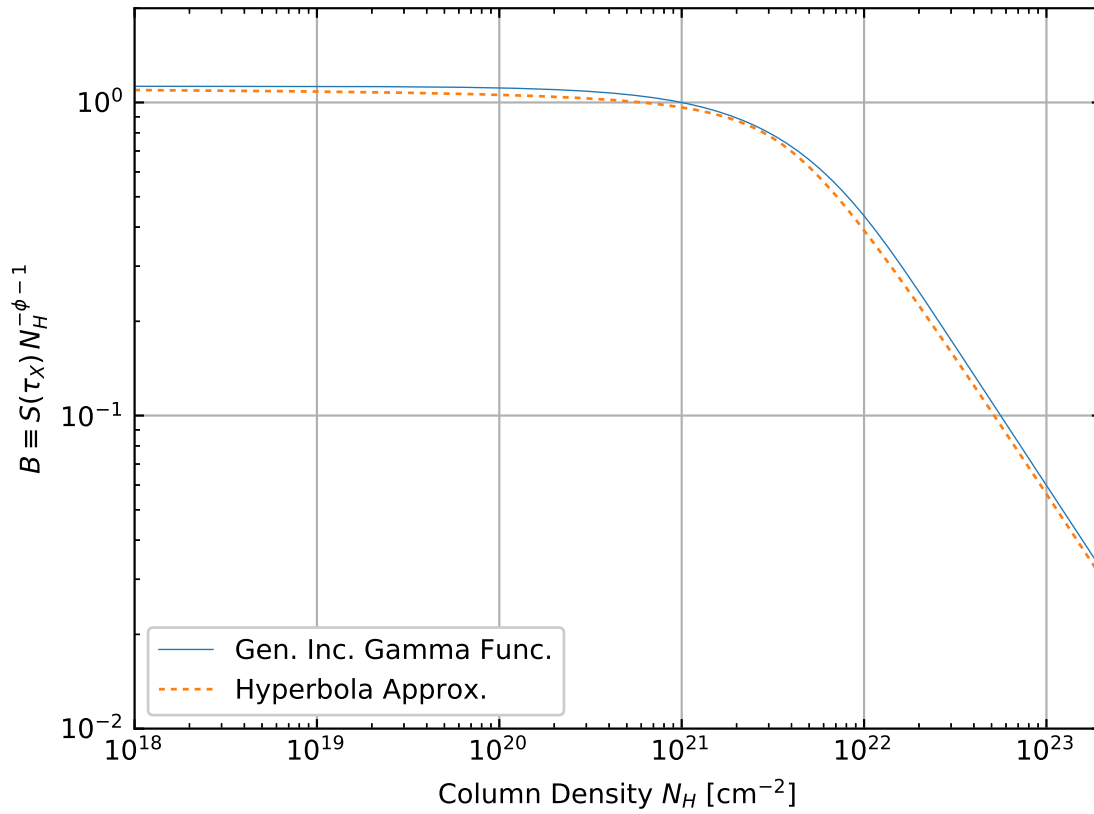


Figure B.6: A comparison of the analytic and numerical forms of  $S(\tau_X)N_H^{-\phi-1}$  in the region where attenuation begins to occur.

## Appendix C

# Analytic Best Fit Curves

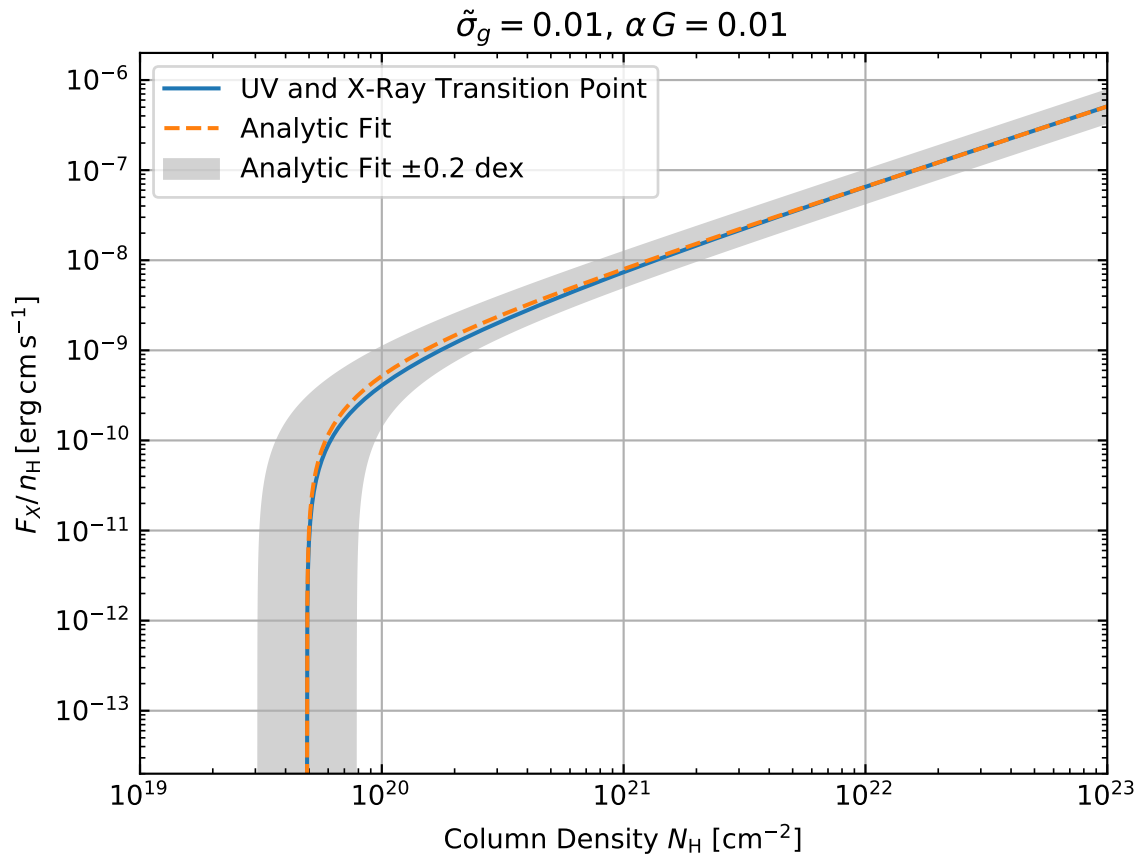


Figure C.1: The HXR perturbation transition point curve (solid blue line) superimposed with the analytic model (orange dashed line) for  $\tilde{\sigma}_d = 0.01$  and  $\alpha G = 0.01$ . A variation of  $\pm 0.2$  dex is shown around the analytic fit line (light grey strip).

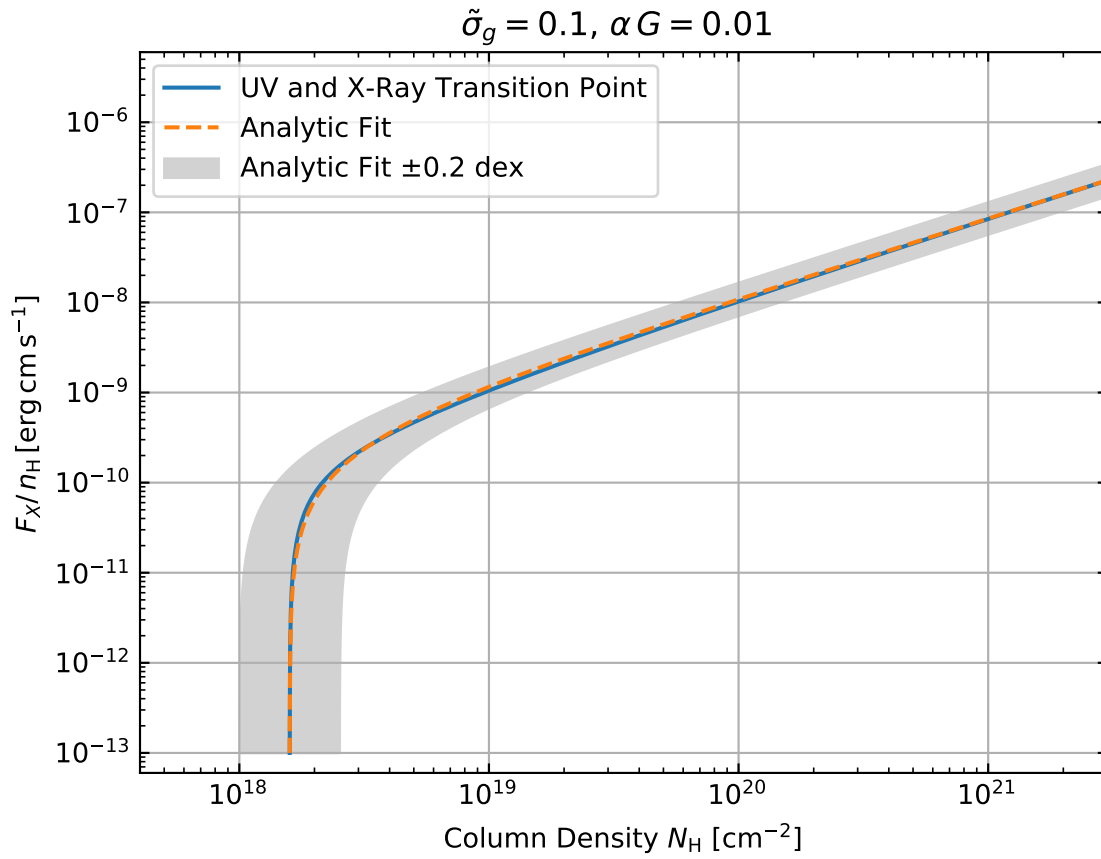


Figure C.2: The HXR perturbation transition point curve (solid blue line) superimposed with the analytic model (orange dashed line) for  $\tilde{\sigma}_d = 0.1$  and  $\alpha G = 0.01$ . A variation of  $\pm 0.2$  dex is shown around the analytic fit line (light grey strip).

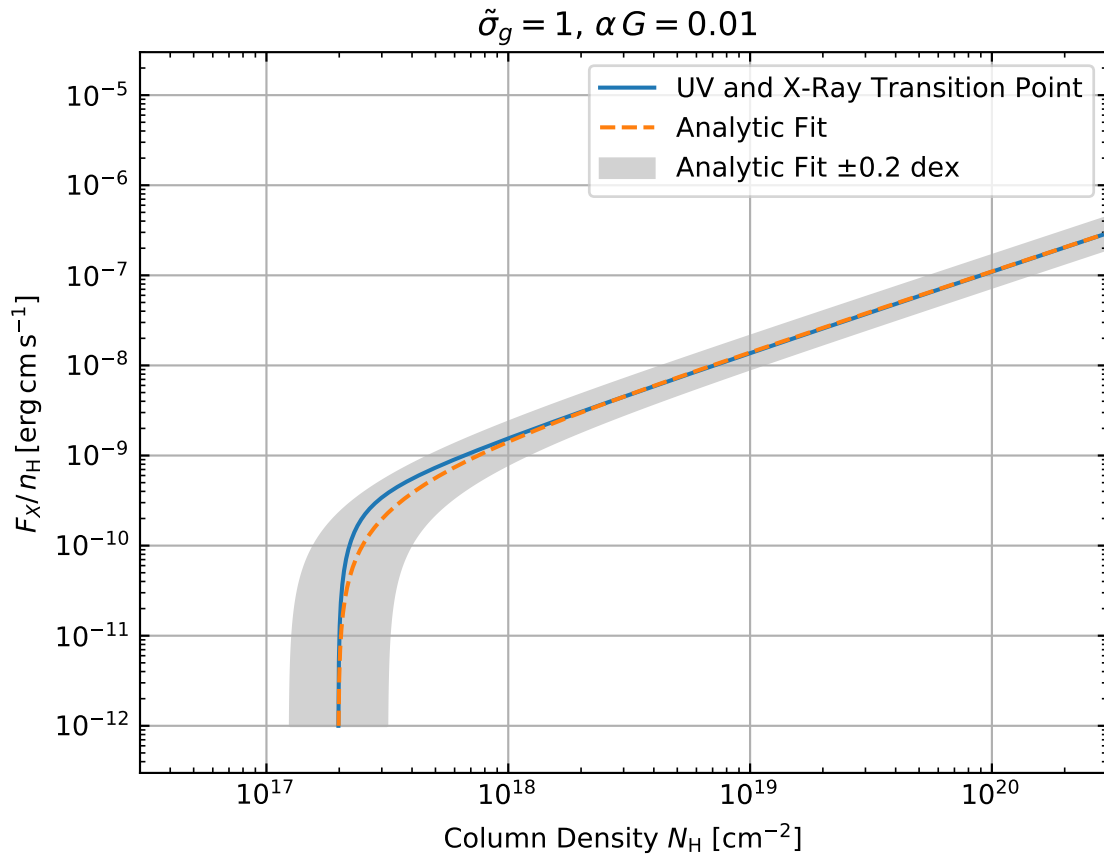


Figure C.3: The HXR perturbation transition point curve (solid blue line) superimposed with the analytic model (orange dashed line) for  $\tilde{\sigma}_d = 1$  and  $\alpha G = 0.01$ . A variation of  $\pm 0.2$  dex is shown around the analytic fit line (light grey strip).

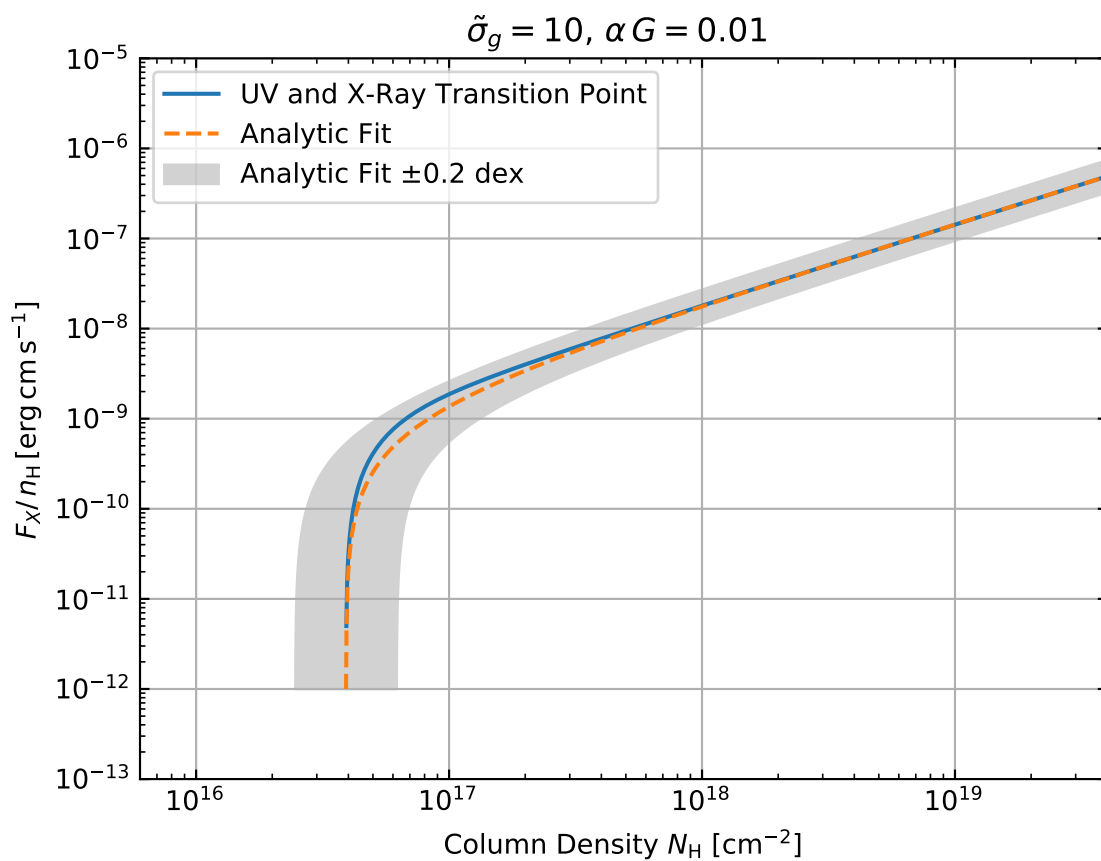


Figure C.4: The HXR perturbation transition point curve (solid blue line) superimposed with the analytic model (orange dashed line) for  $\tilde{\sigma}_d = 10$  and  $\alpha G = 0.01$ . A variation of  $\pm 0.2$  dex is shown around the analytic fit line (light grey strip).

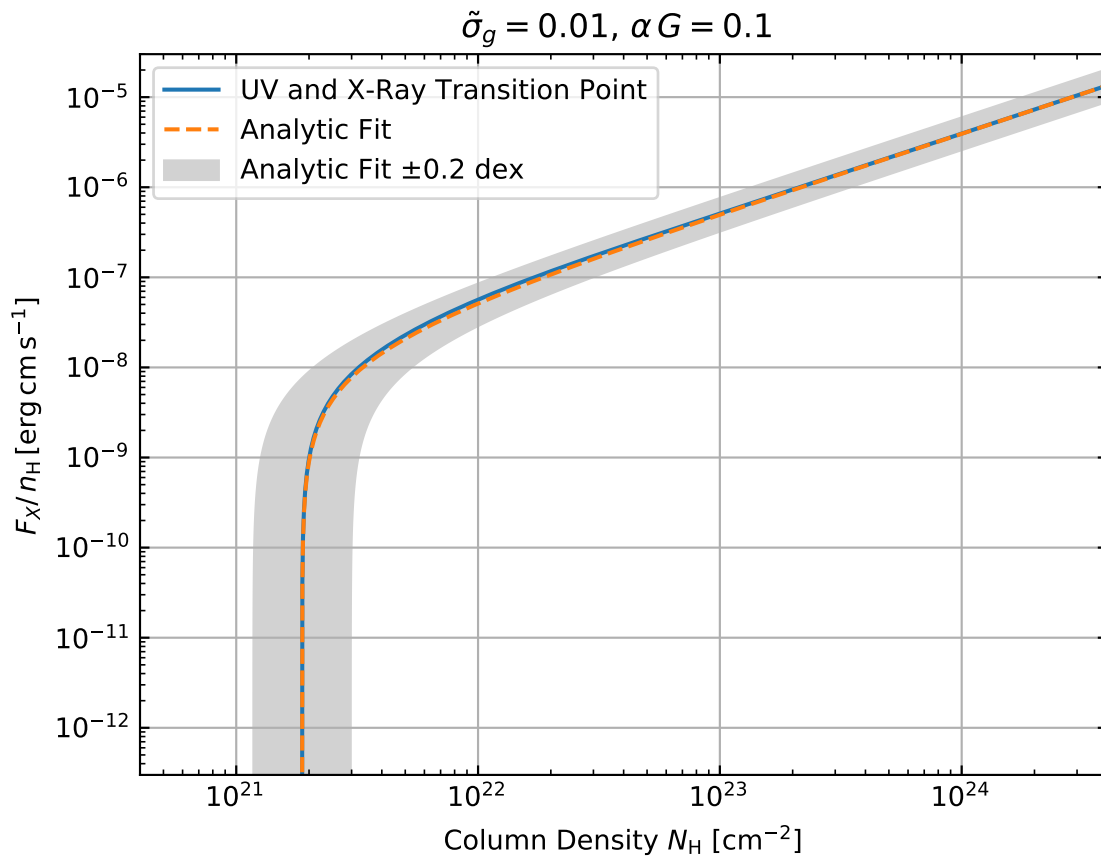


Figure C.5: The HXR perturbation transition point curve (solid blue line) superimposed with the analytic model (orange dashed line) for  $\tilde{\sigma}_d = 0.01$  and  $\alpha G = 0.1$ . A variation of  $\pm 0.2$  dex is shown around the analytic fit line (light grey strip).

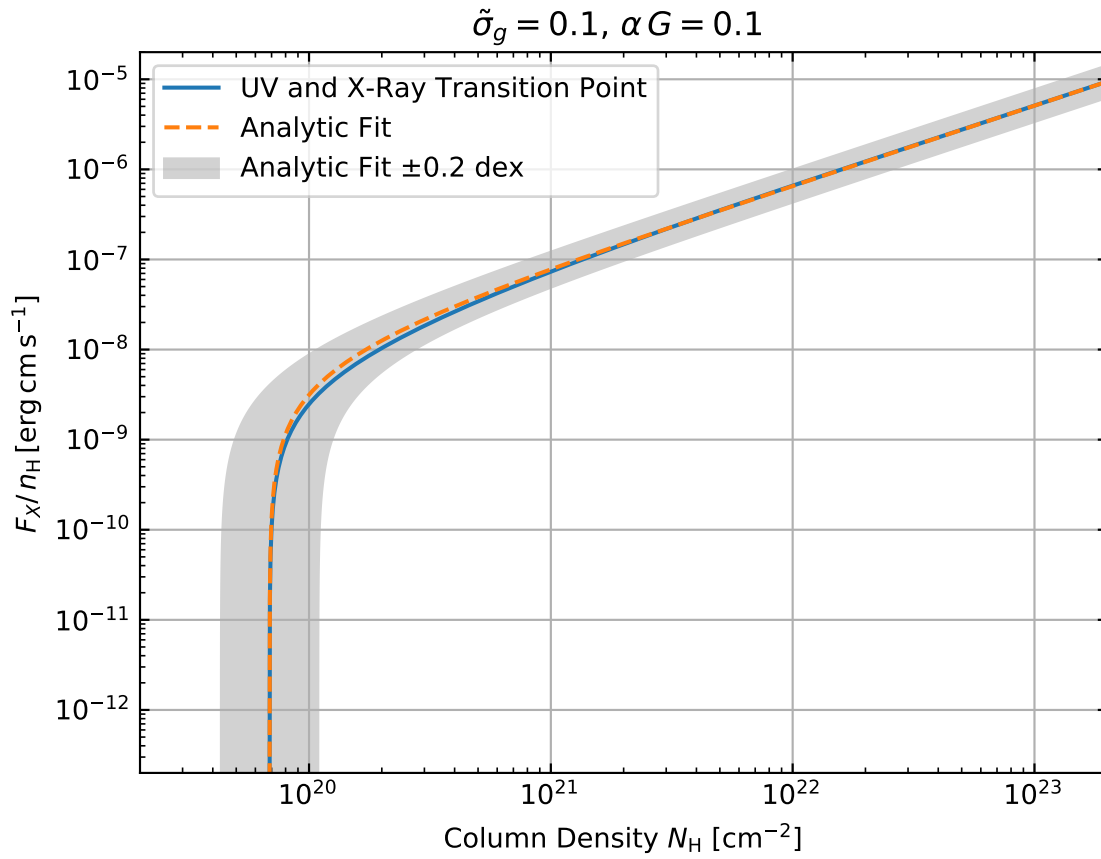


Figure C.6: The HXR perturbation transition point curve (solid blue line) superimposed with the analytic model (orange dashed line) for  $\tilde{\sigma}_d = 0.1$  and  $\alpha G = 0.1$ . A variation of  $\pm 0.2$  dex is shown around the analytic fit line (light grey strip).

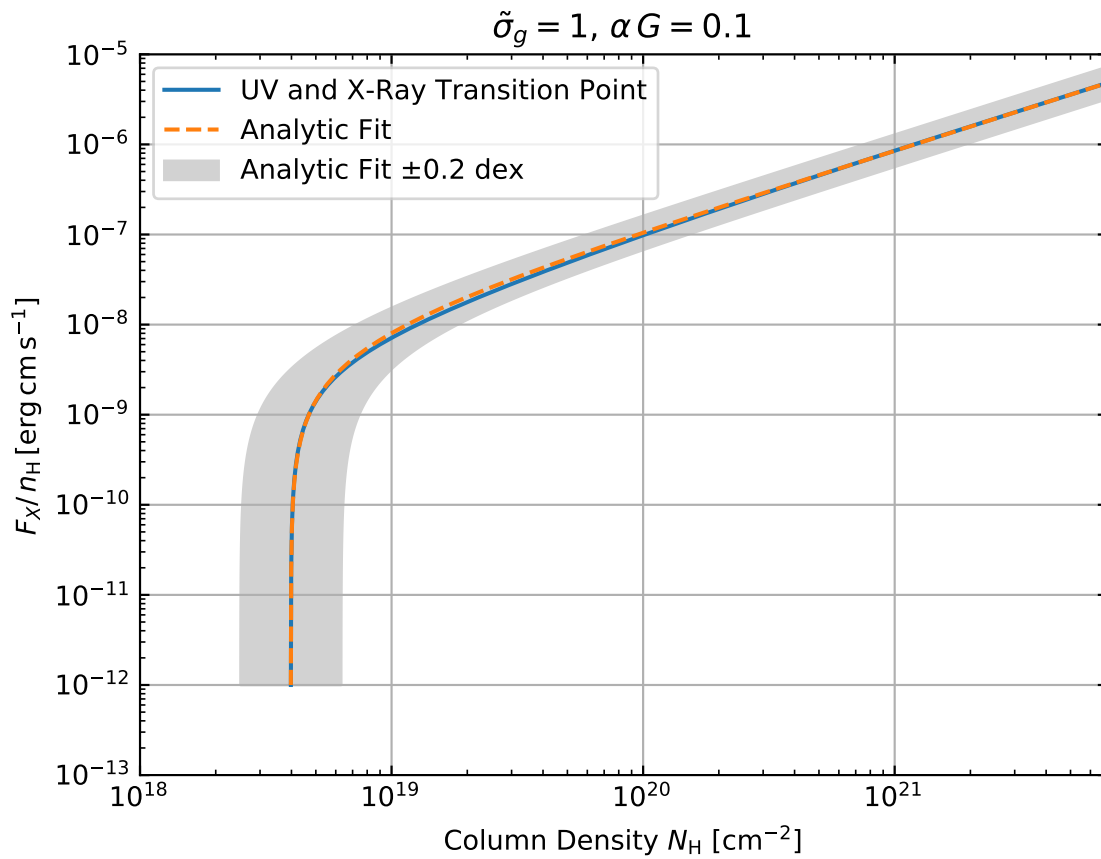


Figure C.7: The HXR perturbation transition point curve (solid blue line) superimposed with the analytic model (orange dashed line) for  $\tilde{\sigma}_d = 1$  and  $\alpha G = 0.1$ . A variation of  $\pm 0.2$  dex is shown around the analytic fit line (light grey strip).

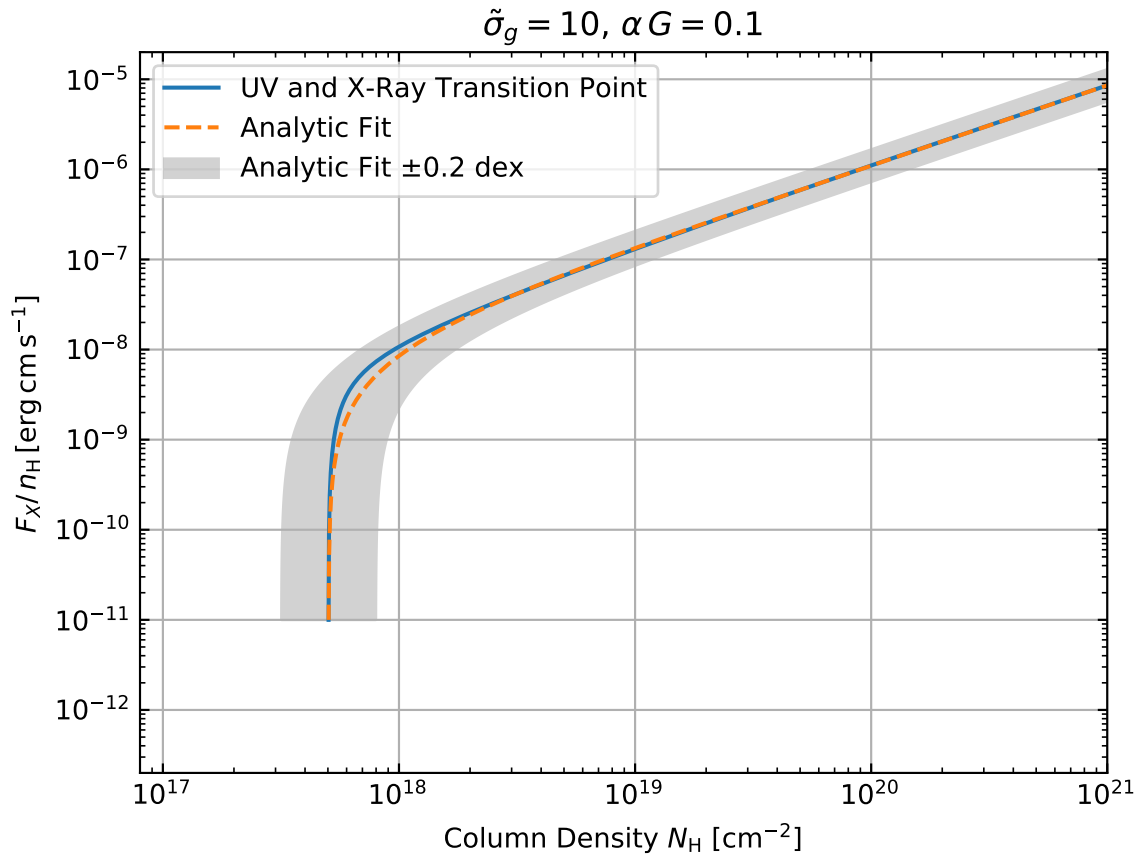


Figure C.8: The HXR perturbation transition point curve (solid blue line) superimposed with the analytic model (orange dashed line) for  $\tilde{\sigma}_d = 10$  and  $\alpha G = 0.1$ . A variation of  $\pm 0.2$  dex is shown around the analytic fit line (light grey strip).

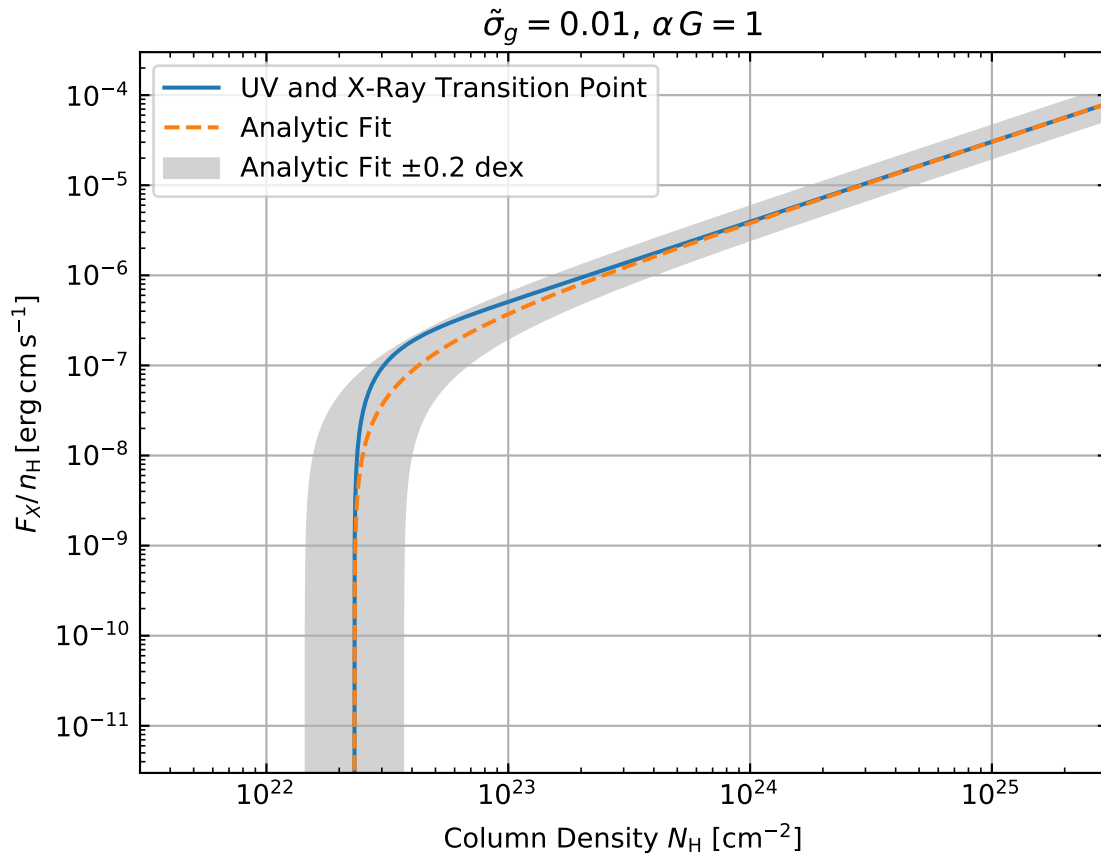


Figure C.9: The HXR perturbation transition point curve (solid blue line) superimposed with the analytic model (orange dashed line) for  $\tilde{\sigma}_d = 0.01$  and  $\alpha G = 1$ . A variation of  $\pm 0.2$  dex is shown around the analytic fit line (light grey strip).

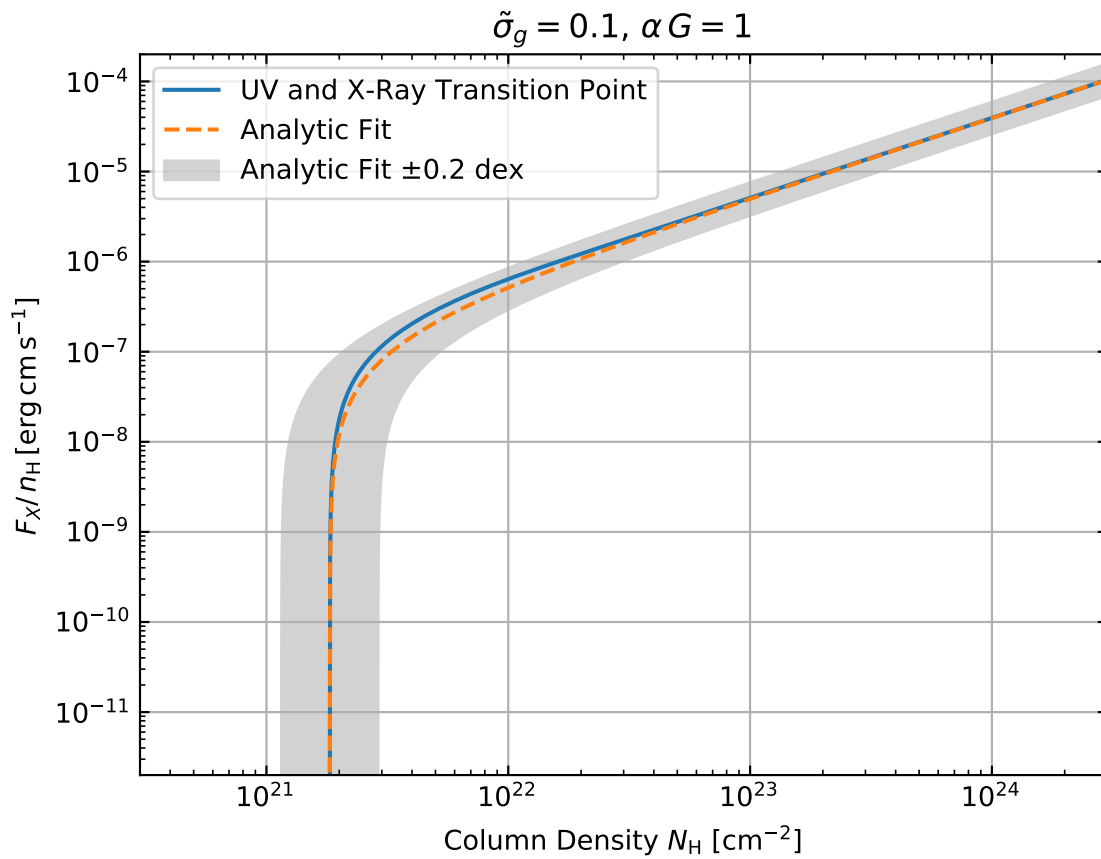


Figure C.10: The HXR perturbation transition point curve (solid blue line) superimposed with the analytic model (orange dashed line) for  $\tilde{\sigma}_d = 0.1$  and  $\alpha G = 1$ . A variation of  $\pm 0.2$  dex is shown around the analytic fit line (light grey strip).

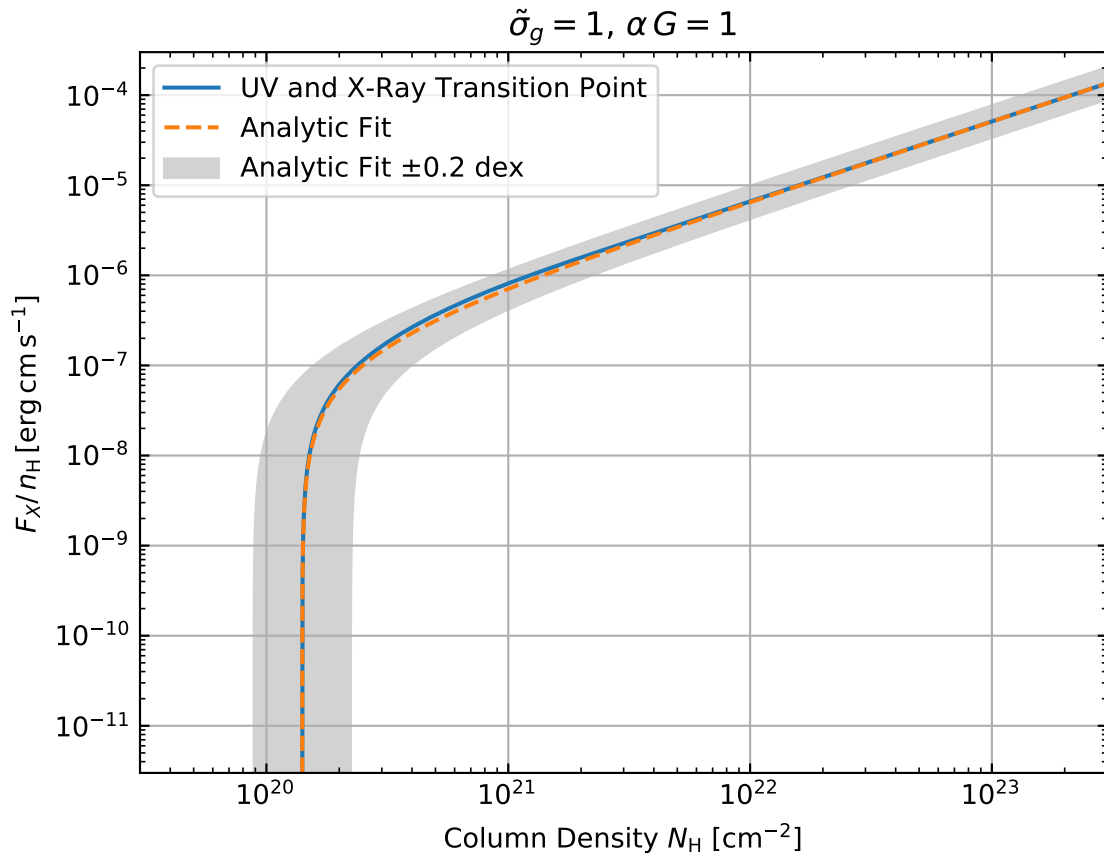


Figure C.11: The HXR perturbation transition point curve (solid blue line) superimposed with the analytic model (orange dashed line) for  $\tilde{\sigma}_d = 1$  and  $\alpha G = 1$ . A variation of  $\pm 0.2$  dex is shown around the analytic fit line (light grey strip).

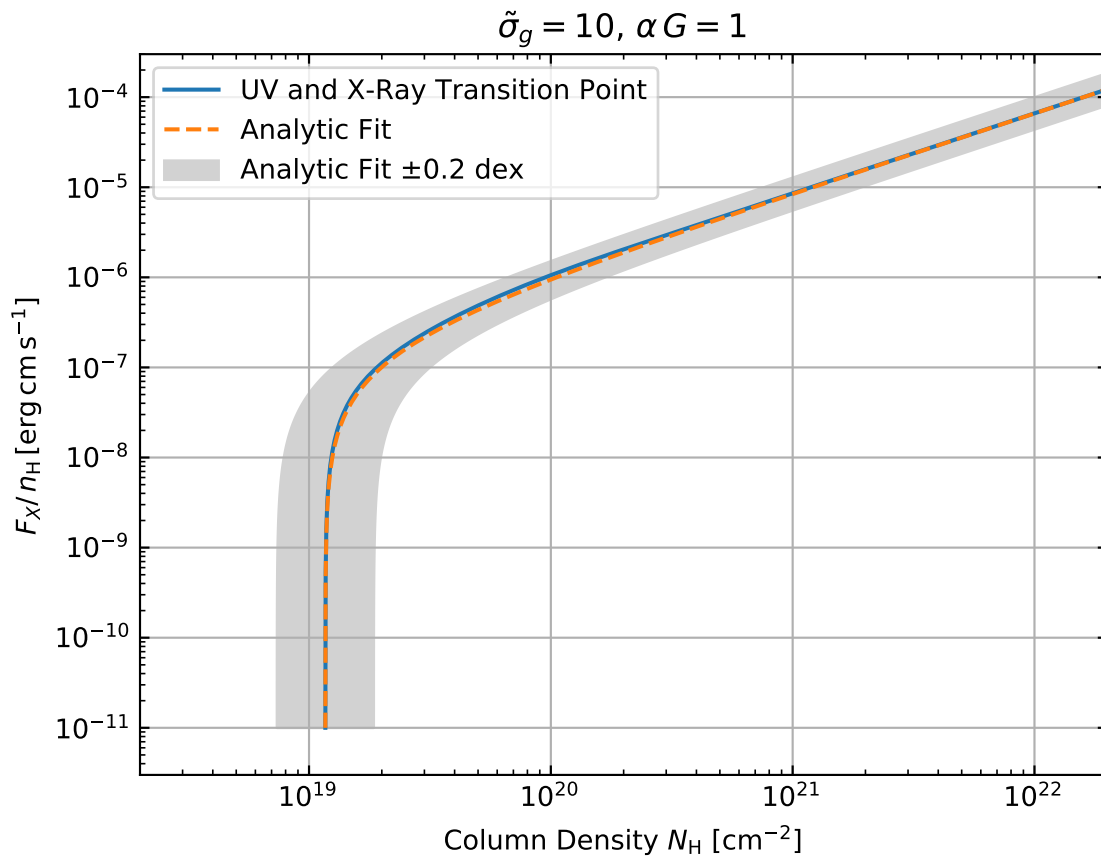


Figure C.12: The HXR perturbation transition point curve (solid blue line) superimposed with the analytic model (orange dashed line) for  $\tilde{\sigma}_d = 10$  and  $\alpha G = 1$ . A variation of  $\pm 0.2$  dex is shown around the analytic fit line (light grey strip).

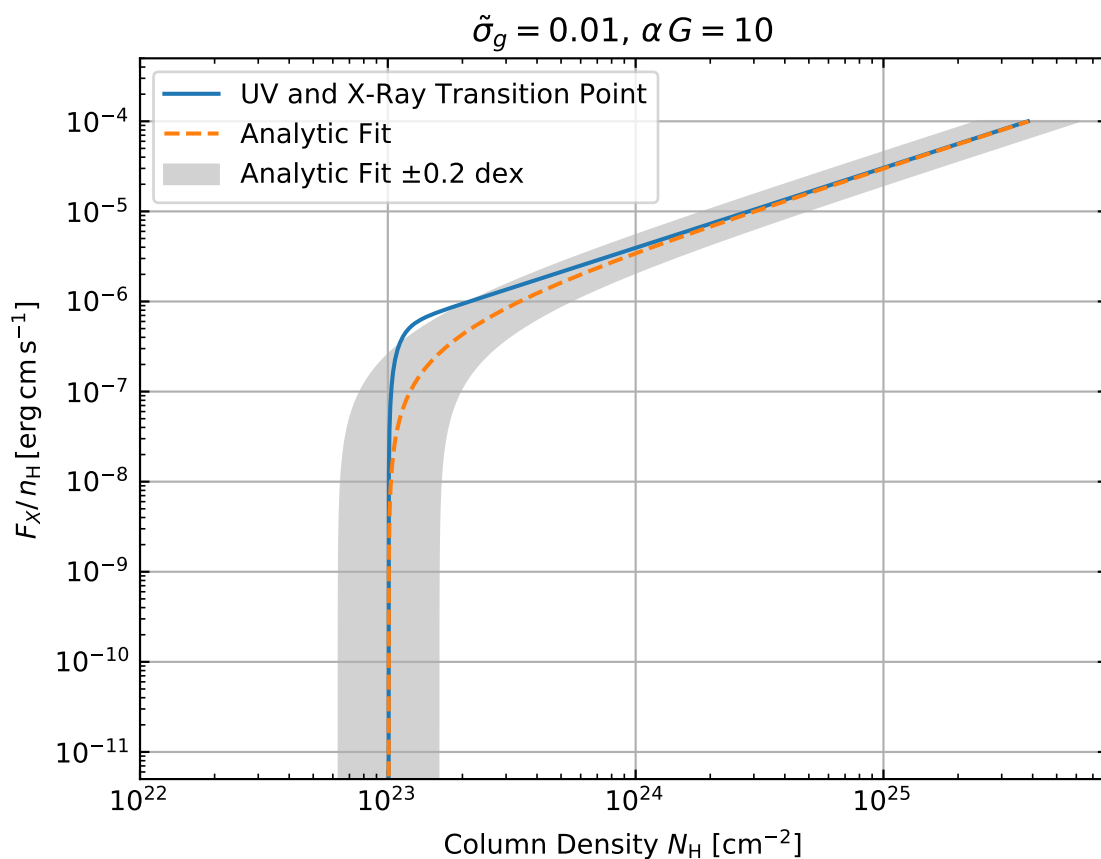


Figure C.13: The HXR perturbation transition point curve (solid blue line) superimposed with the analytic model (orange dashed line) for  $\tilde{\sigma}_d = 0.01$  and  $\alpha G = 10$ . A variation of  $\pm 0.2$  dex is shown around the analytic fit line (light grey strip).

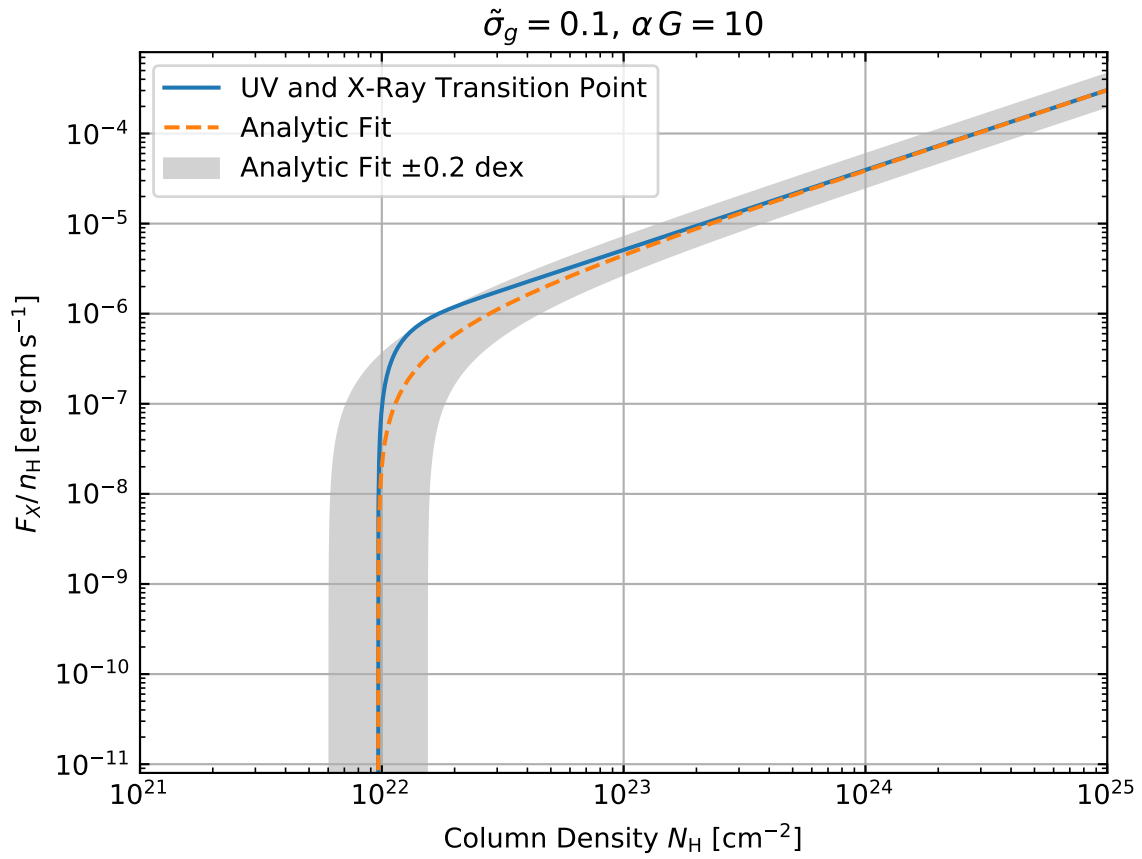


Figure C.14: The HXR perturbation transition point curve (solid blue line) superimposed with the analytic model (orange dashed line) for  $\tilde{\sigma}_d = 0.1$  and  $\alpha G = 10$ . A variation of  $\pm 0.2$  dex is shown around the analytic fit line (light grey strip).

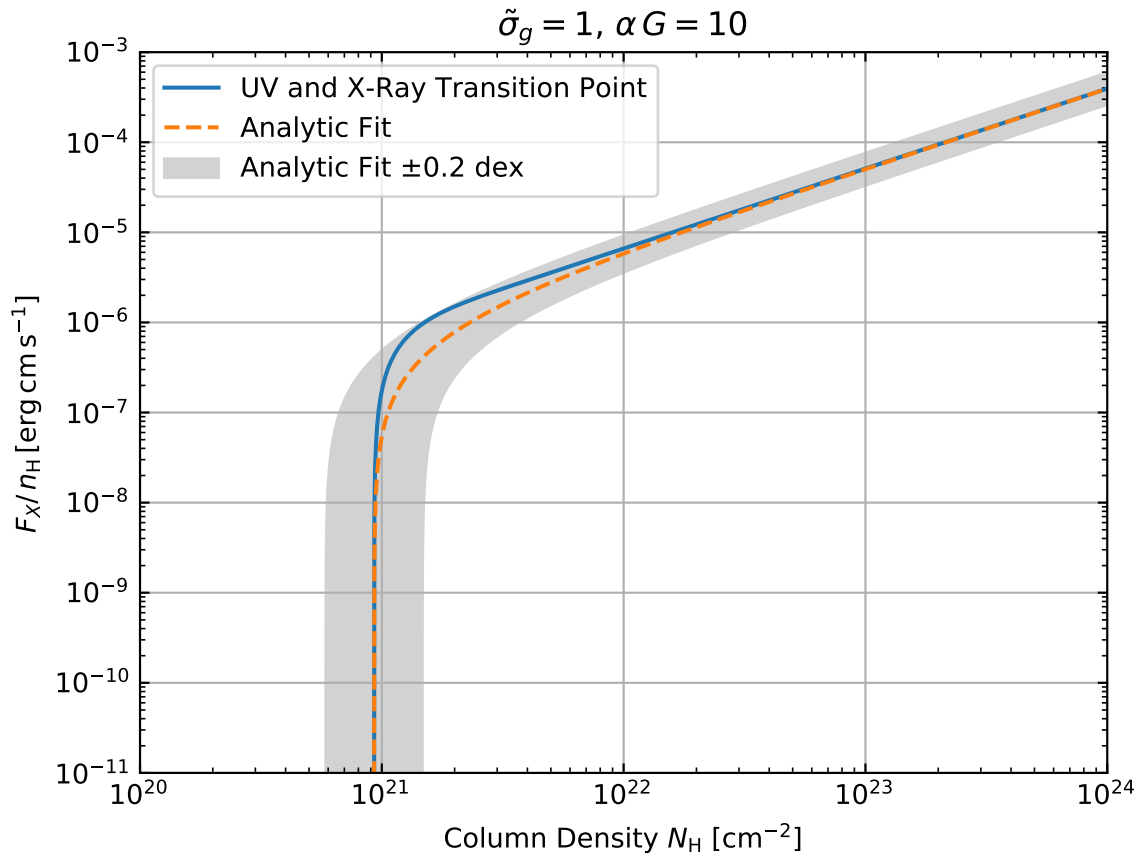


Figure C.15: The HXR perturbation transition point curve (solid blue line) superimposed with the analytic model (orange dashed line) for  $\tilde{\sigma}_d = 1$  and  $\alpha G = 10$ . A variation of  $\pm 0.2$  dex is shown around the analytic fit line (light grey strip).

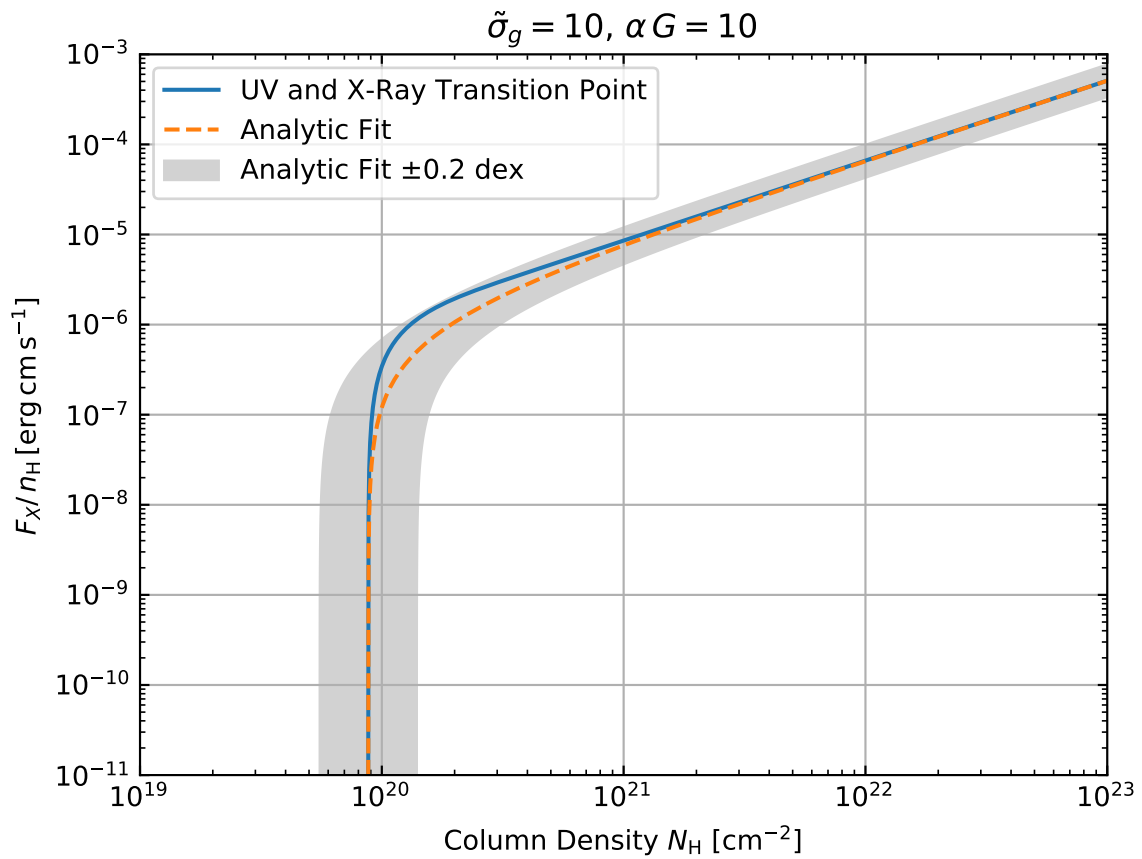


Figure C.16: The HXR perturbation transition point curve (solid blue line) superimposed with the analytic model (orange dashed line) for  $\tilde{\sigma}_d = 10$  and  $\alpha G = 10$ . A variation of  $\pm 0.2$  dex is shown around the analytic fit line (light grey strip).

# References

- [1] A. Sternberg, A. Dalgarno, The infrared response of molecular hydrogen gas to ultraviolet radiation - High-density regions, *ApJ*338 (1989) 197–233. doi:10.1086/167193.
- [2] A. Sternberg, F. Le Petit, E. Roueff, J. Le Bourlot, H I-to-H<sub>2</sub> Transitions and H I Column Densities in Galaxy Star-forming Regions, *ApJ*790 (2014) 10. arXiv:1404.5042, doi:10.1088/0004-637X/790/1/10.
- [3] P. R. Maloney, D. J. Hollenbach, A. G. G. M. Tielens, X-Ray-irradiated Molecular Gas. I. Physical Processes and General Results, *ApJ*466 (1996) 561. doi:10.1086/177532.
- [4] M. G. Wolfire, L. Vallini, M. Chevance, Photodissociation and X-Ray-Dominated Regions, *ARA&A*60 (2022) 247–318. arXiv:2202.05867, doi:10.1146/annurev-astro-052920-010254.
- [5] G. B. Field, W. B. Somerville, K. Dressler, Hydrogen Molecules in Astronomy, *ARA&A*4 (1966) 207. doi:10.1146/annurev.aa.04.090166.001231.
- [6] H. J. Habing, The interstellar radiation density between 912 Å and 2400 Å, *Bull. Astron. Inst. Netherlands*19 (1968) 421.
- [7] B. T. Draine, Photoelectric heating of interstellar gas, *ApJS*36 (1978) 595–619. doi:10.1086/190513.
- [8] A. G. G. M. Tielens, D. Hollenbach, Photodissociation regions. I. Basic model., *ApJ*291 (1985) 722–746. doi:10.1086/163111.
- [9] S. R. Federman, A. E. Glassgold, J. Kwan, Atomic to molecular hydrogen transition in interstellar clouds., *ApJ*227 (1979) 466–473. doi:10.1086/156753.
- [10] E. F. van Dishoeck, J. H. Black, Comprehensive Models of Diffuse Interstellar Clouds: Physical Conditions and Molecular Abundances, *ApJS*62 (1986) 109. doi:10.1086/191135.
- [11] A. Sternberg, The infrared response of molecular hydrogen gas to ultraviolet radiation - A scaling law, *ApJ*332 (1988) 400–409. doi:10.1086/166664.
- [12] B. T. Draine, F. Bertoldi, Structure of Stationary Photodissociation Fronts, *ApJ*468 (1996) 269. arXiv:astro-ph/9603032, doi:10.1086/177689.
- [13] B. T. Draine, Interstellar Dust Grains, *ARA&A*41 (2003) 241–289. arXiv:astro-ph/0304489, doi:10.1146/annurev.astro.41.011802.094840.
- [14] R. J. Gould, E. E. Salpeter, The Interstellar Abundance of the Hydrogen Molecule. I. Basic Processes., *ApJ*138 (1963) 393. doi:10.1086/147654.

- [15] M. Jura, Formation and destruction rates of interstellar  $H_2$ ., *ApJ*191 (1974) 375–379. doi:10.1086/152975.
- [16] S. Bialy, A. Sternberg, Analytic H I-to- $H_2$  Photodissociation Transition Profiles, *ApJ*822 (2016) 83. arXiv:1601.02608, doi:10.3847/0004-637X/822/2/83.
- [17] J. H. Krolik, T. R. Kallman, X-ray ionization and the Orion Molecular Cloud., *ApJ*267 (1983) 610–624. doi:10.1086/160897.
- [18] S. Lepp, R. McCray, X-ray sources in molecular clouds, *ApJ*269 (1983) 560–567. doi:10.1086/161062.
- [19] M. Spaans, R. Meijerink, F. P. Israel, A. F. Loenen, W. A. Baan, The irradiated ISM of ULIRGs, in: J. M. Chapman, W. A. Baan (Eds.), *Astrophysical Masers and their Environments*, Vol. 242, 2007, pp. 452–456. arXiv:0709.3430, doi:10.1017/S1743921307013580.
- [20] D. J. Hollenbach, A. G. G. M. Tielens, Dense Photodissociation Regions (PDRs), *ARA&A*35 (1997) 179–216. doi:10.1146/annurev.astro.35.1.179.
- [21] S. Lepp, S. Tiné, X-ray Dominated Regions, *The Molecular Astrophysics of Stars and Galaxies* 4 (1998) 489.
- [22] A. Sternberg, Photon-dominated Regions, *The Molecular Astrophysics of Stars and Galaxies* 4 (1998) 201.
- [23] D. J. Hollenbach, A. G. G. M. Tielens, Photodissociation regions in the interstellar medium of galaxies, *Reviews of Modern Physics* 71 (1) (1999) 173–230. doi:10.1103/RevModPhys.71.173.
- [24] M. Spaans, R. Meijerink, Dense Molecular Gas around Protostars and in Galactic Nuclei: PDRs and XDRs, *Ap&SS*295 (1-2) (2005) 239–248. doi:10.1007/s10509-005-3698-6.
- [25] R. Meijerink, PDRs and XDRs, in: J. Cernicharo, R. Bachiller (Eds.), *The Molecular Universe*, Vol. 280, 2011, pp. 177–186. doi:10.1017/S1743921311024963.
- [26] Röllig, M., Abel, N. P., Bell, T., Bensch, F., Black, J., Ferland, G. J., Jonkheid, B., Kamp, I., Kaufman, M. J., Le Bourlot, J., Le Petit, F., Meijerink, R., Morata, O., Ossenkopf, V., Roueff, E., Shaw, G., Spaans, M., Sternberg, A., Stutzki, J., Thi, W.-F., van Dishoeck, E. F., van Hoof, P. A. M., Viti, S., Wolfire, M. G., A photon dominated region code comparison study\*, *A&A* 467 (1) (2007) 187–206. doi:10.1051/0004-6361:20065918.  
URL <https://doi.org/10.1051/0004-6361:20065918>
- [27] S. S. Prasad, S. P. Tarafdar, UV radiation field inside dense clouds - Its possible existence and chemical implications, *ApJ*267 (1983) 603–609. doi:10.1086/160896.
- [28] R. Gredel, S. Lepp, A. Dalgarno, The C/CO Ratio in Dense Interstellar Clouds, *ApJ*323 (1987) L137. doi:10.1086/185073.
- [29] R. Gredel, S. Lepp, A. Dalgarno, E. Herbst, Cosmic-Ray-induced Photodissociation and Photoionization Rates of Interstellar Molecules, *ApJ*347 (1989) 289. doi:10.1086/168117.
- [30] D. Hollenbach, C. F. McKee, Molecule formation and infrared emission in fast interstellar shocks. I. Physical processes., *ApJS*41 (1979) 555–592. doi:10.1086/190631.

- [31] P. M. Gondhalekar, R. Wilson, The interstellar radiation field between 912 Å and 2740 Å, *A&A*38 (1975) 329–333.
- [32] S. Hayakawa, K. Yamashita, S. Yoshioka, Diffuse Component of the Cosmic Far UV Radiation and Interstellar Dust Grains, *Ap&SS*5 (1969) 493–502. doi:10.1007/BF00652397.
- [33] R. C. Henry, J. R. Swandic, S. D. Shulman, G. Fritz, Far-ultraviolet studies. II - Galactic-latitude dependence of the 1530 Å interstellar radiation field, *ApJ*212 (1977) 707–713. doi:10.1086/155095.
- [34] D. J. Hollenbach, M. W. Werner, E. E. Salpeter, Molecular Hydrogen in H I Regions, *ApJ*163 (1971) 165. doi:10.1086/150755.
- [35] A. N. Witt, M. W. Johnson, The Interstellar Radiation Density Between 1250 and 4250 Å, *ApJ*181 (1973) 363–368. doi:10.1086/152054.
- [36] L. C. Lee, Photodissociation rates of molecules by the interstellar radiation field, *ApJ*282 (1984) 172–177. doi:10.1086/162188.
- [37] W. G. Roberge, A. Dalgarno, B. P. Flannery, Photoionization and photodissociation in diffuse interstellar clouds, *ApJ*243 (1981) 817–826. doi:10.1086/158648.
- [38] S. Hocuk, L. Szűcs, P. Caselli, S. Cazaux, M. Spaans, G. B. Esplugues, Parameterizing the interstellar dust temperature, *A&A*604 (2017) A58. arXiv:1704.02763, doi:10.1051/0004-6361/201629944.
- [39] A. G. G. M. Tielens, *The Physics and Chemistry of the Interstellar Medium*, Cambridge University Press, 2005.
- [40] E. Teller, über das Wasserstoffmolekülion, *Zeitschrift für Physik* 61 (1930) 458–480. doi:10.1007/BF01330302.
- [41] E. E. Salpeter, LETTERS TO THE EDITOR: Dissociation Cross Sections for Fast Hydrogen Molecule Ions, *Proceedings of the Physical Society A* 63 (1950) 1295–1297. doi:10.1088/0370-1298/63/11/116.
- [42] L. Spitzer, Jr., The Temperature of Interstellar Matter. I., *ApJ*107 (1948) 6. doi:10.1086/144984.
- [43] T. P. Stecher, D. A. Williams, Photodestruction of Hydrogen Molecules in H I Regions, *ApJ*149 (1967) L29. doi:10.1086/180047.
- [44] W. Lichten, Metastable Hydrogen Molecules, *Physical Review* 120 (1960) 848–853. doi:10.1103/PhysRev.120.848.
- [45] H. Abgrall, E. Roueff, F. Launay, J. Y. Roncin, J. L. Subtil, The Lyman and Werner Band Systems of Molecular Hydrogen, *Journal of Molecular Spectroscopy* 157 (1993) 512–523. doi:10.1006/jmsp.1993.1040.
- [46] T. Lyman, The Spectrum of Hydrogen in the Region of Extremely Short Wave-Lengths, *ApJ*23 (1906) 181. doi:10.1086/141330.
- [47] S. Werner, Hydrogen Bands in the Ultra-Violet Lyman Region, *Proceedings of the Royal Society of London Series A* 113 (1926) 107–117. doi:10.1098/rspa.1926.0142.

- [48] S. Nishimura, K. Takayanagi, On the Photodestruction Rate of Hydrogen Molecules in HI Regions, PASJ21 (1969) 111.
- [49] P. F. Bernath, Spectra of atoms and molecules, 2nd Ed., Oxford University Press, Oxford, UK, 2005.
- [50] G. Herzberg, Molecular spectra and molecular structure. Vol I. Spectra of diatomic molecules, D. Van Nostrand, Princeton, NJ, 1950.
- [51] R. N. Zare, Angular momentum: Understanding spatial aspects in chemistry and physics, Wiley-Interscience, New York, NY, 1988. doi:10.1002/bbpc.19890930427.
- [52] G. R. Cook, P. H. Metzger, Photoionization and Absorption Cross Sections of H<sub>2</sub> and D<sub>2</sub> in the Vacuum Ultraviolet Region, Journal of the Optical Society of America (1917-1983) 54 (1964) 968.
- [53] R. W. Nicholls, Franck-Condon Factors for the H<sub>2</sub> Lyman-Band System., ApJ141 (1965) 819. doi:10.1086/148169.
- [54] M. Halmann, I. Laulicht, Isotope Effects on Franck—Condon Factors. V. Electronic Transitions of Isotopic O<sub>2</sub>, N<sub>2</sub>, C<sub>2</sub>, and H<sub>2</sub> Molecules, J. Chem. Phys..
- [55] S. Rothenberg, E. R. Davidson, Theoretical intensities for the X <sup>1</sup>Σ<sub>g</sub><sup>+</sup>-np <sup>1</sup>Π<sub>u</sub> transitions of H<sub>2</sub>. A study of the Franck-Condon principle, Journal of Molecular Spectroscopy 22 (1967) 1–17. doi:10.1016/0022-2852(67)90143-9.
- [56] A. Dalgarno, T. L. Stephens, Discrete Absorption and Photodissociation of Molecular Hydrogen, ApJ160 (1970) L107. doi:10.1086/180539.
- [57] T. L. Stephens, A. Dalgarno, Spontaneous radiative dissociation in molecular hydrogen., J. Quant. Spec. Radiat. Transf.12 (1972) 569–586. doi:10.1016/0022-4073(72)90168-9.
- [58] H. Abgrall, E. Roueff, I. Drira, Total transition probability and spontaneous radiative dissociation of B, C, B' and D states of molecular hydrogen, A&AS141 (2000) 297–300. doi:10.1051/aas:2000121.
- [59] R. J. Gould, M. Harwit, Expected Near Infrared Radiation from Interstellar Molecular Hydrogen., ApJ137 (1963) 694. doi:10.1086/147544.
- [60] J. H. Black, A. Dalgarno, Interstellar H<sub>2</sub> - The population of excited rotational states and the infrared response to ultraviolet radiation, ApJ203 (1976) 132–142. doi:10.1086/154055.
- [61] J. M. Shull, Vibrational excitation of H<sub>2</sub> in intense ultraviolet fluxes, ApJ219 (1978) 877–885. doi:10.1086/155850.
- [62] J. H. Black, E. F. van Dishoeck, Fluorescent excitation of interstellar H<sub>2</sub>, ApJ322 (1987) 412–449. doi:10.1086/165740.
- [63] D. A. Neufeld, M. Spaans, Red Fluorescent Line Emission from Hydrogen Molecules in Diffuse Molecular Clouds, ApJ473 (1996) 894. doi:10.1086/178201.
- [64] A. C. Allison, A. Dalgarno, Band Oscillator Strengths and Transitions Probabilities for the Lyman and Werner Systems of H<sub>2</sub>, HD, and D<sub>2</sub>, Atomic Data 1 (1969) 289. doi:10.1016/S0092-640X(69)80024-0.

- [65] B. T. Draine, *Physics of the Interstellar and Intergalactic Medium*, Princeton University Press, Princeton, NJ, 2011.
- [66] A. K. Pradhan, S. N. Nahar, *Atomic Astrophysics and Spectroscopy*, 2011.
- [67] S. Kwok, *Physics and chemistry of the interstellar medium*, University Science Books, Sausalito, CA, 2007.
- [68] H. L. Johnson, W. W. Morgan, Fundamental stellar photometry for standards of spectral type on the Revised System of the Yerkes Spectral Atlas., *ApJ*117 (1953) 313. doi:10.1086/145697.
- [69] R. C. Bohlin, B. D. Savage, J. F. Drake, A survey of interstellar H I from L $\alpha$  absorption measurements. II., *ApJ*224 (1978) 132–142. doi:10.1086/156357.
- [70] G. J. Ferland, M. Chatzikos, F. Guzmán, M. L. Lykins, P. A. M. van Hoof, R. J. R. Williams, N. P. Abel, N. R. Badnell, F. P. Keenan, R. L. Porter, P. C. Stancil, The 2017 Release Cloudy, *Rev. Mexicana Astron. Astrofis.*53 (2017) 385–438. arXiv:1705.10877.
- [71] S. Datz, G. Sundström, C. Biedermann, L. Broström, H. Danared, S. Mannervik, J. R. Mowat, M. Larsson, Branching processes in the dissociative recombination of H<sub>3</sub><sup>+</sup>, *Phys. Rev. Lett.*74 (6) (1995) 896–899. doi:10.1103/PhysRevLett.74.896.
- [72] P. C. Stancil, S. Lepp, A. Dalgarno, The Deuterium Chemistry of the Early Universe, *ApJ*509 (1) (1998) 1–10. doi:10.1086/306473.
- [73] C. F. McKee, M. R. Krumholz, The Atomic-to-Molecular Transition in Galaxies. III. A New Method for Determining the Molecular Content of Primordial and Dusty Clouds, *ApJ*709 (1) (2010) 308–320. arXiv:0908.0330, doi:10.1088/0004-637X/709/1/308.
- [74] H. C. van de Hulst, *Evolution and Physics of Solid Particles*, Vol. 7, 1948, p. 73.
- [75] M. J. Barlow, J. Silk, H<sub>2</sub> recombination on interstellar grains., *ApJ*207 (1976) 131–140. doi:10.1086/154477.
- [76] S. Cazaux, A. G. G. M. Tielens, Molecular Hydrogen Formation in the Interstellar Medium, *ApJ*575 (1) (2002) L29–L32. arXiv:astro-ph/0207035, doi:10.1086/342607.
- [77] W. W. Duley, D. A. Williams, The formation of interstellar H<sub>2</sub> on amorphous silicate grains, *MNRAS*223 (1986) 177–182. doi:10.1093/mnras/223.1.177.
- [78] E. Habart, F. Boulanger, L. Verstraete, C. M. Walmsley, G. Pineau des Forêts, Some empirical estimates of the H<sub>2</sub> formation rate in photon-dominated regions, *A&A*414 (2004) 531–544. arXiv:astro-ph/0311040, doi:10.1051/0004-6361:20031659.
- [79] D. Hollenbach, E. E. Salpeter, Surface Recombination of Hydrogen Molecules, *ApJ*163 (1971) 155. doi:10.1086/150754.
- [80] J. Le Bourlot, F. Le Petit, C. Pinto, E. Roueff, F. Roy, Surface chemistry in the interstellar medium. I. H<sub>2</sub> formation by Langmuir-Hinshelwood and Eley-Rideal mechanisms, *A&A*541 (2012) A76. arXiv:1202.0374, doi:10.1051/0004-6361/201118126.
- [81] M. A. Leitch-Devlin, D. A. Williams, Sticking coefficients for atoms and molecules at the surfaces of interstellar dust grains, *MNRAS*213 (1985) 295–306. doi:10.1093/mnras/213.2.295.

- [82] V. Pirronello, C. Liu, L. Shen, G. Vidali, Laboratory Synthesis of Molecular Hydrogen on Surfaces of Astrophysical Interest, *ApJ*475 (1) (1997) L69–L72. [arXiv:astro-ph/9611022](#), [doi:10.1086/310464](#).
- [83] J. Takahashi, K. Masuda, M. Nagaoka, The formation mechanism of molecular hydrogen on icy mantles of interstellar dust, *MNRAS*306 (1) (1999) 22–30. [doi:10.1046/j.1365-8711.1999.02480.x](#).
- [84] V. Wakelam, E. Bron, S. Cazaux, F. Dulieu, C. Gry, P. Guillard, E. Habart, L. Hornekær, S. Morisset, G. Nyman, V. Pirronello, S. D. Price, V. Valdivia, G. Vidali, N. Watanabe, H<sub>2</sub> formation on interstellar dust grains: The viewpoints of theory, experiments, models and observations, *Molecular Astrophysics* 9 (2017) 1–36. [arXiv:1711.10568](#), [doi:10.1016/j.molap.2017.11.001](#).
- [85] M. Jura, Interstellar clouds containing optically thin H<sub>2</sub>., *ApJ*197 (1975) 575–580. [doi:10.1086/153545](#).
- [86] R. Morrison, D. McCammon, Interstellar photoelectric absorption cross sections, 0.03-10 keV., *ApJ*270 (1983) 119–122. [doi:10.1086/161102](#).
- [87] R. F. Mushotzky, The X-ray spectrum and time variability of narrow emission line galaxies., *ApJ*256 (1982) 92–102. [doi:10.1086/159886](#).
- [88] G. M. Voit, Energy Deposition by X-Ray Photoelectrons into Interstellar Molecular Clouds, *ApJ*377 (1991) 158. [doi:10.1086/170344](#).
- [89] C. B. Tarter, W. H. Tucker, E. E. Salpeter, The Interaction of X-Ray Sources with Optically Thin Environments, *ApJ*156 (1969) 943. [doi:10.1086/150026](#).
- [90] J. M. Shull, M. E. van Steenberg, X-ray secondary heating and ionization in quasar emission-line clouds, *ApJ*298 (1985) 268–274. [doi:10.1086/163605](#).
- [91] A. Sternberg, A. Dalgarno, S. Lepp, Cosmic-Ray-induced Photodestruction of Interstellar Molecules in Dense Clouds, *ApJ*320 (1987) 676. [doi:10.1086/165585](#).
- [92] A. E. Glassgold, D. Galli, M. Padovani, Cosmic-Ray and X-Ray Heating of Interstellar Clouds and Protoplanetary Disks, *ApJ*756 (2) (2012) 157. [arXiv:1208.0523](#), [doi:10.1088/0004-637X/756/2/157](#).
- [93] A. Sternberg, A. Dalgarno, Chemistry in Dense Photon-dominated Regions, *ApJS*99 (1995) 565. [doi:10.1086/192198](#).

# Curriculum Vitae

Graduate College  
University of Nevada, Las Vegas

Gregory Colarch

email:

qftgauge@gmail.com

Degrees:

Bachelor of Science, Astrophysics, 2009  
University of Calgary, Canada

Master of Science, Physics, 2012  
University of Nevada, Las Vegas, USA

Master of Science, Health Physics, 2015  
University of Nevada, Las Vegas, USA

Doctor of Philosophy, Physics, 2019  
University of Nevada, Las Vegas, USA

Dissertation Title:  $H^0$  -  $H_2$  transition profiles  
in PDRs and XDRs

Dissertation Examination Committee:

Chairperson, Stephen Lepp, Ph.D.  
Committee Member, Tao Pang, Ph.D.  
Committee Member, Bernard Zygelman, Ph.D.  
Graduate Faculty Representative, Steen Madsen, Ph.D.